ADVERTIMENT. La consulta d'aquesta tesi queda condicionada a l'acceptació de les següents condicions d'ús: La difusió d'aquesta tesi per mitjà del servei TDX (www.tesisenxarxa.net) ha estat autoritzada pels titulars dels drets de propietat intel·lectual únicament per a usos privats emmarcats en activitats d'investigació i docència. No s'autoritza la seva reproducció amb finalitats de lucre ni la seva difusió i posada a disposició des d'un lloc aliè al servei TDX. No s'autoritza la presentació del seu contingut en una finestra o marc aliè a TDX (framing). Aquesta reserva de drets afecta tant al resum de presentació de la tesi com als seus continguts. En la utilització o cita de parts de la tesi és obligat indicar el nom de la persona autora.

ADVERTENCIA. La consulta de esta tesis queda condicionada a la aceptación de las siguientes condiciones de uso: La difusión de esta tesis por medio del servicio TDR (www.tesisenred.net) ha sido autorizada por los titulares de los derechos de propiedad intelectual únicamente para usos privados enmarcados en actividades de investigación y docencia. No se autoriza su reproducción con finalidades de lucro ni su difusión y puesta a disposición desde un sitio ajeno al servicio TDR. No se autoriza la presentación de su contenido en una ventana o marco ajeno a TDR (framing). Esta reserva de derechos afecta tanto al resumen de presentación de la tesis como a sus contenidos. En la utilización o cita de partes de la tesis es obligado indicar el nombre de la persona autora.

WARNING. On having consulted this thesis you're accepting the following use conditions: Spreading this thesis by the TDX (www.tesisenxarxa.net) service has been authorized by the titular of the intellectual property rights only for private uses placed in investigation and teaching activities. Reproduction with lucrative aims is not authorized neither its spreading and availability from a site foreign to the TDX service. Introducing its content in a window or frame foreign to the TDX service is not authorized (framing). This rights affect to the presentation summary of the thesis as well as to its contents. In the using or citation of parts of the thesis it's obliged to indicate the name of the author

Structural and electrical characterization of doped graphene and carbon nanotube networks

Muhammad Zahir Iqbal

Doctoral Dissertation

Universitat Politècnica de Catalunya (UPC) Barcelona Tech.

Sejong University

May 2014

Structural and electrical characterization of doped graphene and carbon nanotube networks

Muhammad Zahir Iqbal

Submitted in partial fulfillment of the requirements for the degree of doctor of philosophy in the "Doctorate of Computational and Applied Physics" from Department of Applied Physics and Physics & Nuclear Engineering Dept., Universitat Politècnica de Catalunya, Barcelona Tech. and Department of Physics, Sejong University.

Thesis Advisers:

Professor Dr. Núria Ferrer-Anglada   **Professor Dr. Jonghwa Eom**

Universitat Politècnica de Catalunya (UPC) Barcelona Tech.   **Sejong University**

May 2014

© 2014

Muhammad Zahir Iqbal

All Rights Reserved

ABSTRACT

Graphene, a two-dimensional sp^2-hybridized network of carbon atoms has received a remarkable cornucopia of new physics and served as a unique model system, due particularly to its electronic properties, which could have interesting applications in electronic, spintronic or quantum devices. The first part of the thesis describes the modulation of graphene's structural and electrical properties with various kinds of doping; such as deep ultraviolet irradiation in ambient atmosphere, deep ultraviolet light irradiation in different gaseous environments, and electron beam irradiation. We have fabricated graphene (exfoliated and chemical vapor deposition grown graphene) field effect transistors using photolithography and electron beam lithography and characterized with AFM, Raman spectroscopy and transport measurement using low noise standard lock-in amplifier technique. We have explored how the ultraviolet light exposure tunes the electrical properties of graphene in an ambient atmosphere, confirmed by the shift of Dirac point position towards positive gate voltage, revealing p-type doping for graphene without degradation of mobility. We found that the doping is stable for a time scale of months. This method became more useful when half the graphene device was exposed by ultraviolet light, while the other half part was covered by a mask to make a sharp p-n junction. The doping effect became more prominent and controllable when it was made in an oxygen environment. The most interesting phenomena were observed when doped graphene was restored to a pristine state using ultraviolet light irradiation in a nitrogen environment. Furthermore, we have investigated the doping tunability with ultraviolet light irradiation on mechanically exfoliated single-, bi-, and trilayer graphenes without significantly degrading its charge carrier mobility. In a further study, the structural deformation of graphene was investigated by irradiation of an electron beam. The graphene structure changes its phase in various stages, where graphene transforms gradually from a crystalline to a nanocrystalline form and after a certain irradiation time into an amorphous form. This irradiation effect acts as an n-type dopant for graphene. In this case, mobility decreases with the gradual increase of irradiation dose, which implies the formation of localized states. The second part of the thesis describes carbon nanotube networks as flexible and transparent electrodes for electronic devices, particularly for high frequency applications. The observed results show that at low frequencies, the impedance increases as the density of nanotube networks decreases, as expected. Both the real and imaginary parts of impedance (measured up to 20 GHz) abruptly decrease as the frequency increases over the cut-off frequency. The cut-off frequency not only depends on the carbon nanotube density of the network, but also on the sample geometry. The Nyquist diagram suggests a simple equivalent circuit composed of a parallel combination of a resistor and a capacitor. The experimental results are in line with calculations made by electrochemical spectroscopy simulations. The results show that the electrical behavior is mostly determined by the contact resistance between the nanotubes, which are in a completely disordered distribution in the network. We show that carbon nanotube flexible conducting films, which may be transparent, could be competitive for some applications, such as displays, photovoltaic solar cells or selective sensors.

RESUM

El grafè, considerat com una xarxa bidimensional d'àtoms de carboni units per enllaços híbrids sp^2, és un tema de recerca molt prolífer en els últims anys, com a model de sòlid bidimensional, i molt particularment degut a les seves propietats electròniques, que poden tenir aplicacions interessants en dispositius electrònics, spintrònics o quàntics. La primera part de la Tesi descriu la modificació de les propietats estructurals i elèctriques del grafè utilitzant diferents mètodes per a dopar-lo: radiació ultraviolada d'alta energia (DUV) en atmosfera ambient, DUV en diferents gasos tals com oxigen o nitrogen, o irradiant amb un feix d'electrons (e-beam). Hem fabricat transistors d'efecte de camp (FET) amb grafè (exfoliat a partir del grafit, o bé obtingut per deposició química en fase vapor, CVD) utilitzant fotolitografia i e-beam litografia, i els hem caracteritzat mitjançant AFM, espectroscòpia Raman i mesures de transport elèctric, per a les que hem utilitzat la tècnica d'amplificació de baix soroll, el lock-in. Hem investigat com l'exposició a la llum ultraviolada en atmosfera ambient, modula les propietats elèctriques del grafè, de manera que la posició del punt de Dirac es desplaça cap a tensions de porta positives, cosa que implica dopatge de tipus-p, sense que hi hagi degradació de la mobilitat. El dopatge és estable al menys durant mesos. Amb el mateix mètode, quan només la meitat del dispositiu és exposat a la radiació ultraviolada mentre l'altre meitat és recobert per una màscara metàl·lica, hem obtingut una unió p-n. L'efecte de dopatge és més important i controlable, quan és fet en atmosfera d'oxigen. L'efecte més interessant que hem observat és la reversibilitat, quan el grafè dopat retorna al seu estat primitiu, en ser irradiat amb llum ultraviolada en atmosfera de nitrogen. També hem investigat el dopatge amb llum ultraviolada del grafè exfoliat mecànicament, de una, dues o tres capes, observant que es produeix sense una degradació significativa de la mobilitat dels portadors de càrrega. Posteriorment hem estudiat la deformació estructural del grafè quan és irradiat amb un feix d'electrons. Hem observat canvis estructurals en diferents etapes: el grafè evoluciona gradualment, a partir de la forma cristal·lina, cap a una fase d'estructura nanocristal·lina i finalment, després d'una certa dosi de irradiació, presenta una estructura amorfa. L'efecte d' irradiar el grafè amb electrons actua com a dopant tipus-n, però en aquest cas la mobilitat decreix en incrementar la dosi, això implica que hi ha formació d'estats localitzats. La segona part de la Tesi tracta de capes primes de nanotubs de carboni, com a elèctrodes flexibles i transparents per a dispositius electrònics, en particular per aplicacions d'alta freqüència. Els resultats obtinguts mostren que, a baixes freqüències, la impedància augmenta en disminuir la densitat de nanotubs, tal com cal esperar. Tan la part real com la part imaginària de la impedància (mesurada fins a 20 GHz) decreixen abruptament en augmentar la freqüència més enllà de la freqüència de tall. La freqüència de tall no depèn únicament de la densitat de nanotubs en la capa, sinó també de la geometria de la mostra. El diagrama de Nyquist es pot interpretar amb un circuit equivalent consistent simplement en una resistència i un condensador en paral·lel. Els resultats experimentals s'ajusten bé a les simulacions fetes per espectroscòpia d'impedàncies (EIS). Els resultats posen en evidència que el comportament elèctric queda majoritàriament determinat per la resistència de contacte entre els nanotubs,

que formen la xarxa amb una distribució totalment desordenada. Hem vist que capes primes de nanotubs de carboni conductores i flexibles, que poden ser també transparents, poden ser competitives en diferents aplicacions, com ara pantalles, cel·les solars fotovoltaiques o sensors selectius.

To,

those who live in my mind,
in my heart,
throughout of the whole span of my life
and or
the Nearest, dearest, and deepest to me.

To,
my beloved
Mother
and affectionate
Father,
Who taught me?
the first words to speak,
the alphabet to write
and
the first steps to take.

ACKNOWLEDGMENTS

I have the only pearls of my eyes to admire the blessings of the compassionate and omnipotent one, because words are bound, knowledge is limited, and time is short is for expressing His dignity. It is one of the infinite of Allah that bestowed on me with the potential and ability to complete the present research program on time and make a material contribution towards the deep oceans of Hazrat Muhammad (Sallallaho Allaihe Waalahe Wassalam), the city of knowledge, who has guided his "Umma" to seek knowledge from the cradle to the grave, and who is forever the torch of guidance and knowledge for humanity as a whole.

My cordial gratitude goes to my supervisor at Sejong. I have no words to thank to Prof. Dr. Jonghwa Eom. Although the word thanks is too little to explain my feelings and emotions. I can never forget his outstanding manners, genius way of thinking and benevolence towards me. Because of his fruitful and everlasting efforts I feel very confident in myself in the field of science, research and skills. I often drew the inspiration from his incessant novel ideas. I consider myself fortunate to have the honor of being the first PhD student under his supervision.

I feel great pleasure in expressing my deep sense of devotion and sincerest feelings to my advisor at the UPC, Prof. Dr. Nuria Ferrer-Anglada for her extraordinary guidance. She showed me the right direction of research and helped me to get started on the journey for my PhD degree. She was always available for my questions and gave generously of her time and knowledge. I always enjoyed her company because of her glorious and friendly attitude.

I shall forever feel proud to have had such nice, dedicated, cooperative and sincere lab mates: Waqas, Farooq, Jordi, Aida and friends Ozgur, Sajjad, Waseem, who provided me excellent support; a pleasant company who never let me feel alone or gloomy even in the most difficult times of research.

I cannot close without giving my fervent and heartiest compliments to my son (Muhammad Ali Rayan), my Wife (Salma Zahir), my sisters and my uncle Mr. Sadiq Asif, for helping me to come this far. No acknowledgement could ever adequately express my obligations to my affectionate and adoring parents and my guardian Mr. Mughal Hussain Shah (Late), whose hands are always raised in prayers for me and without whose moral support, the present distinction would have merely been a dream.

Muhammad Zahir Iqbal

TABLE OF CONTENTS

1 INTRODUCTION 1

1.1 Overview and history of graphene 1

1.2 Basic electronic properties of carbon based structures 2

1.3 The structural and transport properties of graphene 3
1.3.1 Structural characterization using Raman spectroscopy 3
1.3.2 Transport properties of graphene 5

1.4 Motivation of work 7

1.5 Organization of the thesis 7

2 EXPERIMENTAL METHODS 10

2.1 Fabrication of graphene flakes by mechanical exfoliation of graphite using the scotch tape technique 10

2.2 Graphene towards large scale production 10

2.3 Graphene transfer method 11

2.4 Fabrication recipe of a graphene device on silicon dioxide substrate 12

2.5 Photolithography patterning on graphene 12

2.6 Electron beam lithography patterning on graphene 14

2.7 Patterning using metal masks 16

2.8 Setup of the lock-in based electrical transport measurements 17

2.9 Doping with DUV irradiation 18

2.10 Structural disorder with E-beam irradiation 19

2.11 Impedance analysis 19

3 TUNING THE ELECTRICAL PROPERTIES OF EXFOLIATED GRAPHENE LAYERS BY DEEP ULTRAVIOLET IRRADIATION 20

3.1 Introduction 20

3.2 Device fabrication and characterization 21
3.2.1 Preparation of graphenes 21
3.2.2 DUV doping and characterization 22

3.3 Results and discussion 22

3.4 Conclusion 28

CHAPTER 4 29

4 FORMATION OF P-N JUNCTION WITH STABLE P-DOPING IN GRAPHENE FIELD EFFECT TRANSISTORS USING DEEP UV IRRADIATION 29

4.1 Introduction 29

4.2 Experimental 30

4.3 Results and discussion 31

4.4 Conclusion 36

5 ULTRAVIOLET LIGHT INDUCED REVERSIBLE MODULATION OF DOPING IN GRAPHENE TRANSISTORS WITH EFFICIENT PHOTOCURRENT GENERATION 37

5.1 Introduction 37

5.2 Experimental 38
5.2.1 Graphene growth and device fabrication 38

5.3 Results and discussion 39
5.3.1 Evaluation of Raman spectra of DUV irradiated graphene 39
5.3.2 Transport measurements of DUV irradiated graphene 40
5.3.3 X-ray photoelectron spectroscopy of pristine and DUV irradiated graphene 42
5.3.4 Photo-conductance measurement of the graphene transistor in DUV, DUV/O_2 and DUV/N_2 environments 45

5.4 Conclusion 45

6 THE STRUCTURAL AND ELECTRICAL EVOLUTION OF CHEMICAL VAPOR DEPOSITION GROWN GRAPHENE BY ELECTRON BEAM IRRADIATION INDUCED DISORDER 46

6.1 Introduction 46

6.2 Experimental 47

6.3 Results and discussion 48
6.3.1 Evaluation of Raman spectra of e-beam irradiated graphene 48
6.3.2 Transport measurements of E-beam irradiated graphene devices 51

6.4 Conclusion 53

7 HIGH FREQUENCY IMPEDANCE OF SINGLE-WALLED CARBON NANOTUBE NETWORKS ON FLEXIBLE SUBSTRATE 54

7.1 Introduction 54

7.2 Experimental 56

7.3 Results and discussion 57
7.3.1 Raman spectroscopy, surface morphology and optical absorption analysis 57
7.3.2 Impedance analysis with two-probe setup up to 100 MHz 58
7.3.3 Impedance analysis up to 20 GHz 60

7.4 Conclusions 62

8 SUMMARY AND OUTLOOK 64

9 BIBLIOGRAPHY 68

LIST OF FIGURES

Figure 1.1. (a) The ground-state electronic shell configuration of s and p hybridized orbitals generated by the superposition of 2s with $2p_x$ and $2p_y$ orbitals. (b) Graphene is a honeycomb lattice of carbon atoms. Graphite can be viewed as a stack of graphene layers. Carbon nanotubes are rolled-up cylinders of graphene and fullerenes (C_{60}) are molecules consisting of wrapped graphene by the introduction of pentagons on the hexagonal lattice. (Adapted from A Catro Neto 2009 & A. Giem 2010) 2
Figure 1.2. (a) Honeycomb lattice of graphene. The shadowed area delineates the unit cell of graphene with its two nonequivalent atoms labeled by A and B. (b) Band energy dispersion showing the degenerate K and K′ points obtained via tight binding approximation. (c) The conical-shape dispersion around the charge neutrality point. (Taken from J. Güttinger et al. Rep. Prog. Phys. 2012) 2
Figure 1.3. (a) Raman spectra for graphene and bulk graphite with an excitation wave length 514 nm. (b) Comparison of the 2D peaks in graphene and graphite. (c) The four components of the 2D peak ($2D_{1A}$, $2D_{1B}$, $2D_{2A}$, and $2D_{2B}$) in bilayer graphene. (d) Evolution of the height and width of the 2*D* peak spectra comparison with number of layers. (e) The phonon dispersion and electron band structure of graphene, calculated at the experimental and equilibrium lattice spacing. The dotted points are the experimental data and the straight red lines at Γ and K are obtained from Kohn anomalies in the phonon dispersions equations of graphite. Adapted from (A. C. Ferrari, et al. Sol. Stat. Comm. 2007, PRL 2006 & PRB 2000) 4
Figure 1.4. (a) Schematic of graphene field effect transistor of SiO2/Si substrate. (b) Ambipolar electrical transport in single layer graphene. The resistivity as function of back gate voltage (Vg) at temperature of 1K. (Adapted from A. K. Geim and K. S. Novoselov, Nature Materials 2007) 5
Figure 1.5. (a) Graphene Hall measurement configuration. (b) The sketch of Hall resistance as a function of magnetic field (B). (c) The gate capacitance of oxide layer (C_g) can be obtained from the slope of charge carrier density versus gate voltage. 6
Figure 1.6. (a)The conductivity as a function of gate voltage. The solid red line corresponds to linear fit of ($\delta\sigma/\delta V_g$). (b) The measured Hall resistance as a function of magnetic field (B). The solid black line is the experimental data and the red line is the line fit used to obtain the slope. (c) The gate capacitance of oxide layer (C_g) obtained from the slope of charge carrier density as a function of gate voltage. 6
Figure 2.1. The plasma-enhanced chemical vapor deposition setup with inductively coupled plasma source. (Taken from Research institute of precision instruments) 11
Figure 2.2. Diagram of the chemical vapor deposition grown graphene transfer method from copper foil to the silicon dioxide substrate. 12
Figure 2.3. Diagram of photolithography patterning and metal deposition. 13
Figure 2.4. (a) The large photolithographic pattern after Au deposition on SiO_2/Si substrate. (b) Inside view of the large pattern after photolithography and Au deposition for the exfoliated graphene sample. (c) and (d) patterns of CVD-grown graphene Hall bars. 14
Figure 2.5. (a) The copolymer resist ethyl lactate and (b) polymethylmethacrylate resulting thickness of resist with coating speed and diluted percentage. (Taken from microchem corp.) 15
Figure 2.6. Diagram of E-beam lithography patterning and metal deposition. 16
Figure 2.7. Scanning electron microscope image of E-beam lithographic (a-b) exfoliated graphene patterns (c) CVD grown graphene Hall bar pattern. 16
Figure 2.8. (a) The Au patterning on SiO2/Si substrate using metal masks. (b) The Au patterning on CVD grown graphene on SiO2/Si substrate using Al metal masks. 17
Figure 2.9. (a) The four-probe electrical transport measurement setup of graphene using Lock-in technique and controlled by LabView software. (b) The two-probe electrical transport measurement using the same Lock-in technique. 18
Figure 2.10. (a) The transport measurement configuration of the graphene Hall bar device (b) The LabView setup during data acquisition of graphene electrical transport measurements. 18
Figure 3.1. (a, b, c) Optical microscopy images of single-, bi-, and trilayer exfoliated graphene devices after photolithography. (d, e, f) Optical microscopy images after e-beam lithography. (g) Raman spectra of pristine single-, bi-, and trilayer graphene. (h) Lorenz curve fitting of the 2D peak for bilayer and (i) fitting for trilayer graphene. 23
Figure 3.2. Raman spectra of (a,c,d) pristine and DUV irradiated single, bi- and trilayer graphene for (t= 5, 10, 15, and 30 min), (b,d,f) Raman G and 2D spectra of pristine and DUV modified SLG for clarity. 24
Figure 3.3. (a-c) Shift of G and 2D peak positions of SLG, BLG, and TLG for period of DUV irradiation time. (b) The ratio of peak intensities ratio of G and 2D for SLG, BLG, and TLG are plotted as a function of DUV irradiation time. 24
Figure 3.4. The general trend of the transformation of the Dirac point position for SLG, BLG, and TLG, before (left side) and after (right side) DUV irradiation 25
Figure 3.5. Resistivity as a function of back gate voltage (Vg) for the (a) SLG pristine and after different periods of DUV irradiation time. (b) BLG pristine and after different periods of DUV irradiation time. (c) TLG pristine and after different periods of DUV irradiation time 26
Figure 3.6. (a) The shift of Dirac point positions with different periods of irradiation tine for SLG, BLG, and TLG. (b) Change of charge carrier density (Δn) as a function of irradiation time for SLG, BLG, and TLG. (c) The electrons and holes mobilities as a function of irradiation time for SLG, BLG, and TLG. 27
Figure 4.1. Diagram of DUV light exposed CVD grown single-layer graphene FET structure. 31
Figure 4.2. (a) Raman spectra of pristine CVD grown graphene and DUV light modified CVD grown graphene (b) Raman G and 2D spectra of pristine and DUV exposed graphene (c) The ratio of the intensities for the 2D and G peaks and the ratio of the intensities for the D and G peaks are plotted as a DUV exposure time. 33

Figure 4.3. (a) Resistivity as a function of back gate voltage (Vg) for the single layer CVD grown graphene before and after DUV light for different exposure time (b) Charge carrier concentration as a function of DUV light exposure time at different gate voltage (c) Mobility as a function of DUV light exposure time at different gate voltage; Inset shows the Dirac points shift as function of DUV light exposure time. 33
Figure 4.4. (a) Resistivity as a function of gate voltage (Vg) black curve of the pristine single layer CVD grown graphene, red curve of 100 minutes DUV exposed single layer CVD grown graphene and the blue curve shows the doping stability after two months (b) Resistivity as a function of gate voltage (Vg) black curve of the pristine single layer CVD grown graphene, red curve of DUV light exposed and blue curve with two distinct Dirac points shows the combination of pristine+DUV exposed region (c) I-V characteristics at different gate voltages pristine+DUV exposed region. 35
Figure 5.1. (a) Raman mapping of peak intensity ratios of 2D and G and (b) peak intensity ratios of D and G. (c) Mapping of position of the G peak and (d) position of the 2D peak. (e) Diagram of the doping mechanism during DUV irradiation in different gas atmospheres. 39
Figure 5.2. (a) Raman spectra of pristine graphene, DUV irradiated graphene in O_2 flow (denoted by DUV/O_2), DUV irradiated graphene in N_2 flow (denoted by DUV/N_2) after DUV/O_2. DUV treatments were done for 60 minutes. (b) Raman spectra of pristine graphene, graphene in O_2 flow for 60 minutes, graphene in N_2 flow for 60 minutes after the O_2 flow treatment. (c) Shift of the Raman band position between treatments with and without DUV irradiation, changes in the G band position for pristine graphene, graphene in O_2 flow, graphene in N_2 flow. (d) The changes in the 2D band position for pristine graphene, graphene in O_2 flow, graphene in N_2 flow. 40
Figure 5.3. Resistivity as a function of back gate voltage (V_g) for (a) DUV irradiated graphene in O_2 flow, (b) DUV irradiated graphene in N_2 flow after DUV/O_2. Resistivity as a function of back gate voltage (V_g) for (c) graphene in O_2 flow, (d) graphene in N_2 flow after the O_2 flow treatment. 41
Figure 5.4. Carrier concentration change (Δn) as a function of exposure time for DUV irradiated graphene in O_2 flow and DUV irradiated graphene in N_2 flow after DUV/O_2. Charge neutrality point for graphene in O_2 flow and graphene in N_2 flow after the O_2 flow treatment. 42
Figure 5.5. (a) C 1s XPS spectra of pristine CVD grown graphene (black curve), after being oxidized with DUV/O_2 (red curve) and then recovery with DUV/N_2 treatment. (b) The deconvoluted spectra after DUV and oxygen treatment show the appearance of the oxygen containing groups on the graphene. 43
Figure 5.6. (a) Resistivity as a function of back gate voltage after DUV illumination in N_2 gas flow on pristine graphene. (b) Resistivity of graphene as a function of back gate voltage after exposure to N_2 gas flow. (c) Resistivity of p-doped graphene as a function of back gate voltage after N_2 gas flow. The graphene sample was p-doped by 60 min DUV/ O_2 treatment before the measurement. (d) Change of charge neutrality point (V_{CNP}) as a function of exposure time for the N_2 gas treatments. (e) Stability of doping after DUV/O_2 treatment. Resistivity as a function of gate voltage remains almost unaffected after 2 months in the atmospheric environment. 44
Figure 5.7. (a) Photo-conductance measurement of the graphene transistor in DUV, DUV/O_2 and DUV/N_2 environments. (b) Continuous sweep of conductance curve versus time with DUV irradiation (black) DUV /O_2 (red) and DUV/N_2 (blue).45
Figure 6.1. (a) Scanning electron micrograph (SEM) image of the device fabricated by simultaneous process of photo- and e-beam lithography. The graphene appears as a dark color in the middle of micrograph. (b) Diagram of e-beam exposure on graphene channel. 48
Figure 6.2. (a) Raman shift for various e-beam irradiation doses. The peaks *D, G* and *2D* appear around 1347, 1587 and 2690 cm^{-1}, respectively. The disorder induced *D* and *D'* peaks is raised after e-beam irradiation. (b) Evaluation of Raman spectra by the multiple Lorentzian curve fittings of *D, G* and *D'* peaks, respectively with measured data. 49
Figure 6.3. (a) Position and full width half maximum (FWHM) of *D* peak as a function of e-beam irradiation dose. (b) Position of *G* and *2D* peak as a function of e-beam irradiation dose. Inset: Crystalline size (L_a) as a function of e-beam irradiation dose. 50
Figure 6.4. Implementation of Eq. (3) on I_D/I_G as a function of average distance L_a between defects, induced by e-beam irradiation. Instead of the integrated area ratio, we use the intensity ratio, because below L_a ~2 nm, the *G* and *D'* peaks overlap. The solid red line is the theoretical modelling data of Eq. (3) and the black dots are the experimental data. (b) The theoretical fit obtained by using Eq. (3) and experimental data of I_D/I_G vs. L_a are plotted on a log-log scale for clarity. 51
Figure 6.5. (a) Resistivity of graphene as a function of back gate voltage (V_g) for various doses. (b) Mobility of graphene as a function of e-beam irradiation dose at different gate voltage. The inset shows the resistivity at the Dirac point as a function of the e-beam irradiation dose. 52
Figure 7.1. Figure 1. (a) Diagram of SWCNT on polypropylene carbonate substrate with Ag contacts in two probe impedance measurement setup (b) Diagram of Corbino reflectometry setup with panel mount SMA connector for microwave frequency range. 57
Figure 7.2. (a) Raman spectra of SWCNT thin film network on PC substrate with different densities of CNT used for two-probe and Corbino geometry impedance measurements. (b) Transmittance as a function of wavelength for various density networks. Inset shows the photograph of SWCNT network on polypropylene carbonate flexible substrate. 57
Figure 7.3. (a) AFM image of a nanotube thin film area 4x4 μm^2. (b) Thickness profile taken by drawing the line in the middle of topography image. The average thickness of the SWCNT film is 27 nm and RMS roughness is around 12 nm. The SWCNT bundle size is approximately 15-20 nm. 58
Figure 7.4. Bode plots showing the real (a) and imaginary (b) parts of impedance as a function of frequency for SWCNT thin film networks with different density of samples S1, S2, and S3. 58
Figure 7.5. (a) Nyquist plot showing the imaginary part (-Z'') vs real part (Z') of impedance of SWCNT thin film networks with different densities of samples S1, S2, and S3. The inset shows a simple equivalent circuit composed of parallel combination of resistor and capacitor. The electrochemical impedance spectroscopy (EIS) simulation plot (b) for sample S1 with resistance R =550

Ω and capacitance C =1.89 × 10^{-9} F, (c) for sample S2 with resistance R = 418 Ω and capacitance C = 5.16 × 10^{-9} F, and (d) for sample S3 with resistance R = 338 Ω and capacitance C = 7.83 × 10^{-8} F. 59
Figure 7.6. (a) Frequency dependence of real component and (b) imaginary component of impedance with various densities of samples measured by two probe method. Length and width of the sample are 1.5 cm and 0.5 cm, respectively. 61
Figure 7.7. Impedance as a function of frequency of SWCNT thin film networks with various densities. (a) Real component and (b) imaginary component measured by Corbino reflectometry (panel mount SMA connector with inner and outer diameters a = 0.5 mm and b = 1.9 mm, respectively) setup. 61
Figure 7.8. The impedance at cut-off frequency as a function of cut-off frequency (f_0) of SWCNT thin film networks with different densities. In the two-probe measurement, the width was 0.5 cm and lengths were 1.5, 3 and 6 cm, respectively. In the Corbino reflectometry setup the circular shape sample has a diameter of D = 1.9 mm. 62

Chapter 1

1 Introduction

1.1 Overview and history of graphene

The history of graphene begins with graphite which consists of stacked layers of carbon atoms. In these stacked layers, the carbon atoms are arranged in a hexagonal lattice and strongly covalent bonds with each other. However, the atoms of two adjunct layers are weakly bound by a van der Waals force. Such a single layer of graphite is called graphene. This two-dimensional sp^2-hybridized network of carbon atoms has received a remarkable cornucopia of new physics due to its novel linear dispersion relation, together with unique electronic properties such as ambipolar transport, Dirac particle quantum Hall effect including anomalous integer quantum Hall effect and quantized opacity. The scientific importance of graphene becomes significantly greater in the field of materials science and condensed matter physics, because graphene makes a unique model system which is reliable for studying a variety of unusual phenomena and technological applicability. The perfect honeycomb monolayer structure of carbon atoms is treated as a theoretical model for describing the properties of various carbon-based materials such as graphite, fullerenes, and carbon nanotubes. The theoretical investigation of two-dimensional (2D) crystals revealed that graphene would be unstable in reality due to thermal fluctuations [1-5]. Various experimental results have been in accord with this theoretical presumption that graphite thin films become thermodynamically unstable below a certain thickness. Furthermore, the initial steps were set out by Geim, Novoselov, and Kim when graphene emerged as a real sample with isolation of astonishingly thin carbon films and eventually monolayer graphene by simple exfoliation using Scotch tape [6-8]. No further proof is required for its importance in fundamental physics, whereas its effectiveness will be more evident after its appearance in commercially applicable products. Much research effort is being devoted to understanding the main physical properties of graphene. In particular, the remarkable electronic properties of graphene have provided significant motivation towards a better understanding of their physical features and have been transformed into real technological applications. However, the absence of band gap is a main obstacle, which limits its use for electronic logic devices. Thus, development strategies have been introduced for inducing band gap in graphene, some of which are being successfully utilized to tailor the electronic properties of graphene by controlled tunings, which include chemical doping, dual gate with external electric field, etc.

1.2 Basic electronic properties of carbon based structures

The atomic structure of graphene is solely defined as a single layer of carbon atoms arranged in a hexagonal lattice. A single carbon atom has four valence electrons with a ground-state electronic shell configuration of $2s^2\ 2p^2$. In case of graphene, the carbon-carbon chemical bonds are due to hybridized orbitals generated by the superposition of 2s with $2p_x$ and $2p_y$ orbitals. In the honeycomb lattice, the planer orbitals construct σ-bonds with the three nearest-neighbor carbon atoms, and the remaining $2p_z$ orbitals having π symmetry orientation play a significant role in the electronic properties of graphene. The detailed layout of electronic structure of graphene is shown in Fig. 1(a). It can be used as a fundamental building-block paradigm to other carbon-based materials, since it can be folded into fullerenes, rolled up into nanotubes, or stacked layer by layer into graphite, as shown in Fig. 1(b).

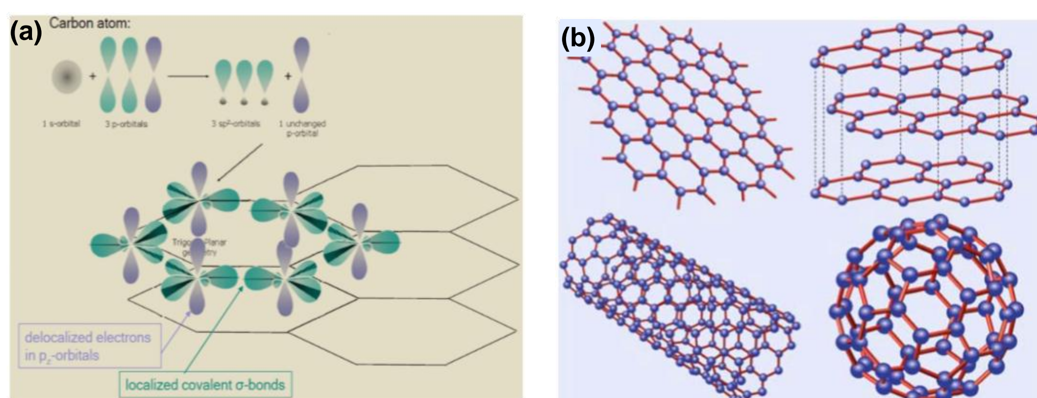

Figure 1.1. (a) The ground-state electronic shell configuration of s and p hybridized orbitals generated by the superposition of 2s with $2p_x$ and $2p_y$ orbitals. (b) Graphene is a honeycomb lattice of carbon atoms. Graphite can be viewed as a stack of graphene layers. Carbon nanotubes are rolled-up cylinders of graphene and fullerenes (C_{60}) are molecules consisting of wrapped graphene by the introduction of pentagons on the hexagonal lattice. (Adapted from A Catro Neto 2009 & A. Giem 2010)

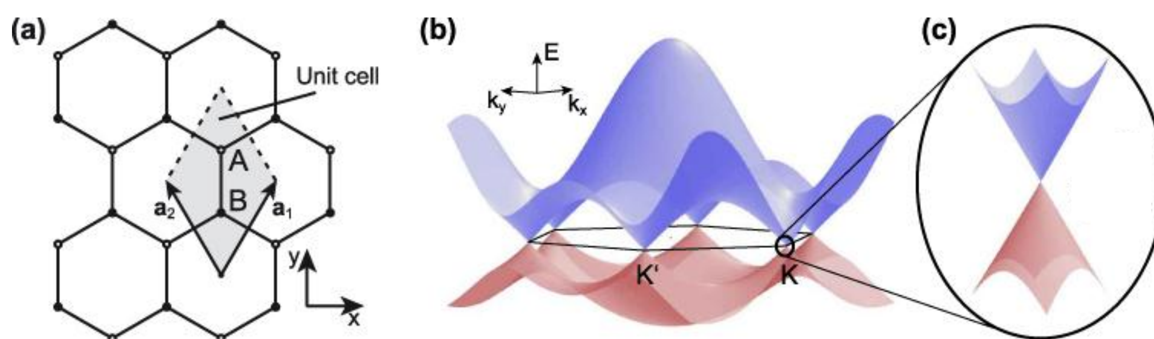

Figure 1.2. (a) Honeycomb lattice of graphene. The shadowed area delineates the unit cell of graphene with its two nonequivalent atoms labeled by A and B. (b) Band energy dispersion showing the degenerate K and K′ points obtained via tight binding approximation. (c) The conical-shape dispersion around the charge neutrality point. (Taken from J. Güttinger et al. Rep. Prog. Phys. 2012)

In Fig. 2 (b) and (c), one can see the band structure of graphene obtained from such a simple tight-binding model, which yields symmetric conduction and valence bands with respect to the Fermi energy, called the

charge neutrality point or Dirac point at 0 eV. The Dirac points are the junctions between the valence band and the conduction band. Graphene valence and conduction bands are degenerate at 6 points located on the corners of the Brillouin zone, also called K and K′ valleys, which are the two nonequivalent corners of the zone. The vertical axis is energy, while the horizontal axes are the momentum space on the graphene lattice. The hexagonal region (Brillouin zone) has a side length of $4\pi/3a$ and delineates the Fermi surface of the graphene. The low-energy dispersion near the valleys exhibits a circular conical shape. The dispersion relation of graphene with massless relativistic particles obtained from the Dirac equation shows that graphene charge carriers can behave as Dirac fermions [5].

1.3 The structural and transport properties of graphene

1.3.1 Structural characterization using Raman spectroscopy

Raman spectroscopy is used as a standard nondestructive tool for the electronic structure characterization of carbon based crystalline films. It has also been used to measure the number of graphene layers and to analyze disorder, strain and doping in graphene. The D peak is attributed to A_{1g} symmetry phonons near the K-zone boundary. These phonons are not Raman active due to the momentum conservation in the scattering, and require a defect for their activation. The G peak corresponds to the E_{2g} optical phonon at the Brillouin zone center and 2D peak is the second order of the D peak. It originates from a process where momentum conservation is satisfied by two phonons with opposite wave vectors. The ratio and positions of 2D and G peaks are used to identify the number of layers of graphene. The number of layers is also estimated from the full width half maxima (FWHM) of 2D peaks. Figure 1.3(a) shows the Raman spectra of graphene and bulk graphite with 514 nm laser wave length. Figure 3(b) shows the comparison of the 2D peaks in graphene and graphite. The four components $2D_{1A}$, $2D_{1B}$, $2D_{2A}$, and $2D_{2B}$ of the 2D peak after Lorentzian fitting in bilayer graphene with an excitation wavelengths 514.5 and 633 nm are shown in Fig. 1.3(c). Figure 1.3(d) shows the evolution of the height and width of the 2D peak spectra comparison with the number of layers. The variation in the positions and shape of the 2D peak for different numbers of layer can be clearly seen. The phonon dispersion and electron band structure of graphene are shown in Fig. 1.3(e), where the black lines correspond to the calculated band structure for graphene with equal lattice spacing, whereas the red, blue and green dotted points are the experimental data from various references. The straight red lines at Γ and K represent the E_{2g} and A_{1g}-like eigenvectors of aromatic clusters on those of graphene, respectively, which are obtained from Kohn anomalies in the phonon dispersions equations of graphite.

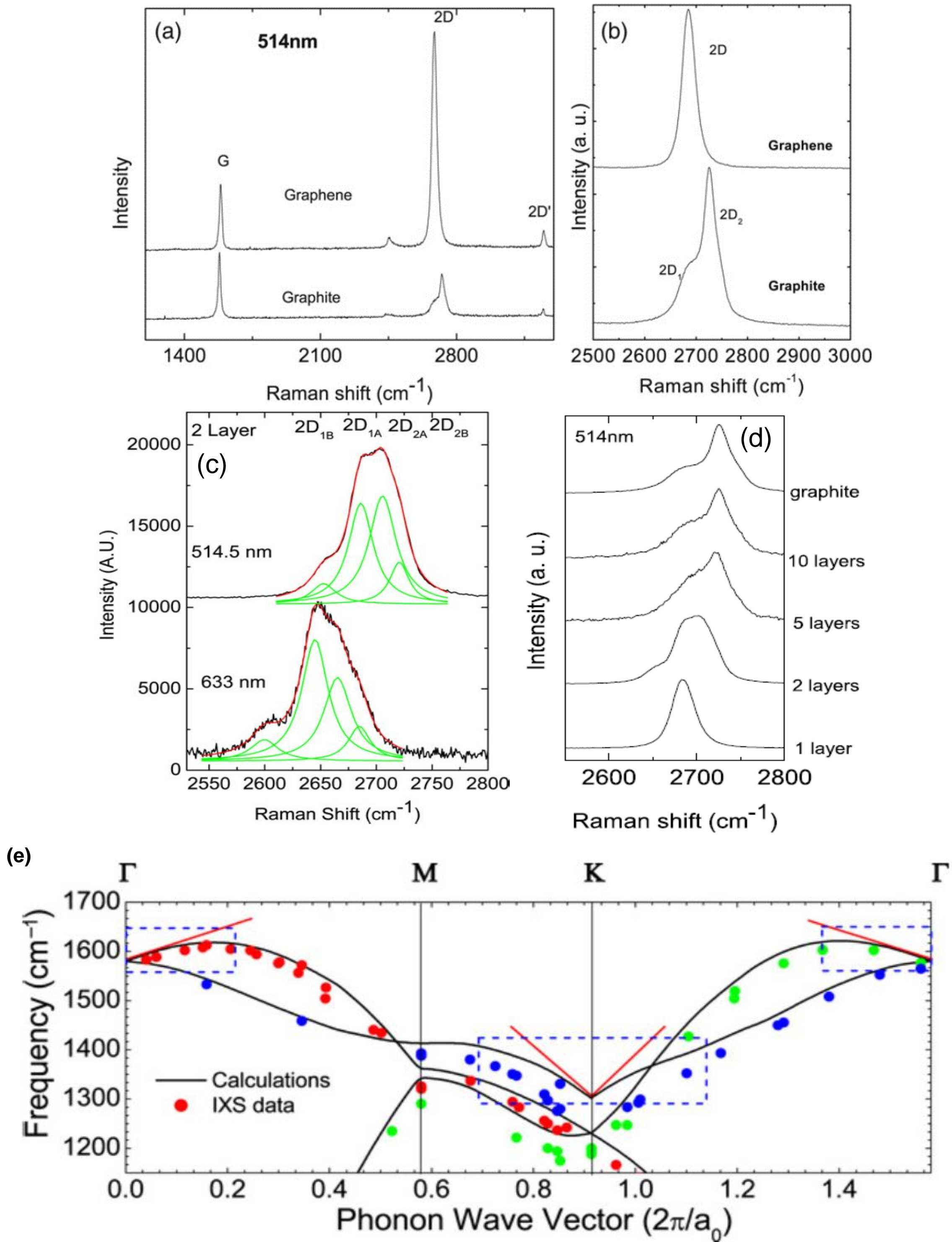

Figure 1.3. (a) Raman spectra for graphene and bulk graphite with an excitation wave length 514 nm. (b) Comparison of the 2D peaks in graphene and graphite. (c) The four components of the 2D peak ($2D_{1A}$, $2D_{1B}$, $2D_{2A}$, and $2D_{2B}$) in bilayer graphene. (d) Evolution of the height and width of the 2*D* peak spectra comparison with number of layers. (e) The phonon dispersion and electron band structure of graphene, calculated at the experimental and equilibrium lattice spacing. The dotted points are the experimental data and the straight red lines at Γ and K are obtained from Kohn anomalies in the phonon dispersions equations of graphite. Adapted from (A. C. Ferrari, et al. Sol. Stat. Comm. 2007, PRL 2006 & PRB 2000)

1.3.2 Transport properties of graphene

Much attention has been devoted to the transport properties of graphene since the experimental realization of isolated graphene [6]. However, the effective implications depend mostly on patterning device architectures in which their electronic properties can be tuned in a predetermined and controlled way. An interesting phenomena can be observed experimentally when a graphene device with an isolated oxide gate experiencing strong tunability of carrier density under a modulating electrical field and an isotropic cone-like structure of the energy relation is observed. Robust degeneracy at the Dirac point is split and this isotropic cone-like structure of the energy relation is now composed of two distinct valley structures with highly anistropic dispersions [9]. Figure 4 (a) shows the schematic of graphene field effect transistor of SiO_2/Si substrate with Au electrodes. Figure 1.4 (b) shows the ambipolar electrical transport in single layer graphene. The positive (negative) back gate voltage (V_g) induces the concentration change of electrons (holes) for the field effect device on silicon dioxide substrate. The prompt decrease in resistivity (ρ) on addition of charge carriers corresponds to the high mobility of the graphene device. The Dirac cones in the insets in Fig. 1.4 (a) represent the modulation of Fermi energy (E_F) with changing V_g changes [10].

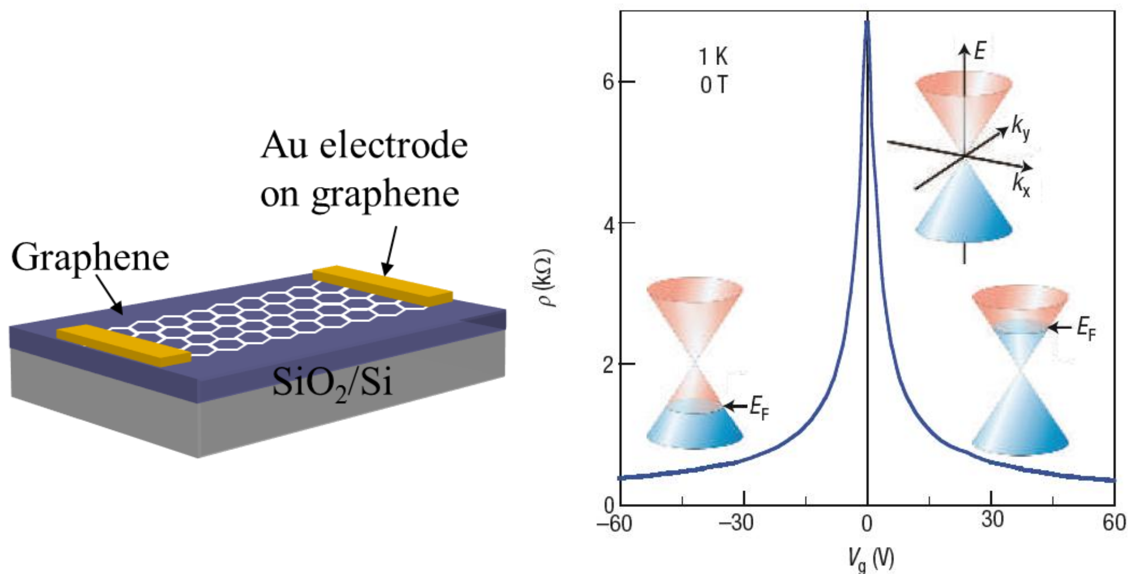

Figure 1.4. (a) Schematic of graphene field effect transistor on SiO_2/Si substrate. (b) Ambipolar electrical transport in single layer graphene. The resistivity as function of back gate voltage (Vg) at temperature of 1K. (Adapted from A. K. Geim and K. S. Novoselov, Nature Materials 2007)

The carrier density and mobility of the graphene devices can be calculated by various methods, which are given below:

1) The first method is to calculate the mobility of the graphene device using the Drude model: $\mu=1/ne\rho$ where the resistivity of the graphene device is $\rho=RW/L$, R (resistance), W (width of graphene channel), and L (length of graphene channel). The "n" is the carrier density, which can be calculated from Hall

measurements ($n=1/(R_{xy}/B)e$). The Hall measurement configuration and the sketch of the obtained Hall resistance as a function of magnetic field (B) are shown in Fig. 1.5(a) and (b), respectively.

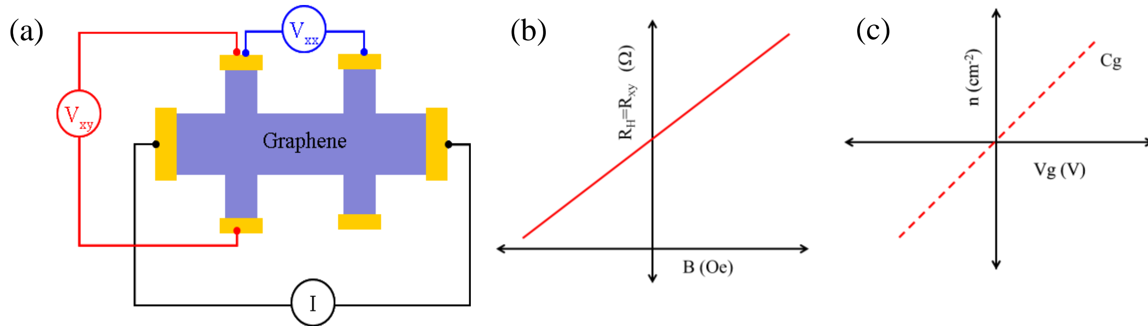

Figure 1.5. (a) Graphene Hall measurement configuration. (b) The sketch of Hall resistance as a function of magnetic field (B). (c) The gate capacitance of oxide layer (C_g) can be obtained from the slope of charge carrier density versus gate voltage.

2) The second method for the calculation of mobility is $\mu = (1/C_g)(\delta\sigma/\delta V_g)$, where C_g is the gate capacitance of oxide layer and $\delta\sigma/\delta V_g$ is the slop of conductivity (σ) as the function of the gate voltages (V_g) of the graphene device. The calculation of $\delta\sigma/\delta V_g$ is shown in Figure 1.6(a) and gate capacitance can be obtained from the slope of charge carrier density as a function of the gate voltage.

3) The third method for the graphene mobility calculation is $\mu=1/ne\rho$, where $ne= C_g (V_g-V_{Dirac})$, C_g is the gate capacitance of oxide layer, V_g is the gate voltages and V_{Dirac} is the voltage of the graphene device at the Dirac point

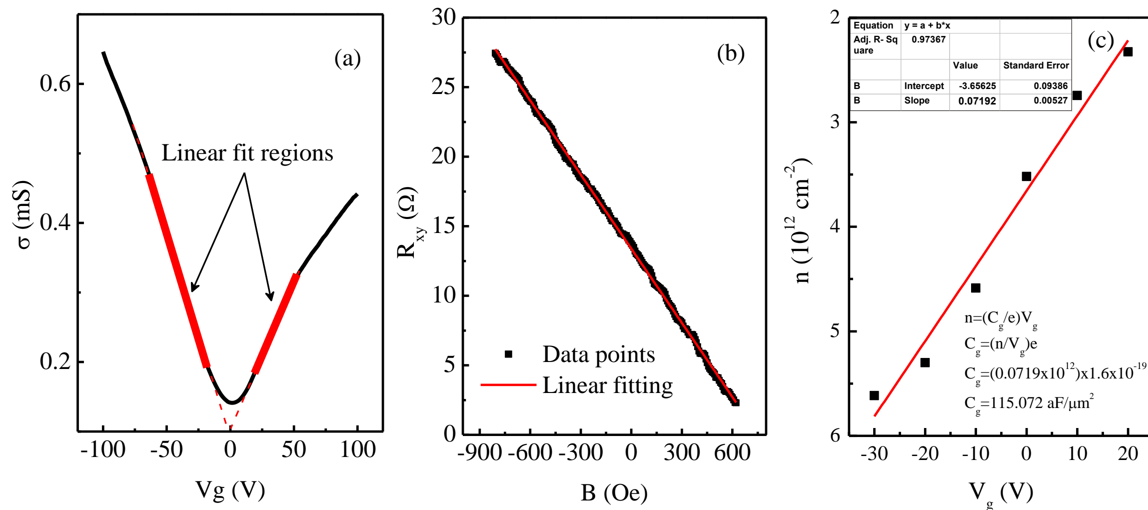

Figure 1.6. (a)The conductivity as a function of gate voltage. The solid red line corresponds to linear fit of ($\delta\sigma/\delta V_g$). (b) The measured Hall resistance as a function of magnetic field (B). The solid black line is the experimental data and the red line is the line fit used to obtain the slope. (c) The gate capacitance of oxide layer (C_g) obtained from the slope of charge carrier density as a function of gate voltage.

1.4 Motivation of work

In this section, I explain the motivation for the work presented in this thesis. The experimental realization of the doping effect in graphene opened the way for the exploration of many fundamental properties. In this thesis I focus on the following issues:

- How essential is it to tune the Fermi level of the carriers in graphene?
- How are the structural properties affected by doping of graphene?
- How are the electrical transport properties tuned by varying the carrier density with doping?
- How does the effect of ultraviolet light tailor the Fermi level of graphene?
- What is the influence of a p-n junction in graphene on its transport properties?
- How do the doping properties depend on the layers, when we go from a linear dispersion (single-layer graphene) to the parabolic dispersion that is present in bi- or trilayer graphene?
- How do the different environments affect the structural and electrical properties of graphene?
- How can the structural disorder be controlled during doping?
- High frequency (40 MHz to 20 GHz) applications of carbon nanotube network for flexible and transparent electronics with different measurement geometries.

1.5 Organization of the thesis

The thesis is organized as follows:

Chapter 2 is devoted to a detailed overview of device fabrication methods and characterization tools. This chapter includes the production of graphene using a mechanical exfoliated technique and large scale growth of graphene using chemical vapor deposition method. The graphene transfer procedure is also addressed in this chapter. The device fabrication techniques such as photolithography and electron beam lithography pattering processes are also described. The Raman spectroscopy and transport measurement techniques using standard low noise lock-in two and four probe methods are given in this chapter.

Chapter 3 of the thesis reports the tuning of electronic properties of single-, bi-, and trilayer mechanically exfoliated graphenes using deep ultraviolet (DUV) light. Raman spectroscopy and charge transport measurements reveal that DUV light imposes p-doping to single-, bi-, and trilayer graphenes. The Raman peak frequencies and intensity ratio of single-, bi-, and trilayer graphenes are analyzed as a function of irradiation time. The Dirac point is also analyzed as a function of irradiation time indicating the p-type doping effect for all single-, bi-, and trilayer graphenes. Our study demonstrates that DUV irradiation is a non-destructive approach to tailor the electrical properties of single-, bi-, and trilayer graphenes, while maintaining the important structural and electrical properties.

Chapter 4 contains a detailed study of the formation of p-n junction with stable p-doping in graphene field effect transistors using deep UV irradiation. Modification of the electronic properties of single-layer chemical vapor deposition (CVD)-grown graphene by DUV light irradiation is studied in this chapter. The Raman spectra suggests p-doping in graphene field effect transistors (FETs) with DUV irradiation. In the transport measurements, the Dirac point is shifted towards positive gate voltage with increasing DUV light exposure time, revealing the strong p-doping effect without a large increase of resistance. The doping is found to be stable in graphene devices, with a slight change in mobility. A p-n junction is also constructed by DUV light exposure on selected regions of graphene, and investigated by gate voltage dependent resistivity measurements and current-voltage characteristics.

Chapter 5 of the thesis deals with the improvement of the doping technique described in Chapter 4. This work comprises the ultraviolet light induced reversible modulation of doping in graphene transistors with efficient photocurrent generation. The reversible modulation in different gases (dry oxygen and nitrogen environments) moved us firmly towards the controllable doping and de-doping mechanism. Hole doping is observed by DUV irradiation with oxygen flow, but becomes reversed with nitrogen flow in transport measurements supported with Raman and X-ray photoelectron spectroscopy. The generation of efficient photocurrent provides the possibility of integrating high-efficiency optoelectronic devices.

Chapter 6 describes the structural and electrical evolution of chemical vapor deposition grown graphene by electron beam irradiation induced disorder. The defect formation mechanism in chemical vapor deposition grown single-layer graphene devices is investigated by gradually increasing electron beam (e-beam) irradiation doses. The Raman spectra provide evidence of strong lattice disorder due to e-beam irradiation. In particular, the result suggests that the graphene changes from the crystalline form to the nanocrystalline form and then towards the amorphous form with increasing irradiation dose. The defect parameters are calculated by a phenomenological model of amorphization trajectory for graphitic materials. Mobility decreases gradually with a gradual increase of irradiation dose, which implies the formation of localized states in e-beam irradiated graphene. The Dirac point is shifted towards negative gate voltage, indicating n-doping in graphene with an increasing e-beam irradiation dose.

Chapters 7 presents the analysis of single-walled carbon nanotube networks, which are expected to be suitable as miniaturized flexible radio frequency RC filters and also have important implications for high frequency devices. The thickness and roughness of the thin film of SWCNTs are examined by atomic force microscopy. The surface morphology obtained by atomic force microscopy shows that most of the growth on polypropylene carbonate substrate is homogeneous. The frequency-dependent impedance measurements of SWCNTs network on transparent and flexible substrates is performed by using two different techniques, i.e., two probe and Corbino reflectometry setups. The impedance measurements show

that the cut-off frequency decreases with increasing density of SWCNTs. The real part of the impedance as a function of cut-off frequency shows the same slope in both measuring techniques. For the case of two-probe impedance measurements, the measured impedance is large and is mainly due to high contact resistance. As expected, the cut-off frequency not only depends on the density of the network, but on other factors such as geometry in the measurement setup.

Chapter 8 provides a thorough discussion of the doping effect on graphene-based devices and a summary of whole work.

Chapter 2

2 Experimental methods

In this chapter I describe graphene growth, device fabrication processes and experimental details of our measurements.

2.1 Fabrication of graphene flakes by mechanical exfoliation of graphite using the scotch tape technique

The micromechanical cleavage of bulk graphite is also commonly known as the “Scotch tape” method. The silicon substrate with 300 nm silicon oxide as a top layer is glued onto glass slide using double-sided sticky tape. A few pieces of graphite are placed on scotch tape and peeled off many times. This procedure makes fresh graphene layers glued with tape. The scotch tape together with the graphene are pressed onto the SiO_2 substrate. Van der Waals forces make single, multilayer or graphite pieces remain on the SiO_2 after removing the tape. The exfoliated single, bi- or trilayer graphene flakes can be identified using optical microscopy due to the interference effects of light between SiO_2 and graphene.

2.2 Graphene towards large scale production

The mechanical exfoliation technique has a low cost, but, it is highly uncontrollable for the size and number of layers of graphene. Furthermore, the yield of graphene is low and the flakes have rather small dimensions of a few microns. Although most of the fundamental research can be done using this method, alternative techniques for large-scale production of graphene are required. There are two main directions in this area: (i) epitaxial growth of graphene on SiC substrate; and (ii) chemical vapor deposition on metal substrate. The epitaxial growth of graphene on SiC substrate requires very high-temperatures and is relatively expensive. However, chemical vapor deposition (CVD) on metal (Cu, Ni) substrate is relatively cheaper than the growth on SiC and is a more promising approach for large-scale production of graphene. Most of the samples discussed in this thesis were obtained this method with help from Dr. Chanyong Hwang’s group in the Korea Research Institute of Standards and Science, and Prof. Seung-Hyun Chun’s group at Sejong University. The detailed procedure of graphene growth using CVD method on Cu foil is given as: Large-area high-quality monolayer graphene samples were grown on 25 μm thick Cu foils (Alfa Aesar, 99.8 %, #13382) by remote radio frequency (RF) plasma-enhanced chemical vapor deposition (RF-PECVD) system. The graphene growth setup of PECVD with inductively coupled plasma source is shown in Fig. 2.1. The CVD chamber was pumped with pressure up to ~10^{-7} Torr with turbo-molecular-pump.

Polycrystalline Cu foil was accumulated in the chamber. Before starting gas flow into the chamber, the Cu substrate was heated up to 830 °C. H_2 gas was then introduced into the chamber at a flow rate of 40 standard cubic centimeter per minute (sccm). The hydrogen gas was then discharged by RF power of 50 W for two minutes to purge the surface oxides of copper foil. During the growth of graphene, the RF plasma was generated for 3 minutes with a continuous flow of a mixture of argon (40 sccm) and methane (1 sccm) gas at a pressure of 10 mTorr. Subsequently the sample was cooled down to room temperature.

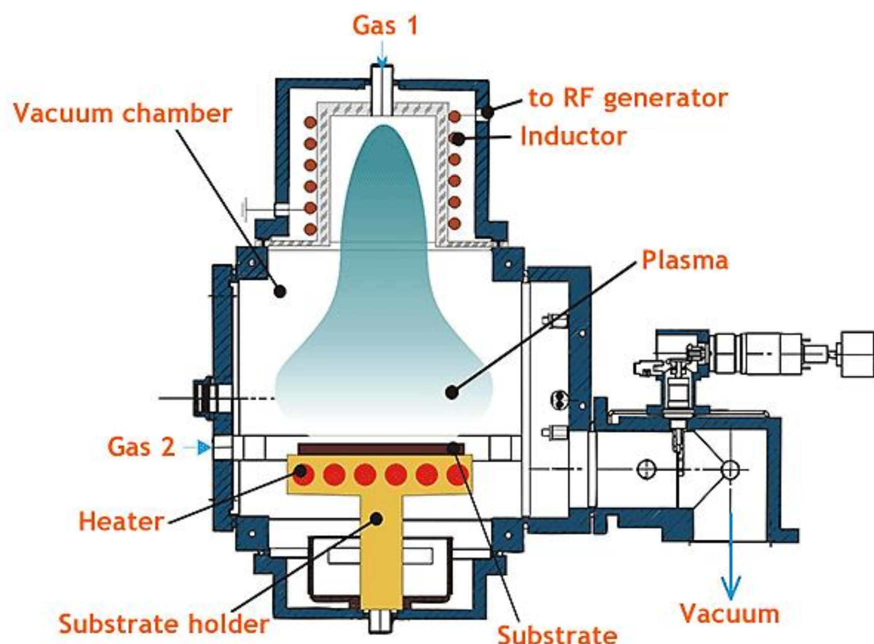

Figure 2.1. The plasma-enhanced chemical vapor deposition setup with inductively coupled plasma source. (Taken from Research institute of precision instruments)

2.3 Graphene transfer method

The graphene film grown on Cu foil was transferred to a SiO_2/Si substrate with the wet transfer method. The Cu foil was spin-coated (850 rpm for 10sec, 2500 rpm for 60sec) with a thin layer of polymethyl methacrylate (PMMA). The bottom Cu foil was then removed by etching in a 1 molar solution of ammonium persulfate (APS) ($(NH_4)_2S_2O_8$), and the PMMA membrane was washed with de-ionized water. The graphene film with the PMMA membrane was then transferred to heavily p-doped Si substrate with a 300 nm thick SiO_2 top layer, and graphene on the SiO_2/Si substrate was kept in acetone for one day to dissolve the PMMA layer. The diagram of the chemical vapor deposition grown graphene transfer method from copper foil to the silicon dioxide substrate is shown in Fig. 2.2.

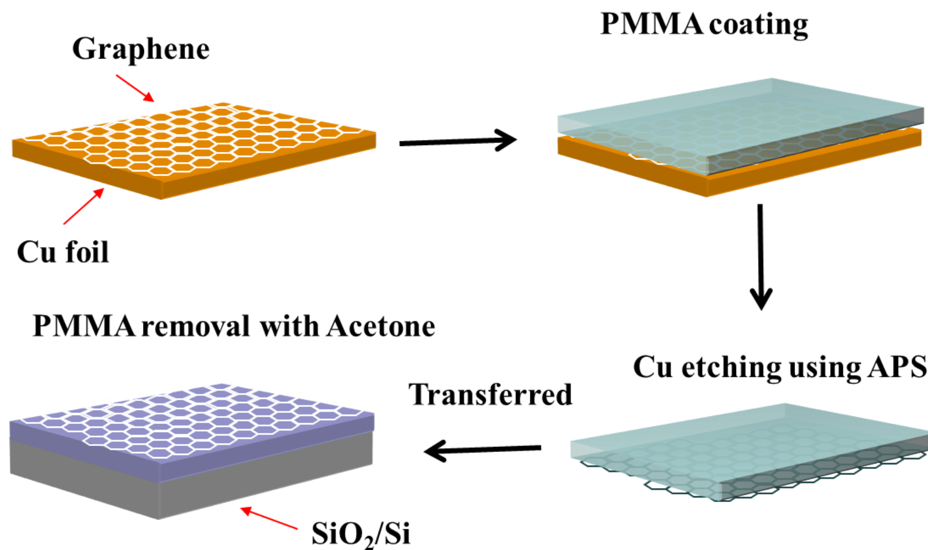

Figure 2.2. Diagram of the chemical vapor deposition grown graphene transfer method from copper foil to the silicon dioxide substrate.

2.4 Fabrication recipe of a graphene device on silicon dioxide substrate

The fabrication of the graphene device proceeds as follows:

The first step is the sonication of SiO_2/Si substrates in acetone for 5 min, and then the substrates are flushed with methanol. This step helps to remove dust particles and other residues from the wafer surface, leading to a better adhesion of graphene. The sample is dried with nitrogen gas and baked on a hot plate at 180℃ for 60 sec to eliminate the water molecules and other solvents. Then graphene is transferred onto the silicon dioxide substrate using the scotch tape method for mechanical exfoliated graphene and the wet transfer method for CVD grown graphene, as mentioned above. After that, photolithography patterning is conducted using the process described below:

2.5 Photolithography patterning on graphene

The bilayer photolithography resist process utilizes an ethyl lactate (EL9) and SPR (3612) coating. Initially, the EL9 resist is spin-coated at the rate of 5000 rpm for 30 sec on the graphene containing piece of silicon wafer. The substrate is then baked at 170℃ in a heating oven for 120 sec, and after that the SPR is spin-coated at the rate of 5000 rpm for 30 sec and baked at 95℃ for 120 sec. The photoresist creates a thin film on the surface of samples with a high-speed spinner, and the baking process helps to dry out the film completely. The dried samples are then exposed under UV light for 4.5 sec using a mask aligner for the desired pattern. The exposed samples are developed in CPD-18 for 55 sec, which removes the exposed region of the SPR. The complete removal of SPR from the desired area is performed by oxygen plasma treatment for 8 minutes. For the removal of EL9, a flood exposure of DUV is conducted for 15 minutes and developed in the mixture of cholorobenzene and xylene (3:1) for 3 minutes. After these steps, the

samples are ready for metal deposition. Since the resist residue in the exposed area still remains, it may cause a high resistance between electrode connections. To avoid this problem, the samples are exposed under oxygen plasma for 15 seconds to completely remove the resist residue. Finally, the metal deposition is carried out using a thermal evaporation system. The diagram of the photolithography patterning procedure is shown in Fig. 2.3. The large photolithographic patterns after Au deposition for exfoliated graphene and Hall bars patterns of CVD-grown graphene are shown in Fig. 2.4.

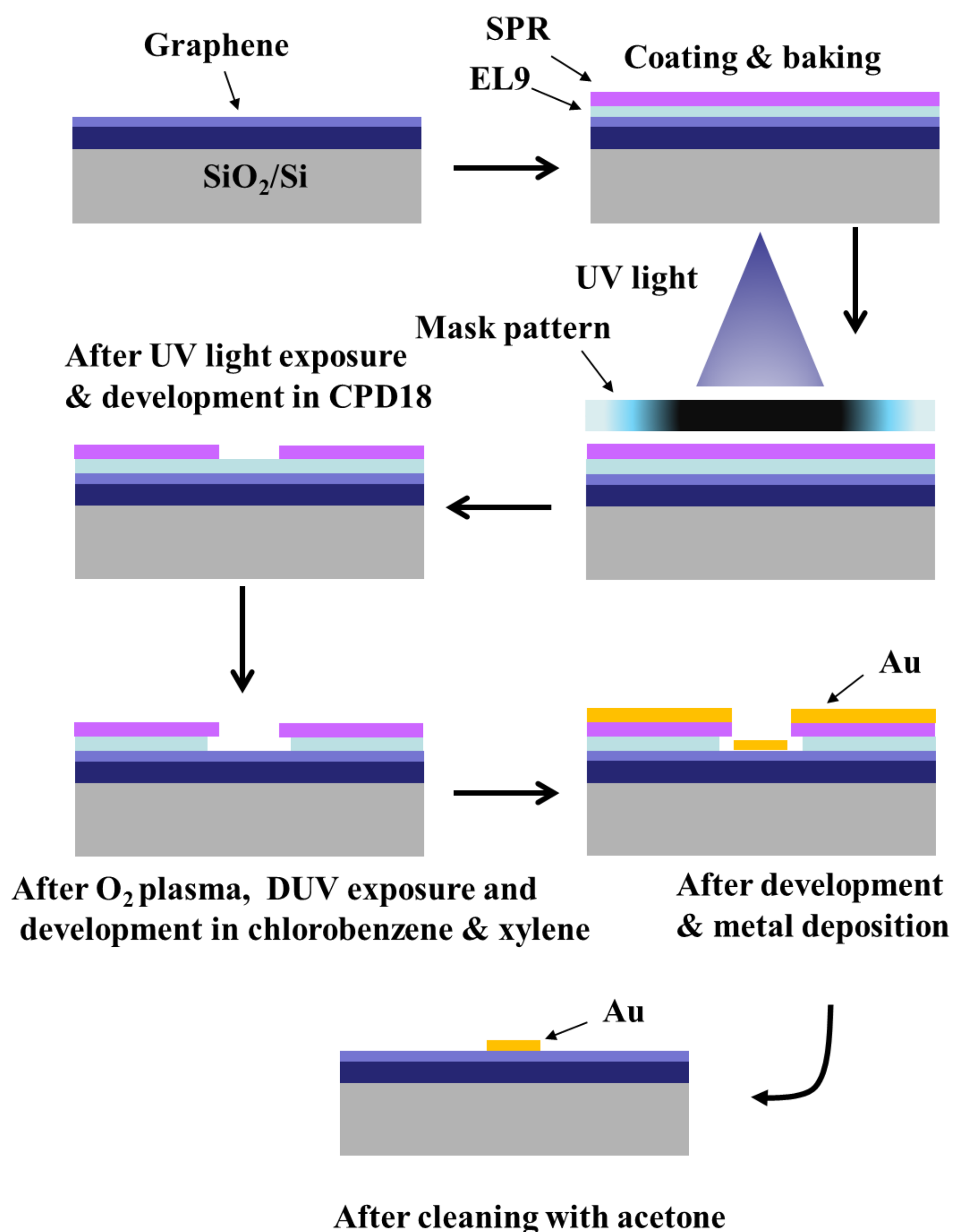

Figure 2.3. Diagram of photolithography patterning and metal deposition.

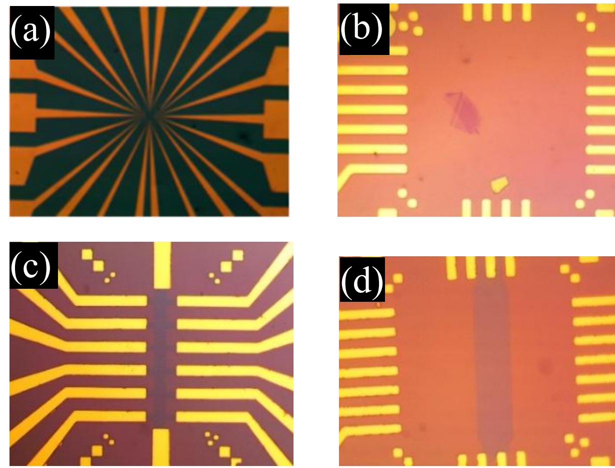

Figure 2.4. (a) The large photolithographic pattern after Au deposition on SiO_2/Si substrate. (b) Inside view of the large pattern after photolithography and Au deposition for the exfoliated graphene sample. (c) and (d) patterns of CVD-grown graphene Hall bars.

2.6 Electron beam lithography patterning on graphene

The bilayer electron beam resist-recipe utilizes copolymer ethyl lactate (EL9) and polymethylmethacrylate (PMMA 950K A2). This recipe is intended for metal liftoff. Spin coating of EL9 is performed at the rate of 5000 rpm for 30 sec on the graphene samples after photolithography patterning. The sample is then baked at 170℃ in a heating oven for 1 hour. Oven heating is preferred to hot plate baking for uniform baking. The second layer is spin-coated by the PMMA resist at 5000 rpm for 30 sec. The resulting thickness of resist film is determined by the coating speed and can also be controlled using a diluted percentage of the EL and PMMA, as shown in Fig. 2.5 (a) and (b), respectively. The thickness ratio between the resist and deposited material has to be at least 2:1 for a better lift-off process.

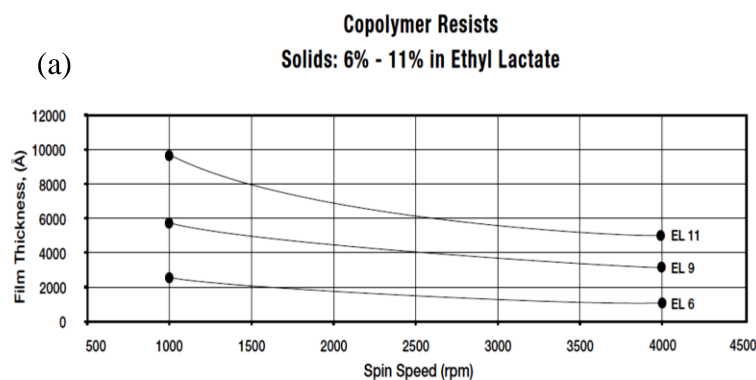

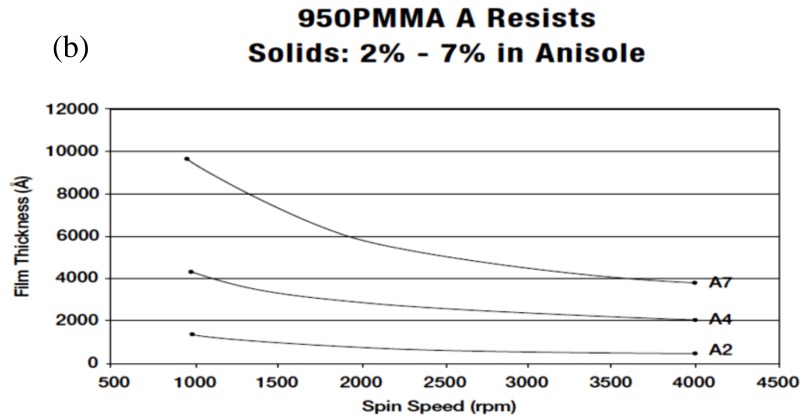

Figure 2.5. (a) The copolymer resist ethyl lactate and (b) polymethylmethacrylate resulting thickness of resist with coating speed and diluted percentage. (Taken from microchem corp.)

The designed pattern of contacts made by means of AutoCAD are written using electron beam lithography (EBL). In this technique, a beam of electrons exposes the required pattern of contacts on the sample covered with polymer (resist). The positive resist is commonly used, although in some cases negative resist may also be preferred. The electron beam breaks polymer chains in the exposed regions. For EBL exposure, we normally use 20 kV of accelerating voltage for electrons with an area dose of 100-150 μC/cm^2. The sample is developed for 10 sec in a 3:1 (60 mL: 20 mL) mixture of IPA (propan-2-ol) and MIBK (4-methyl-2-pentanone) at 20℃. The sample is washed in IPA for more cleaning. To prevent drying marks, the sample is dried by blowing dry nitrogen. After EBL exposure, the broken chains become soluble in the developer. The resultant sample is covered with polymer, except for the places where the contacts have to be deposited. The next stage is to evaporate the metal on the sample for the contacts. The evaporation is done in a vacuum (~ 2×10^{-6} Torr) by thermal evaporation. We usually evaporate thin layer of Cr as an adhesion layer followed by the Au layer. The exact thickness of the deposited materials is monitored by the thickness monitor. The sample covered with metal is dipped into a beaker half filled with acetone for lifting off polymers. The acetone reacts with the resist underneath the metal and breaks it down by lifting up the undesired metal layer. Figure 2.6 shows the E-beam lithography patterning and metal deposition. A scanning electron microscope image of E-beam lithographic patterns on graphene Hall bar is shown in Fig. 2.7. The sample with a pattern of metal contacts is mounted on a chip and then wire-bonded using indium. Finally, the sample is ready to be measured.

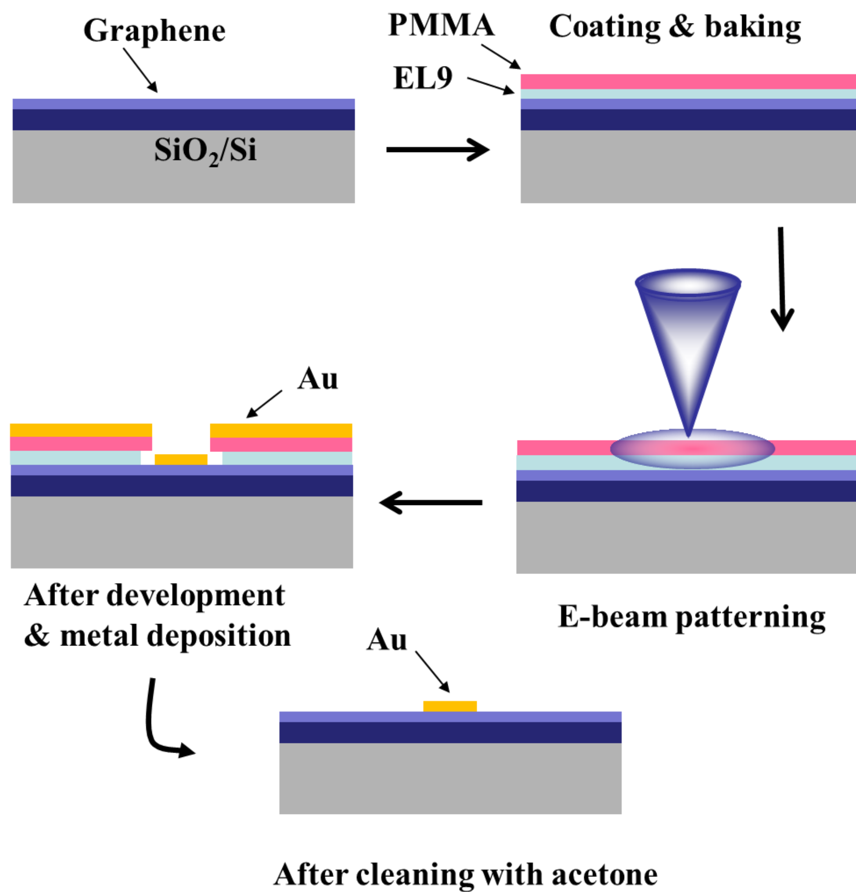

Figure 2.6. Diagram of E-beam lithography patterning and metal deposition.

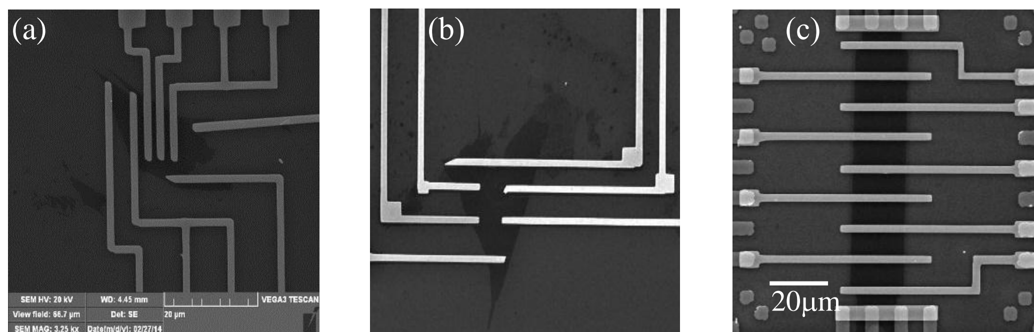

Figure 2.7. Scanning electron microscope image of E-beam lithographic (a-b) exfoliated graphene patterns (c) CVD grown graphene Hall bar pattern.

2.7 Patterning using metal masks

Patterning using a metallic hard mask is an alternate strategy for making a clean residue-free interface between metal and graphene. This scheme is promising for large area patterning on graphene such as CVD grown. However, this method is not useful for small-scale patterning. The Au patterns on the SiO_2/Si substrate and CVD grown graphene on the SiO_2/Si substrate using Al metal masks are shown in Fig. 2.8.

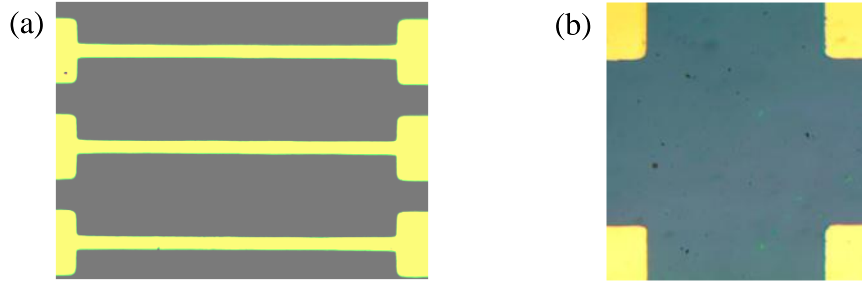

Figure 2.8. (a) The Au patterning on SiO2/Si substrate using metal masks. (b) The Au patterning on CVD grown graphene on SiO2/Si substrate using Al metal masks.

2.8 Setup of the lock-in based electrical transport measurements

The samples are mounted onto the electrical transport measurement setup after bonding with indium wires. The measurements are performed with the standard lock-in technique. The lock-in amplifier (signal recovery 7265 DSP) produces an ac voltage with an operating frequency range from 1 mHz to 250 kHz. This ac voltage is used as a reference for generating the ac-current in an I-V measurement. The back gate voltage can be directly applied to the graphene using a voltage source (Keithley 2400). The two and four probe measurement method of measurements are mainly adopted. In the two-probe setup, the current is applied between two electrodes and the voltage drop is measured between the same set of electrodes. In this method, the measured output resistance contains the contributions of the contact resistance of the metallic contact leads. However, in the four-probe configuration the measured resistance is the sample resistance itself without any contributions from the contacts leads. The two outer electrodes are connected to the current source and two inner electrodes to the voltage probes. The measurement configuration for both the four- and two-probe setup is shown in Fig. 2.9 (a) and (b), respectively. Figure 2.10 (a) shows the electrical transport measurement configuration of the graphene Hall bar device. The data acquisition during measurements are automatically controlled by LabView software. The LabView setup during data acquisition of graphene transport measurements is shown in Fig. 2.10 (b).

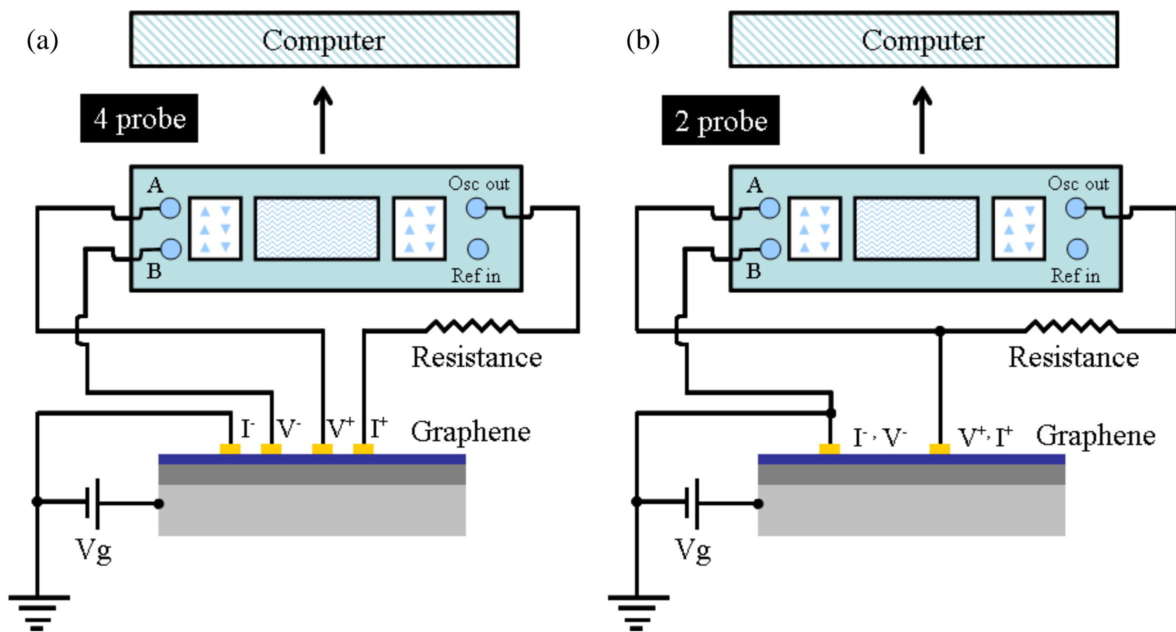

Figure 2.9. (a) The four-probe electrical transport measurement setup of graphene using Lock-in technique and controlled by LabView software. (b) The two-probe electrical transport measurement using the same Lock-in technique.

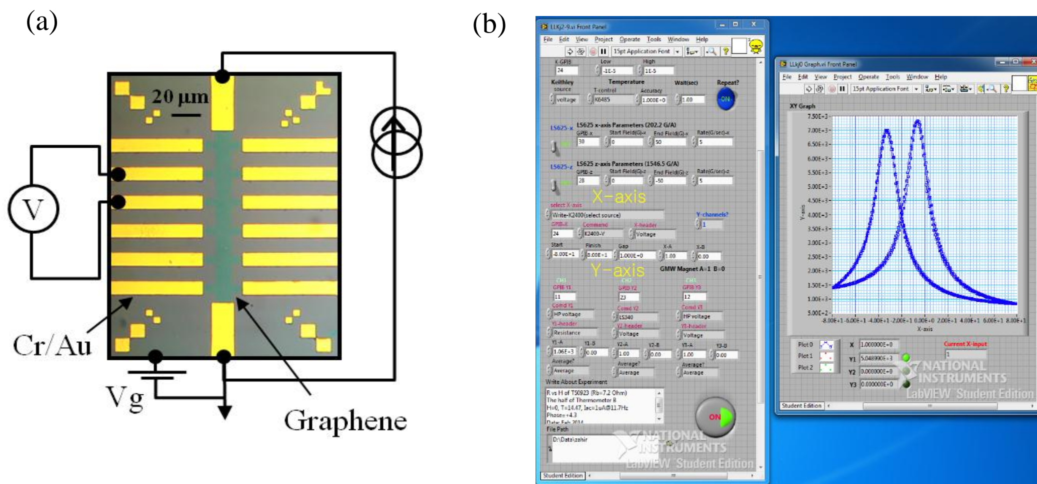

Figure 2.10. (a) The transport measurement configuration of the graphene Hall bar device (b) The LabView setup during data acquisition of graphene electrical transport measurements.

2.9 Doping with DUV irradiation

The modification of graphene properties by DUV is investigated by transport measurements and Raman spectroscopy. The DUV system (Lamp Model: UXM-501 MA) is used for the experiment. The maximum limit of lamp voltage and current are 20 V and 25 A, respectively. The dominant lamp wavelength of DUV light is 220 nm with uniformity of 3.6 % and its average intensity is 11 mW/cm^2.

2.10 Structural disorder with E-beam irradiation

The Tescane VEGA 3 scanning electron microscope (SEM) is used to study the e-beam irradiation effect on graphene. The different dose e-beam irradiation is conducted with the use of the Raith GmbH lithography system, which permits an accurate control of the irradiation dose and the location of the exposed area. The experiment is performed with an accelerating voltage of 20 keV of e-beam at a working distance of 3.55 μm. The Faraday cup of the sample stage is used to measure the beam current, which for this experiment is 14.9 pA.

2.11 Impedance analysis

Two different impedance analyzers are used: (1) Agilent E8362B network analyzer with a frequency range from 10 MHz to 20 GHz, and (2) Agilent 4294A network analyzer with a frequency range from 40 Hz to 110 MHz for high frequency measurements of CNT network on flexible on PC substrate.

Chapter 3

3 Tuning the electrical properties of exfoliated graphene layers by deep ultraviolet irradiation

It is a matter of huge concern in graphene-based nano- and optoelectronic devices to tune the electrical properties of graphene layers, while sustaining its unique band structure and their electrical holdings. Here, we report the tuning of electronic properties of single-, bi-, and trilayer mechanically exfoliated graphenes by deep ultraviolet irradiation (DUV). Raman spectroscopy and electrical transport measurements reveal that DUV light imposes p-doping to single-, bi-, and trilayer graphenes. The shift of the G and 2D peak wave number and intensity ratio of single-, bi-, and trilayer graphenes are evaluated as a function of irradiation time. The Dirac point shift is analyzed as a function of irradiation time, which indicates the p-type doping effect for all single-, bi-, and trilayer graphenes. Our investigation demonstrates that DUV irradiation is a non-destructive approach to tailor the electrical properties of single-, bi-, and trilayer graphenes, while maintaining their important structural and electrical characteristics.

3.1 Introduction

Graphene, a two-dimensional sp^2-hybridized network of carbon atoms with perfect crystalline structure, enables remarkable exploration of fundamental physics as well as the exciting potential applications for electronic devices [7, 10]. In addition, graphene attracts great attention due to its unique electronic properties, such as ambipolar transport with high charge carrier mobility and transparency [6, 8, 11, 12]. These distinctive properties make graphene an ideal candidate for the application of transparent conducting electrodes like other carbon-based materials [13-15]. The structural and electrical properties of graphene are extremely affected and modified via chemical doping, metal doping, and high energy electron or ion irradiation [16-19]. The controlled tunability is an essential to make the graphene devices more suitable for technological applicability. Chemical doping is one of the most common approaches for the modification of structural and electrical properties; however, it produces structural disorders [20-24]. The high energy electron or ion irradiations therefore mostly induce the large structural defects in graphene [18, 25-30]. The exchange of carbon atoms in the graphene lattice with dopant atoms may provide another route, but this substitute doping may have some disadvantages that cause the disorder in the honeycomb structure and potentially reduce the carrier mobility of the graphene [18, 31, 32]. The application of oxygen plasma treatment is able to tailor the electrical properties of graphene through oxidation, but the induced structural disorders are irrepressible [33, 34]. However, these complications can be avoided by employing an alternative approach for the tunability while preserving the honeycomb structure of graphene. Theoretical

predictions suggest that the modification of graphene with photo oxidation is a conceivable approach for tuning the properties of graphene [35-37]. Some experimental studies have been carried out to investigate molecular photo-assisted desorption and absorption, particularly with the ultraviolet light effect on pristine and functionalized graphene layers [38-40]. However, a comprehensive methodology is still required for the tunability of graphene from neutral to doped states for flourishing applications. In this work, we concentrate on the defect-free modulation of graphene. Recently, graphene-based research shows great interest in the investigation into the modification of electrical properties as a function of the number of graphene layers. The electronic structure and morphology become different by increasing the number of graphene layers [41]. For example, the electronic structure of single-layer graphene (SLG) is distinct from bilayer graphene (BLG) and trilayer graphene (TLG). The study of different graphene layers is more important, because the optical, structural and electrical properties obviously change when we go from a linear spectrum (single-layer graphene) to the parabolic spectrum that is present in bi- or trilayer graphene. The stacking of more graphene layers reduces the sheet resistance, which makes graphene a more suitable candidate for conducting electronic devices [42-44]. On the other hand, the transparency of graphene layers decreases linearly in proportion to the number of layers, in the order of 2.3% for each layer in the visible region. However, more than 90 % transparency may still be achieved with up to three layers of graphene [11].

Here we report the tuning of electronic properties of mechanically exfoliated single-, bi-, and trilayer graphenes by DUV irradiation without significantly degrading its charge carrier mobility. Raman spectroscopy and charge transport measurements reveal that the DUV irradiation effect tunes the properties of single-, bi-, and trilayer graphene layers towards p-type doping. The shift of Dirac point positions for single-, bi-, and trilayer graphenes is investigated as a function of DUV irradiation time. It is found that the charge neutrality point shifts toward positive gate voltage with increase of DUV irradiation time for single-, bi-, and trilayer graphenes, which evidently confirms the p-doping effect. The results indicate that DUV irradiation is a non-destructive approach to tuning the properties of single-, bi-, and trilayer graphenes, while preserving the optical, structural and electrical assets.

3.2 Device fabrication and characterization

3.2.1 Preparation of graphenes

The SLG, BLG, and TLG films are obtained by mechanical exfoliation of natural graphite flakes by using adhesive tape, and then transferred onto a 300 nm SiO_2 supported with Si wafer. The layer numbers of the graphene films are identified by optical microscope and Raman spectroscopy, as shown in Fig. 3.1 (a), (b) and (c). The big patterned electrodes (Cr/Au of 5/30 nm) for all SLG, BLG, and TLG are made by

photolithography on Si/SiO2 substrate. The electrodes are made by e-beam lithography and evaporation of Cr/Au (6/50 nm) for electrical transport measurements. The device structures of SLG, TLG, and BLG are shown in Fig. 3.1(a), (b) and (c), respectively.

3.2.2 DUV doping and characterization

The modification of graphene properties by DUV is investigated by transport measurements and Raman spectroscopy. The gate voltage-dependent resistivity measurements and Raman spectroscopy are implemented on pristine graphene, and after different durations of DUV treatment on SLG, BLG, and TLG devices. Raman spectra are performed with a Renishaw micro spectrometer with the laser wavelength of 514.5 nm over wave number from 1100 to 3200 cm^{-1}. The laser power is kept at ~1.0 mW to prevent the introduction of defects and local heating due to the laser. The SLG, BLG, and TLG are exposed with DUV light for a certain period of time, and four terminal Dirac point measurements are taken using a standard lock-in amplifier technique at room temperature in a vacuum.

3.3 Results and discussion

The optical microscope images of the SLG, BLG and TLG field effect transistor devices fabricated on SiO_2/Si substrates are shown after photolithography and e-beam lithography in Fig. 3.1(a-f), respectively. Initially, these numbers of graphene layers were identified on the basis of their optical contrast and then further confirmed by Raman spectroscopy [45, 46]. Figure 3.1(g) shows the Raman spectra of pristine SLG, BLG, and TLG. The ratio of I_{2D}/I_G peaks are found to be 5.1, 1.34 and 0.96 for pristine SLG, BLG and TLG, respectively. The characteristic G and 2D peaks for pristine SLG appear around 1583.8 and 2680.2 cm^{-1}, for pristine BLG observed at 1584.75 and 2699.85 cm^{-1}, while for pristine TLG they appear around 1581.57 and 2703.18 cm^{-1}, respectively. A broad 2D peak is fitted with four Lorentz curves, as shown in Fig. 3.1(h), which confirms the bilayer graphene. Figure 3.1(i) shows the six Lorentz curve fitting of a broad 2D band of TLG. The absence of the D peak in pristine SLG, BLG, and TLG is an indication of defect-free high quality graphenes.

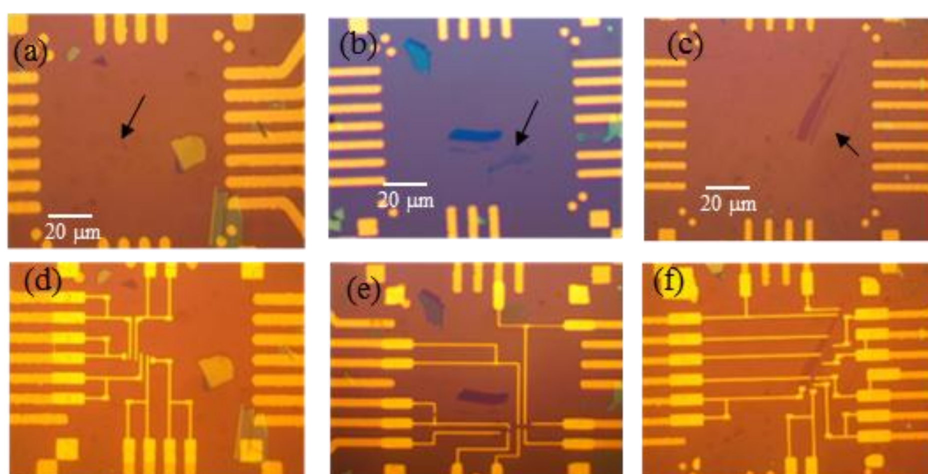

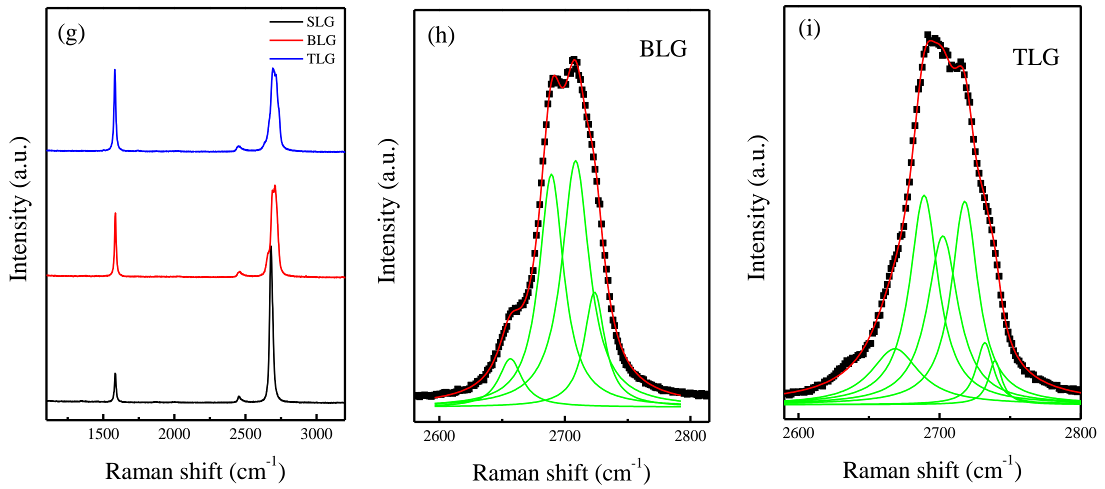

Figure 3.1. (a, b, c) Optical microscopy images of single-, bi-, and trilayer exfoliated graphene devices after photolithography. (d, e, f) Optical microscopy images after e-beam lithography. (g) Raman spectra of pristine single-, bi-, and trilayer graphene. (h) Lorenz curve fitting of the 2D peak for bilayer and (i) fitting for trilayer graphene.

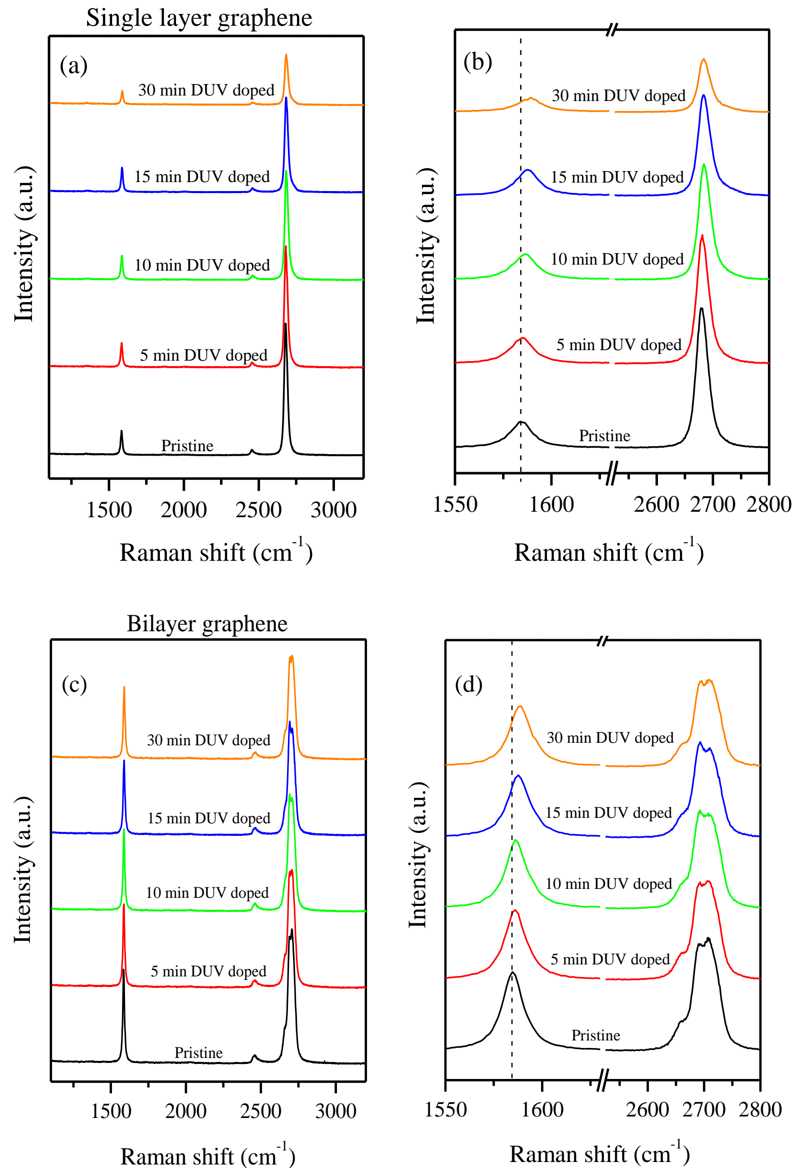

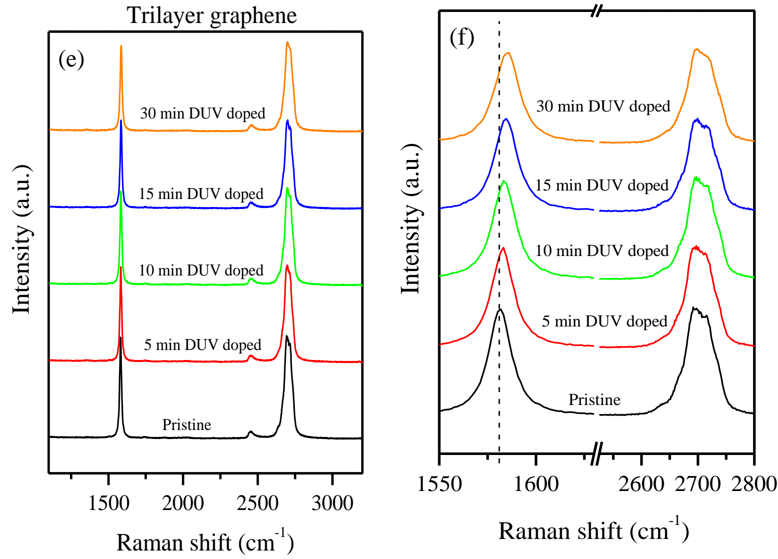

Figure 3.2. Raman spectra of (a,c,d) pristine and DUV irradiated single, bi- and trilayer graphene for (t= 5, 10, 15, and 30 min), (b,d,f) Raman G and 2D spectra of pristine and DUV modified SLG for clarity.

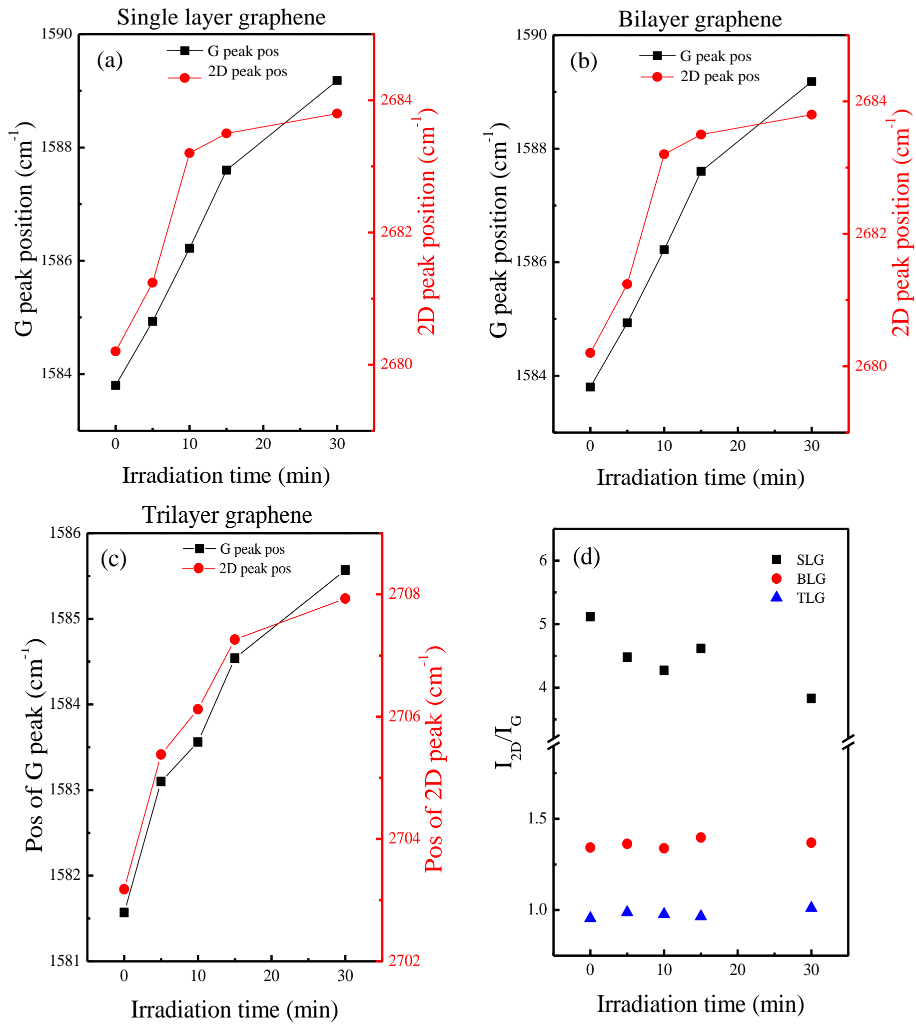

Figure 3.3. (a-c) Shift of G and 2D peak positions of SLG, BLG, and TLG for period of DUV irradiation time. (b) The ratio of peak intensities ratio of G and 2D for SLG, BLG, and TLG are plotted as a function of DUV irradiation time.

Figure 3.2 (a) shows the Raman spectra of SLG before and after different periods of DUV irradiation time (5, 10, 15, and 30 min). The D peak is not observed on increasing irradiation time, which indicates that DUV irradiation does not change the lattice structure of graphene. The upward shifting of G and 2D peak positions are responsible for p-doping, as shown in Fig. 3.2(b). It has already been reported that the shifting of G and 2D peak positions toward lower wavenumber and upper wavenumber is attributed to n-type and p-type doping, respectively [25, 26, 47-49]. Raman spectra of BLG for pristine graphene and after different periods of irradiation time are shown in Fig. 3.2c. The intensity of the D peak undergoes no increase in BLG after modification with DUV irradiation for different time durations, as shown in Fig. 3.2(c). The upward shifting of G and 2D peak positions are shown in Fig. 2(d) for clarity. The shifting of the G peak position toward higher wavenumber is attributed to p-doping of bilayer graphene. Figure 3.2(e) shows the Raman spectra of TLG for pristine graphene and after different periods of irradiation time. The upward shifting of G and 2D peak positions are shown in Fig. 5.2(f) for clarity. The shifting of G peak positions toward higher wave number is also attributed to p-doping for trilayer graphene. The shift of G and 2D peak positions of SLG, BLG, and TLG before and after DUV irradiation are shown in Fig. 3.3(a), (b), and (c), respectively. For all SLG, BLG, TLG, the G and 2D peak positions are shifted to higher wave number, which is attributed to p-doping. The general trend of the shifting of peak positions is similar for a different number of graphene layers. Figure 3.3(d) shows the intensity ratio of 2D and G peaks (I_{2D}/I_G) before and after DUV irradiation for different periods for SLG, BLG, and TLG. The I_{2D}/I_G of SLG shows a slight decrease when increase irradiation time is increased, while in BLG and TLG it remains significantly unchanged with an increase irradiation time. This decrease in the I_{2D}/I_G ratio may be due to the increase in the carrier density of graphene, as previously reported [50].

The p-doping effect of exfoliated SLG, BLG, and TLG is further confirmed by Dirac point measurements. Resistivity as a function of gate voltage (Vg) before and after DUV irradiation treatment of SLG, BLG, and TLG is shown in Fig. 3.4.

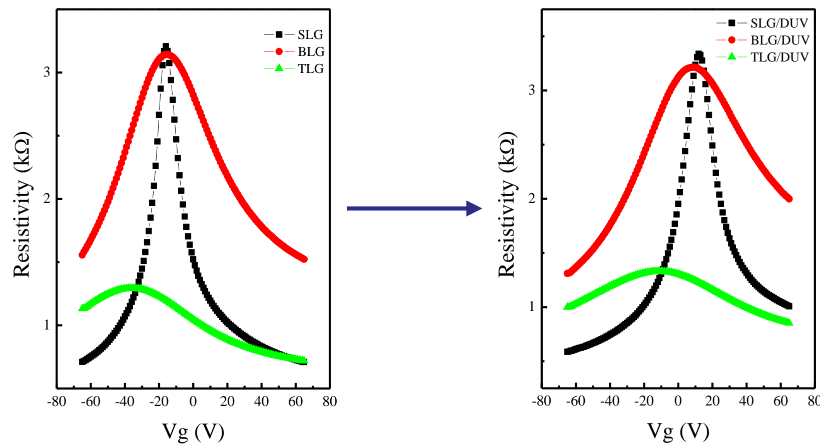

Figure 3.4. The general trend of the transformation of the Dirac point position for SLG, BLG, and TLG, before (left side) and after (right side) DUV irradiation for 30 minutes.

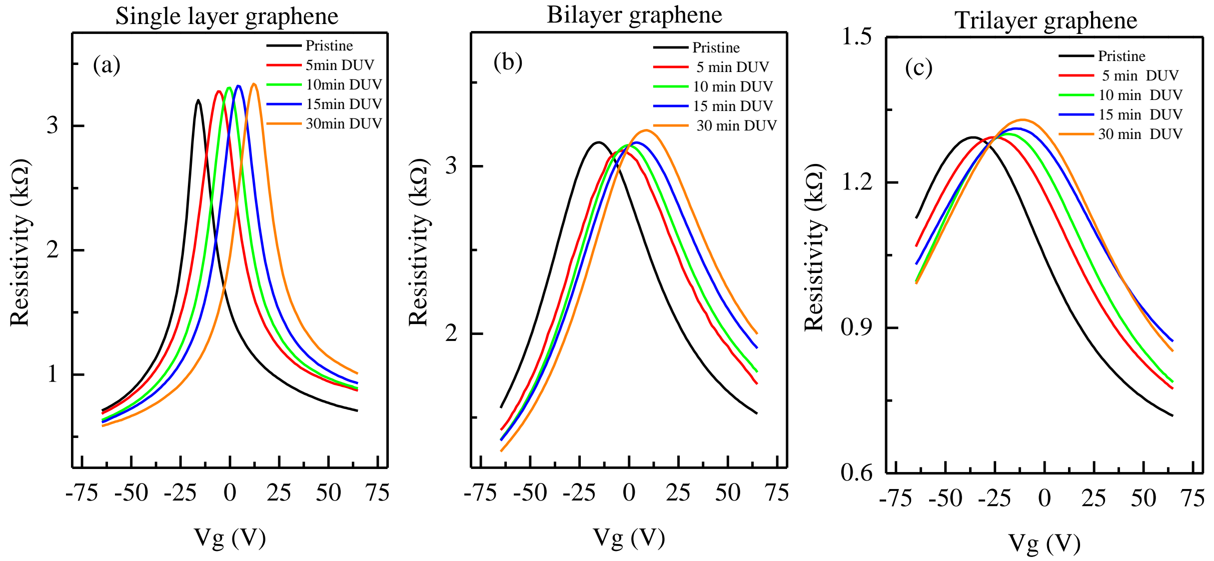

Figure 3.5. Resistivity as a function of back gate voltage (Vg) for the (a) SLG pristine and after different periods of DUV irradiation time. (b) BLG pristine and after different periods of DUV irradiation time. (c) TLG pristine and after different periods of DUV irradiation time.

Resistivity as a function of gate voltage (V_g) before and after DUV irradiation treatment of SLG, BLG, and TLG are shown in Fig. 3.5. Figure 3.5(a) shows the Dirac point (V_{Dirac}) of SLG for different periods of time. After taking the measurements of pristine graphene, the device is then exposed to DUV light for the desired amount of time and afterwards the electrical transport measurements are taken after subsequent steps. The V_{Dirac} of the pristine SLG is found around V_g = -16 V and the V_{Dirac} shifts towards positive V_g on increasing DUV exposure time and is reached at V_g= 12 V after 30 minutes, which is indicative of p-type doping in exfoliated SLG. Figure 3.5(b) and (c) show the V_{Dirac} of BLG and TLG for different periods of time. The V_{Dirac} of the pristine BLG is found around V_g= -15 V and V_g= -36 V for TLG. The V_{Dirac} shifts towards positive V_g on increasing DUV exposure time and is reached at V_g= 8 V and -11V, respectively, after 30 minutes, which indicates p-type doping in exfoliated BLG and TLG.

The gradual shifts of Dirac point positions with irradiation time for SLG, BLG and TLG are shown in Fig. 3.6(a), while Fig. 3.6(b) shows the change charge carrier density (Δn) as a function of irradiation time. The charge carrier density is obtained from the relation $\Delta n= C_g | V_{Di} - V_{Dp} | /e$, where C_g is the gate capacitance, 115 aF/μm^2, obtained for our SiO_2/Si substrate; V_{Dp} represents the Dirac point of SLG, BLG, and TLG, and V_{Di} is the Dirac point after different periods of DUV irradiation time [51]. The Δn increases with the increasing the period of DUV exposure time. These modifications in charge carrier density are related to the tunability of the Fermi level of graphene layers. Thus, DUV irradiation significantly modulates the Fermi level of graphene. Similar trends in charge carrier densities are observed for BLG and TLG as a function of irradiation time, as shown in Fig. 3.6(b).

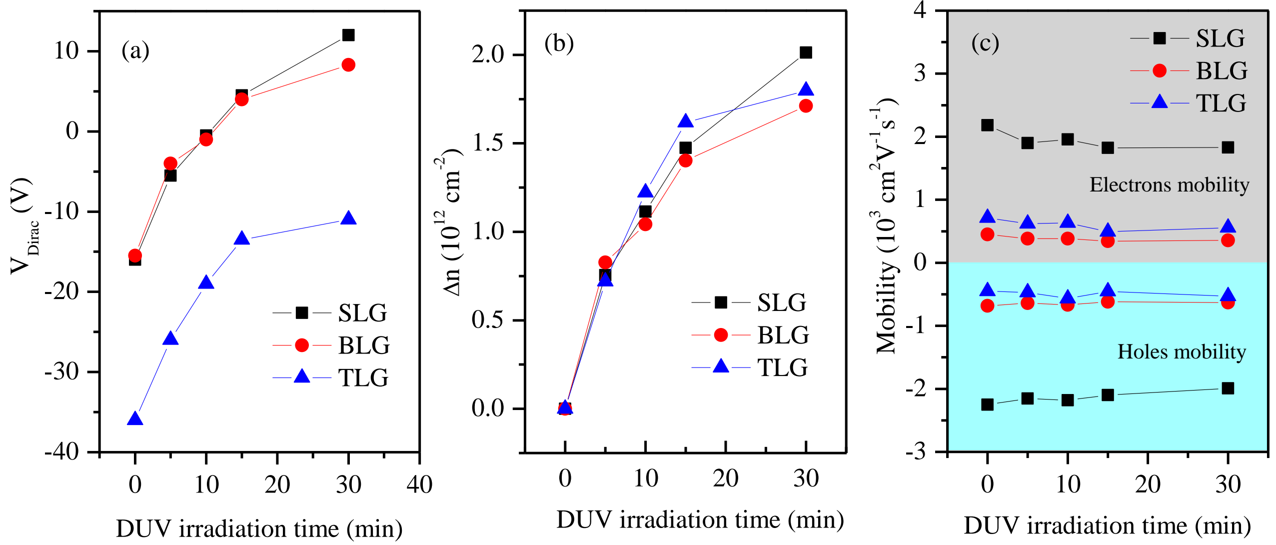

Figure 3.6. (a) The shift of Dirac point positions with different periods of irradiation tine for SLG, BLG, and TLG. (b) Change of charge carrier density (Δn) as a function of irradiation time for SLG, BLG, and TLG. (c) The electrons and holes mobilities as a function of irradiation time for SLG, BLG, and TLG.

The mobility (μ) of different graphene layers are obtained by taking the slope of the conductivity of Dirac points before and after irradiation for different periods of time, and are calculated using the relation $\mu=(1/C_g)(\delta\sigma/\delta V_g)$, where σ (1/Resistivity) is the conductivity of graphene layers and V_g is the back gate voltage. Figure 5c shows the mobility of pristine and DUV doped single, bi- and trilayer graphenes. The mobilities are found to be sustainable for all graphene layers after different periods of irradiation time. These results are in line with the previously reported transport measurements of DUV irradiation on chemical vapor deposition grown single layer graphene [49].

The holes formation in graphene is the result of photo-oxidation of oxygen molecules under DUV irradiation. Theoretical investigations have determined that oxygen molecules dissociate in the presence of UV light [52]. These dissociated molecules lead to the generation of oxygen-containing groups which can easily attach themselves to the most stable sites of graphene and provide favorable conditions for p-doping of graphene [52-54]. During the photo-oxidation process with DUV light, the O_2 molecules absorb 185 nm photons to form two $O(^3P)$ atoms in the ground state, as this energy is sufficient to break the molecular bond: $O_2 + h\upsilon = 2O(^3P)$; and these dissociated O(3P) atoms attach themselves to the most stable adsorption sites of the graphene [55]. The photon energy ($E=h(c/\lambda)$) of DUV light is inversely proportional to the wavelength, and this energy is reduced for higher wavelengths. Therefore, the shift of the Dirac point position may have less effect at a lower energy (i.e. increased wavelength), because the dissociation of oxygen molecules to form oxygen atoms will be smaller, while the effect will be more prominent at higher energy (i.e. decreased wavelength) due to the large amount dissociation of oxygen molecules. The intensity of DUV light determines the concentration of carriers in the graphene, while for higher intensities the carrier concentration effectively increases, which greatly enhances the doping level.

3.4 Conclusion

We have investigated the tunability of mechanically exfoliated single-, bi-, and trilayer graphene layers using DUV irradiation for different periods of time. The Raman spectroscopy and transport measurements reveal the p-doping effect under DUV irradiation for all single-, bi-, and trilayer graphene layers. The shift of G and 2D peak positions and intensity ratios for single-, bi-, and tri-layer graphene layers are evaluated as a function of irradiation time. The shift in the G and 2D bands in the Raman spectra towards higher wavenumber suggests p-doping in the graphene devices. The absence of the D peak in Raman spectra after irradiation reveals the defect-free modulation of graphene layers. The Dirac point is shifted towards positive gate voltage for single-, bi-, and trilayer graphenes on increasing DUV irradiation time, which is attributed to the strong p-doping effect. Thus, DUV irradiation doping significantly modulates the Fermi level of graphene layers while sustaining its mobility. The results indicate that DUV irradiation can significantly tailor the properties of graphene layers without degrading structural and electrical holding. Doping using DUV irradiation is a suitable photo-assisted scheme for modulating the electronic properties of graphene layers for future graphene-based transparent electronic devices.

Chapter 4

4 Formation of p-n junction with stable p-doping in graphene field effect transistors using deep UV irradiation

We demonstrate the modification of the electronic properties of single layer chemical vapor deposition (CVD) grown graphene by deep ultraviolet (DUV) light irradiation. The shift in G and 2D bands in Raman spectroscopy towards higher wave numbers suggests p-doping in graphene field effect transistors (FETs). In the transport measurement, the Dirac point is shifted towards positive gate voltage on increasing the DUV light exposure time, revealing the strong p-doping effect without any significant increase in resistance. The doping is found to be stable in graphene devices with a slight change in mobilities. We have also constructed the p-n junction with DUV light exposure on a selective region of graphene and investigated by gate voltage the dependent resistivity measurement and current-voltage characteristics.

4.1 Introduction

In recent times, graphene, a two-dimensional sp^2-hybridized network of carbon atoms with one atom thickness, has been recognized as an important material for electronic devices due to its unique electronic properties such as ambipolar transport [10, 12]. Single layer graphene films can be obtained by different methods such as mechanical exfoliation of graphite [6]. However, it is very difficult to control the number of layers and to achieve large-scale production by using mechanical exfoliation. The epitaxial growth of graphene on SiC substrate is another way to do this, but it requires very high-temperatures and is also expensive [56], However, chemical vapor deposition (CVD) on metal (Cu, Ni) substrate is the most feasible and promising approach for large-scale production of graphene [57]. Tuning of the Fermi level of graphene is an important factor for electronic applications [58]. A number of approaches have recently been applied to tuning the electronic properties of graphene, for example, electron, ion beam irradiation, with metal deposition, absorption of gas molecules, chemical and electrochemical doping [19, 25, 35, 59, 60]. The electrical transport properties of graphene are very sensitive to local perturbations or defects induced by adsorption or desorption of gas molecules, as well as surface charge doping from various aromatic molecules, which often degrades the carrier mobility of graphene [20, 35-37, 59, 61]. It is highly desirable to develop an alternative way to tune the doping level without reducing the mobility of graphene. One plausible technique is to modulate the Fermi level of graphene by surface modification. M. Grujicic et al. have reported the computational calculations for the interactions of an oxygen molecule with single-walled carbon nanotubes and their oxidation under UV light [62]. There are three major approaches for oxidizing graphene. Oxygen plasma treatment and electron beam irradiation are two well-known methods to oxidize

graphene, but treatments of the above-mentioned methods create defects in graphene [25, 33, 34, 63, 64]. The third most suitable technique is the oxidation of graphene without defects as generated by UV light in atmosphere [39, 65, 66]. However, only a few experimental studies have been done so far to investigate the molecular photo-assisted desorption and absorption, particularly with the UV light effect on pristine or functionalized CVD grown graphene layer [38, 39, 67, 68]. P. Joo et al. have recently reported the optical switching of spiropyran functionalized graphene multilayer FETs by UV light. S. Huh et al. have studied the UV/Ozone-Oxidized of graphene using Raman dye molecules such as rhodamine B (RhB), rhodamine 6G (R6G), and crystal violet [39]. M. Kim et al. have reported the modulation of doping in functionalized graphene by pyrene tethered disperse red (DR1P) [38]. Theoretically, it has been observed that oxygen molecules react with graphene in the presence of UV light to produce oxygen containing groups (such as the dissociation of an oxygen molecule into oxygen atoms) [55]. These oxygen atoms form a stable structure on the sites of pristine graphene and induce p-type doping [52, 69].

We have investigated the doping in CVD grown graphene film with deep ultraviolet (DUV) light. Raman spectroscopy and transport measurements reveal that DUV light produces p-doping for CVD grown graphene. The shift of G and 2D peak frequencies and the intensity ratios of these peaks are analyzed as a function of DUV light exposure time. The back gate voltage dependent resistivity for single-layer graphene is also analyzed as function of DUV light exposure time. The maximum resistivity corresponding to the Dirac point is shifted toward positive gate voltage when increasing the DUV light exposure time. We have constructed the p-n junction in the single-layer CVD grown graphene by exposing half of the graphene with DUV light, while remaining halft is covered with metal mask. The results indicate that modification by DUV light is an appropriate approach to tailor the electrical properties of graphene without introducing unusual defects in graphene.

4.2 Experimental

Large-area high-quality monolayer graphene samples are synthesized on 25 μm thick Cu foils (Alfa Aesar, 99.8 %, #13382) by remote radio frequency (RF) plasma-enhanced chemical vapor deposition (RF-PECVD) system. The CVD chamber is pumped with pressure up to ~10^{-7} Torr with a turbo-molecular-pump. Polycrystalline Cu foil is accumulated in the chamber. Before starting gas flow into the chamber, the Cu substrate is heated up to 830 °C. H_2 gas is then introduced into the chamber at a flow rate of 40 standard cubic centimeter per minute (sccm). The hydrogen gas is then discharged by RF power of 50 W for two minutes to purge the surface oxides of copper foil. During the growth of graphene, the RF plasma is generated for 3 minutes with a continuous flow of a mixture of argon (40 sccm) and methane (1 sccm) gas at a pressure of 10 mTorr. Subsequently the sample is cooled down to room temperature. The grown graphene film on Cu foil is transferred to the Si substrate with the wet transfer method. The Cu foil is spin-

coated (850 rpm for 10sec, 2500 rpm for 60sec) with a thin layer of polymethyl methacrylate (PMMA). The lower Cu foil is then removed by etching in a 1 molar solution of ammonium persulfate (APS) ($(NH_4)_2S_2O_8$), and the PMMA membrane is washed with de-ionized water. The graphene film with the PMMA membrane is then transferred to heavily p-doped Si substrate with 300 nm thick SiO_2 top layer, and the graphene on the Si/SiO_2 substrate is kept in acetone for one day in order to dissolve the PMMA layer [57]. The diagram of the DUV irradiated graphene device is shown in Fig. 4.1. The DUV light (λ= 220 nm, average intensity of 11 mW/cm^2) is applied for the doping of the graphene. Raman spectra are measured with a Renishaw micro-spectrometer over a wave number from 1100 to 3200 cm^{-1} with the laser wavelength of 514.5 nm. The spot size is ~1 μm, and power is kept at ~1.0 mW to avoid local heating. The Cr/Au (5/30nm) contacts are made by using a metal mask and a thermal evaporation system. The electrical measurements are performed using the standard lock-in technique with an ac current of 50 μA at 11.7 Hz.

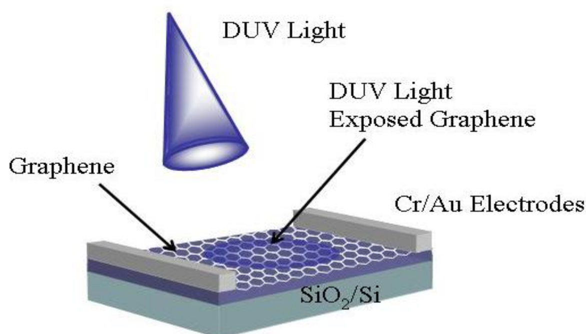

Figure 4.1. Diagram of DUV light exposed CVD grown single-layer graphene FET structure.

4.3 Results and discussion

Raman spectroscopy has been used as a standard nondestructive tool for the electronic structure characterization of carbon based crystalline films. It has also been used to measure the number of graphene layers and to analyze disorder, strain and doping in graphene. We have utilized Raman spectroscopy to detect the doping effect in graphene resulting from the DUV exposure. Fig. 4.2(a) shows the Raman spectra of single layer CVD grown graphene before and after modification with DUV light for different exposure times, and also shows the characteristic peaks of single-layer graphene. The very small peak around 1345 cm^{-1} in pristine CVD grown graphene is attributed to D or the defect peak for graphene. The D peak is attributed to A_{1g} symmetry phonons near the K-zone boundary. These phonons are not Raman-active due to the momentum conservation in the scattering, and require a defect for their activation. Therefore, the intensity of D peak is indicative of defects in graphene. The very small intensity of D peak indicates the good quality of our graphene samples. However the intensity of the D peak is not significantly changed with time. The characteristic G and 2D peaks appears around 1583 cm^{-1} and 2682 cm^{-1} respectively, for

pristine single layer CVD grown graphene, as similarly reported by others [39]. The G peak corresponds to the E_{2g} optical phonon at the Brillouin zone center and the 2D peak is the second order of the D peak. It originates from a process where momentum conservation is satisfied by two phonons with opposite wave vectors. The full width at half maximum (FWHM) of the 2D band is about 30 $cm^{-1,}$ and the ratio of 2D/G peak intensity is ~ 2.3 for the pristine graphene in Fig. 4.2(a), indicating a single layer of graphene. The shift of G and 2D peaks are clearly observed in Fig. 4.2(b), the G peak transforms from 1583 to 1588 $cm^{-1}$and the 2D peak moves from 2682 to 2690 cm^{-1}. This blue shift of both G and 2D peak positions is attributed to p-doping of graphene. It has already been reported that red and blue shifting of the G and 2D peak positions are attributed to n-type and p-type doping, respectively, in single-layer graphene [43, 47, 70]. This blue shift of the G and 2D peak positions increases with an increase in the exposure time [10, 67]. Fig. 4.2(c) shows the intensity ratio of the D and G peaks (I_D/I_G) as a function of exposure time. The minor change in the ratio of the D/G peak intensity implies a negligible change in sp^2 hybridization before and after DUV light exposure. These defects appearing along the catalyst boundaries are usually generated during growth in CVD graphene. The small ratio ~0.38 of the D/G peak intensity from the Raman spectra of single-layer graphene indicates the relatively low defect density. It also indicates that the intensity of the D peak of CVD grown graphene is slightly enhanced after first exposure to DUV light, and then it does not significantly change with an increase in the exposure time. The slight increase in I_D/I_G may be due to the increasing oxygen bonding with carbon atoms during DUV exposure. The intensity ratio of the 2D and G peaks (I_{2D}/I_G) is found to decrease from 2.3 to 1.08 with an increase in exposure time. This decrease in the ratio of I_{2D}/I_G may be due to an increase in the carrier density of graphene, as previously reported.[50] Although the shift of the Raman band position indicated doping of graphene, the shift can be also induced by other factors such as compressive strain. The concise confirmation of doping can be obtained by electrical transport measurements. The p-doping of CVD grown graphene is confirmed by gate voltage dependent resistivity measurements. Fig. 4.3(a) shows the resistivity as a function of back gate voltage (V_g) before and after DUV exposure for different periods of time. The Dirac point (V_{Dirac}) of the pristine CVD grown graphene is found around zero volts. The graphene devices are then exposed to DUV light for a desired time, and the electrical transport measurements are performed under ambient atmosphere. The V_{Dirac} move towards positive V_g with increasing DUV exposure time indicates p-type doping. It is initially near ~0V for pristine graphene and then shifts rapidly towards positive gate voltage up to ~35 V after 100 minutes of DUV exposure. The formation of holes (p-type doping) is the result of the photo-oxidation of the graphene layer with DUV light exposure [71].

The p-doping of CVD grown graphene is confirmed by gate voltage-dependent resistivity measurements. Fig. 4.3(a) shows the resistivity as a function of back gate voltage (V_g) before and after DUV exposure for different periods of time. The Dirac point (V_{Dirac}) of the pristine CVD grown graphene is found around zero volts. The graphene devices are then exposed to DUV light for a desired time, and the electrical transport

measurements are performed under ambient atmosphere. The V_{Dirac} move towards positive V_g with increasing DUV exposure time indicates p-type doping. It is initially near ~0V for pristine graphene and then shifts rapidly towards positive gate voltage up to ~35 V after 100 minutes of DUV exposure. The formation of holes (p-type doping) as the result of the photo-oxidation of the graphene layer with DUV light exposure [71].

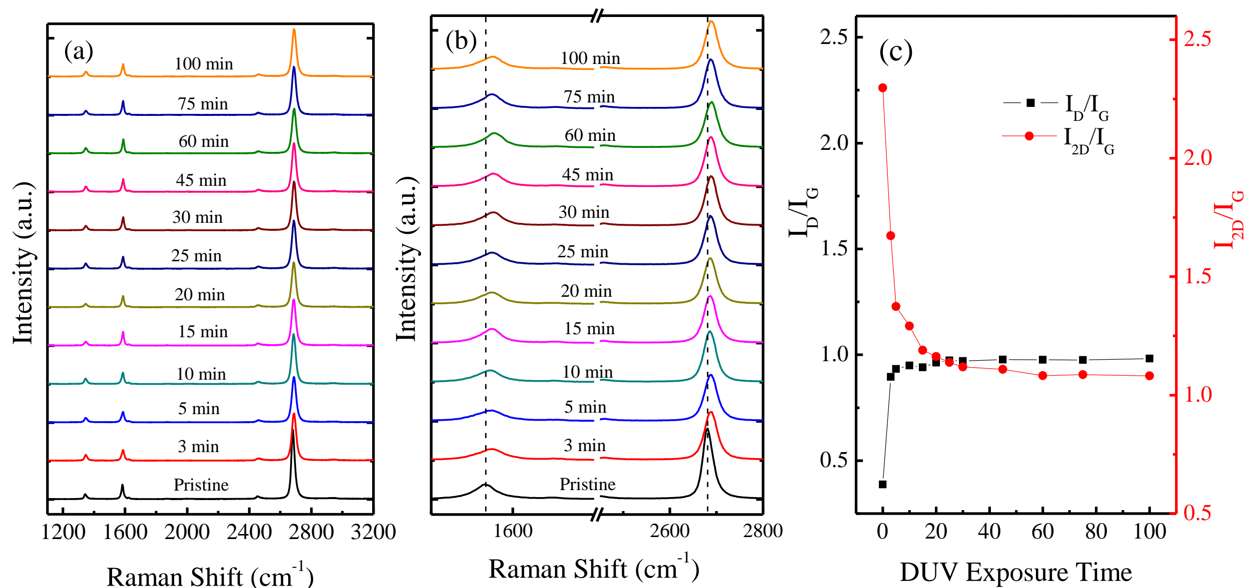

Figure 4.2. (a) Raman spectra of pristine CVD grown graphene and DUV light modified CVD grown graphene (b) Raman G and 2D spectra of pristine and DUV exposed graphene (c) The ratio of the intensities for the 2D and G peaks and the ratio of the intensities for the D and G peaks are plotted as a DUV exposure time.

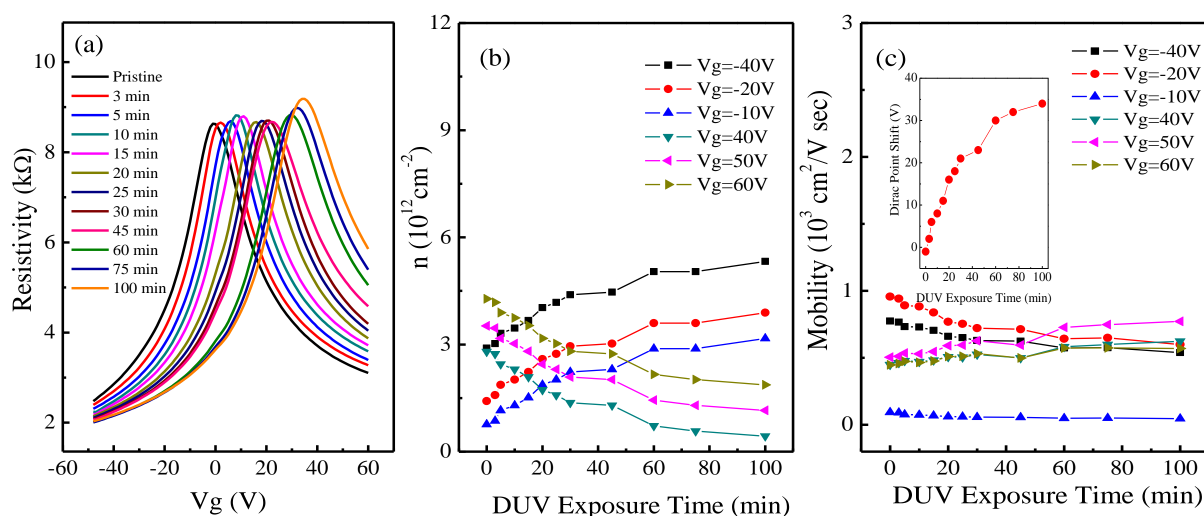

Figure 4.3. (a) Resistivity as a function of back gate voltage (Vg) for the single layer CVD grown graphene before and after DUV light for different exposure time (b) Charge carrier concentration as a function of DUV light exposure time at different gate voltage (c) Mobility as a function of DUV light exposure time at different gate voltage; Inset shows the Dirac points shift as function of DUV light exposure time.

Theoretically, it has been predicted that oxygen molecules dissociate in the presence of UV light. These dissociated molecules react with graphene to create oxygen containing groups and induce p-type doping [53]. These oxygen atoms may also attach themselves to the most stable site of the graphene [52, 54]. In this process, O_2 molecules absorb 185 nm photons to form two $O(^3P)$ in the ground state and this energy is sufficient to break the molecular bond: $O_2+h\upsilon= 2O(^3P)$ and the bridge site are the most stable within the possible adsorption sites of dissociated $O(^3P)$ atoms on graphene [55]. The energy of DUV light is inversely dependent on the wavelength, because $E=h(c/\lambda)$, and for higher wavelengths the energy decreases. Therefore, below the minimum limit of energy (i.e. increase in wavelength), the oxygen molecules cannot dissociate to oxygen atoms and the Dirac point position shift will be lower for higher wavelengths. The intensity of DUV light determines the amount of carrier concentration in the graphene, but after a certain limit of time it saturates, because only a finite number of charge carriers can adsorb on the graphene surface. Noticeably, the graphene does not dope by water molecules [53]. However, the exact physical mechanism for an adequate description of the absorption of water molecules on graphene modified by UV light interaction is not clear at present. Nevetheless, we could expect that water molecules absorb photons from UV light, which causes the water molecule to dissociate into an H-OH bond and then break down to H and H-O bonds. O. Leenaerts et al. have theoretically examined the effect of H and H-O bonds on graphene surface, but small amounts of charge transfer has been observed for different orientations [72].

The shift of V_{Dirac} as a function of DUV light exposure time is shown in the inset in Fig. 4.3 (c). There is no significant change observed in the resistivity at Dirac points of the CVD grown graphene with DUV light exposure. Figure 4.3 (b) shows the charge carrier density as a function of DUV light exposure time at different gate voltages. The charge density is obtained from the relation $ne = C_g(V_g - V_{Dirac})$, where Cg is the gate capacitance ~101 aF/μm^2, which was obtained for our Si/SiO_2 substrate.[51] The mobility of the samples was obtained using relation $\mu = (ne\rho)^{-1}$, where e is the electronic charge, n is the charge carrier density and ρ is the resistivity of the FET device, as shown in Fig. 4.3 (c). It is observed that mobility is not significantly affected by the DUV light exposure.

It is vital for the application of electronic devices that the doping should be stable. This important point is confirmed by measuring the back gate dependent resistivity of same device after two months. It is found that the Dirac point is stable after a couple of weeks, as shown in Fig. 4 (a). After confirmation of stable p-type doping of single layer CVD grown graphene by DUV light, we investigate the exposure of DUV light doping as route for p-n junction formation in CVD grown graphene. Half of the graphene is covered with a metal mask and then the graphene device is exposed to DUV light. The uncovered half of graphene device is affected by DUV light, whereas the other half remains unaffected. The black curve shows the resistance profile of the untreated region of the graphene device and the Dirac point is found to be about +8 V. The

Dirac point is shifted toward a more positive gate voltage (~+36 V) for the DUV exposed region, as shown in the red curve. The blue curve in Fig. 4.4 (b) shows the resistance profile for the combined region of pristine graphene and the DUV light exposed region of graphene. In this case, the gate dependent resistance reveals two distinct Dirac points due to two different regions. The observed two separate gate voltages peaks correspond to the Dirac point at each region of the device. Therefore, a p-n junction can be constructed in the graphene device with the application of an appropriate gate voltage. Since DUV light acts as a p-type dopant for graphene, it raises the Fermi level of the p-doped region; however the untreated region remains at the same Fermi level as pristine graphene. This difference in the Fermi level creates a junction across the boundary. Fig. 4.4 (c) shows the current-voltage (I-V) characteristics of the pristine and DUV exposed exposed graphene region at different back gate voltages. We apply the back gate voltage of V= 0, +20 and +40 V, as in Fig. 4.4 (c). The I-V curves at V= 0 and +40 V correspond to an n-n and an p-p junction, respectively, while the I-V curve at V= +20 V represents the p-n junction. It is well recognized that the I-V curve for a semiconductor junction exhibits the nonlinear behavior due to the depletion region, but in the case of graphene the depletion region is not expected between the doped and undoped regions of graphene due to the gapless band structure. The I-V curves show linear behavior in all regions of graphene and the results are consistent with these explanation.

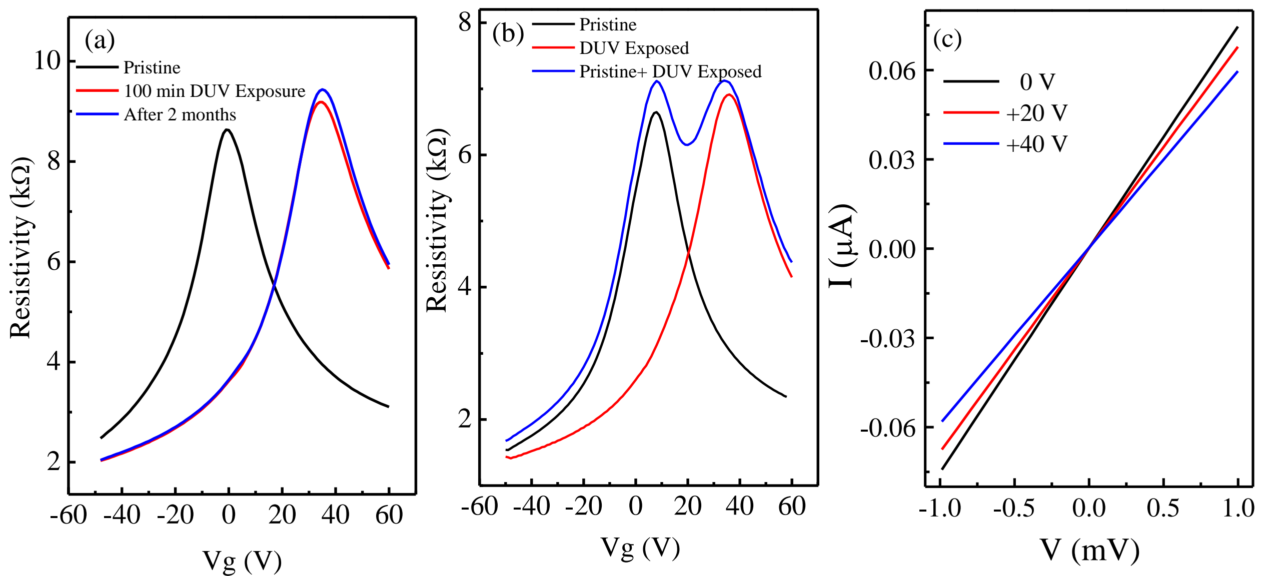

Figure 4.4. (a) Resistivity as a function of gate voltage (Vg) black curve of the pristine single layer CVD grown graphene, red curve of 100 minutes DUV exposed single layer CVD grown graphene and the blue curve shows the doping stability after two months (b) Resistivity as a function of gate voltage (Vg) black curve of the pristine single layer CVD grown graphene, red curve of DUV light exposed and blue curve with two distinct Dirac points shows the combination of pristine+DUV exposed region (c) I-V characteristics at different gate voltages pristine+DUV exposed region.

4.4 Conclusion

We have investigated an effective doping method for large area CVD grown graphene. The scheme adopted in this work has the advantage that doping can be tuned without disturbing the physical configuration of graphene FET devices. The shift in the G and 2D bands in Raman spectroscopy towards a higher wave number suggests the p-doping in graphene FET devices. In back gate voltage-dependent resistivity measurement, the Dirac point is shifted toward a more positive gate voltage when the DUV light exposure time is increased, which indicates a strong p-doping effect without any significant increase in resistance. Doping is found to be stable in graphene devices with a slight change in mobilities. The back gate-dependent resistivity measurements indicate tunable p-doping and p-n junction formation with DUV light, an appropriate approach for modifying the electrical properties. This promising photo-assisted approach holds potential interest for future graphene-based electronic devices and sensors.

Chapter 5

5 Ultraviolet light induced reversible modulation of doping in graphene transistors with efficient photocurrent generation

We show the reversible doping in graphene using deep ultraviolet (DUV) irradiation and flow of dry oxygen and nitrogen. Hole doping is observed by DUV irradiation with oxygen flow, but becomes reversed with nitrogen flow. The generation of efficient photocurrent enables the integration of high-efficiency optoelectronic devices.

5.1 Introduction

Graphene, a two-dimensional sp^2-hybridized network of carbon atoms, has been the object of much attention due to its novel linear dispersion relation, resulting in unique electronic properties [10, 12]. Because of these distinctive properties, graphene is expected to be a prospective material for electronics applications [13, 73]. The extremely sensitive planar structure of graphene readily absorbs the molecules acting as donors or acceptors [20, 74]. A number of theoretical and experimental studies have investigated the irradiation or molecular doping effect on mechanically exfoliated or chemically derived graphene layers [16, 25, 26, 36, 37, 61, 75]. A route for efficient doping in graphene is to replace carbon atoms in the graphene lattice with dopant atoms [18, 31, 32]. However, this type of substitutional doping leads to disorder in honeycomb structure, which in turn gives rise to defects in graphene. These defects due to local perturbations, a non-covalent detaching or latching, can be avoided by employing a alternative approach for electron or hole doping while preserving the honeycomb structure of graphene. Controlling the Dirac point of graphene is a crucial for the application of nanoelectronic and optoelectronic devices. A plausible technique is to modulate the doping level in graphene by surface modification [35], since the graphene surface is very sensitive to adsorption or desorption of gas molecules [20]. However, only a few experimental studies have so far investigated the molecular photo-assisted desorption and absorption, particularly the ultraviolet light effect on the pristine and functionalized vapor deposition (CVD) grown graphene layer [38, 39, 49, 67, 76].

In this work, we demonstrate reversible hole doping in CVD grown graphene films with DUV irradiation in gas flow environment. We characterize the doping effects by using electrical transport, Raman and X-ray photoelectron spectroscopy (XPS) measurements. The reversible doping process is explained by the

formation mechanism of NO molecules and detachment from the graphene surface, and an efficient photocurrent is generated in a DUV, DUV/O_2 and DUV/N_2 environment.

5.2 Experimental

5.2.1 Graphene growth and device fabrication

Large area graphene films are grown on 25 μm thick Cu foils by the same method as that described in Chapter 4. The Cr/Au (6/35nm) contacts with size of 500×500 μm^2 are made by using a metal mask and a thermal evaporation system. The Cr/Au contacts are located in a square shape and the distance between contacts is 3.6 mm. We use van der Pauw method to measure the resistivity of graphene [77], where an ac current of 50 μA at 11.7 Hz is used. The DUV light lamp (λ= 220 nm, average intensity of 11 mW/cm^2) in O_2 or N_2 gas flow is applied for doping of the graphene. Doping treatments in this experiment can be performed without affecting the physical configuration of the graphene devices. The doping effects of graphene are examined by Raman spectroscopy, XPS and electrical transport measurements.

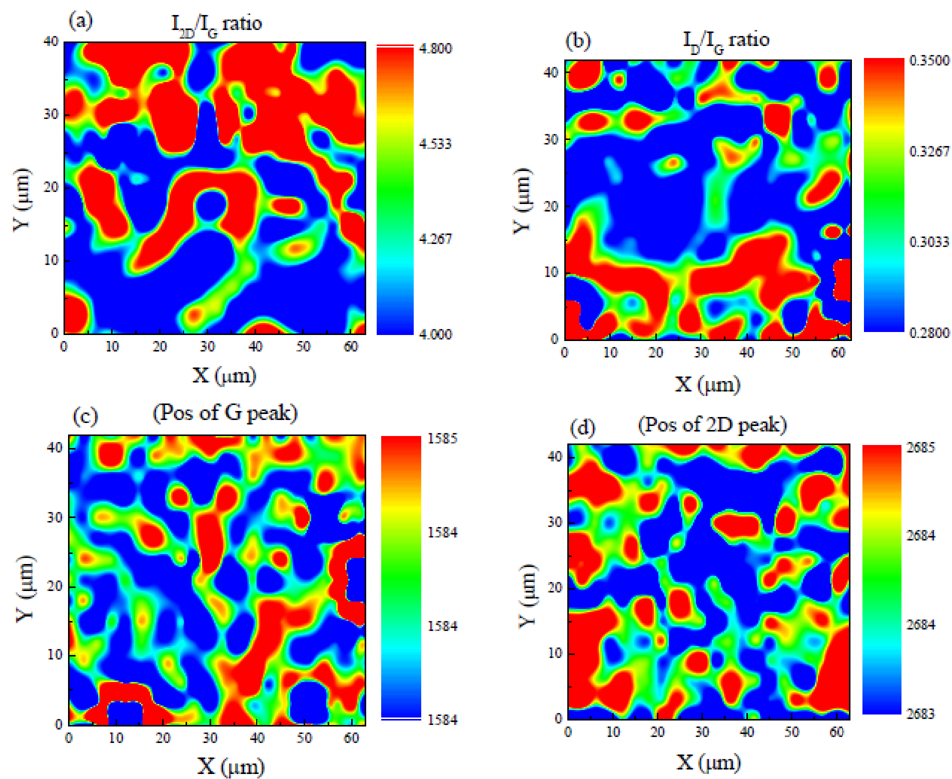

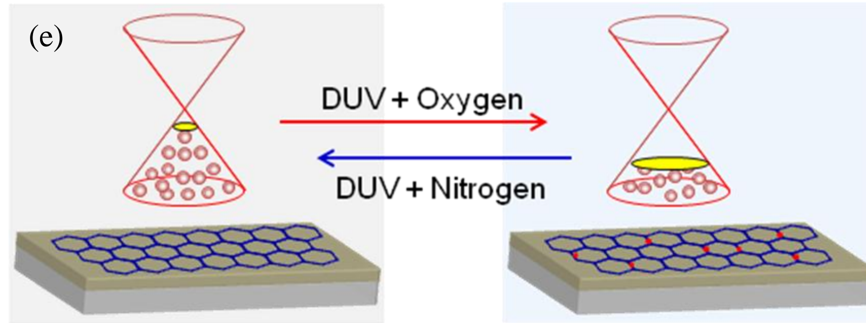

Figure 5.1. (a) Raman mapping of peak intensity ratios of 2D and G and (b) peak intensity ratios of D and G. (c) Mapping of position of the G peak and (d) position of the 2D peak. (e) Diagram of the doping mechanism during DUV irradiation in different gas atmospheres.

5.3 Results and discussion

5.3.1 Evaluation of Raman spectra of DUV irradiated graphene

We employ Raman spectroscopy with 514.5 nm laser excitation to study the intrinsic properties of graphene. The detailed investigation on the quality of CVD grown graphene over the large area is confirmed by Raman mapping and can be seen in Fig. 5.1 (a-d). The 2D/G peak intensity ratio is greater than 4.5 for graphene on the Si/SiO_2 substrate, indicating a single layer of graphene. However, a very low D peak intensity is observed in Raman spectra of graphene, which reveals a relatively high quality with low defect density. These defects or vacancies present along the catalyst boundaries are usually generated during growth in CVD graphene. The diagram for DUV induced doping through adsorption and desorption of gaseous molecules on graphene is shown in Fig. 5.1 (e). Raman spectroscopy is used to trace the general trend of DUV irradiation effects with and without gaseous environment, as shown in Fig. 5.2 (a,b). This shift is found to be more prominent in a DUV/O_2 environment, but becomes less effective with O_2, as shown in Fig. 5.2 (c,d). The shift in peak positions is also well controlled in the DUV/N_2 case rather than on N_2 flow without DUV.

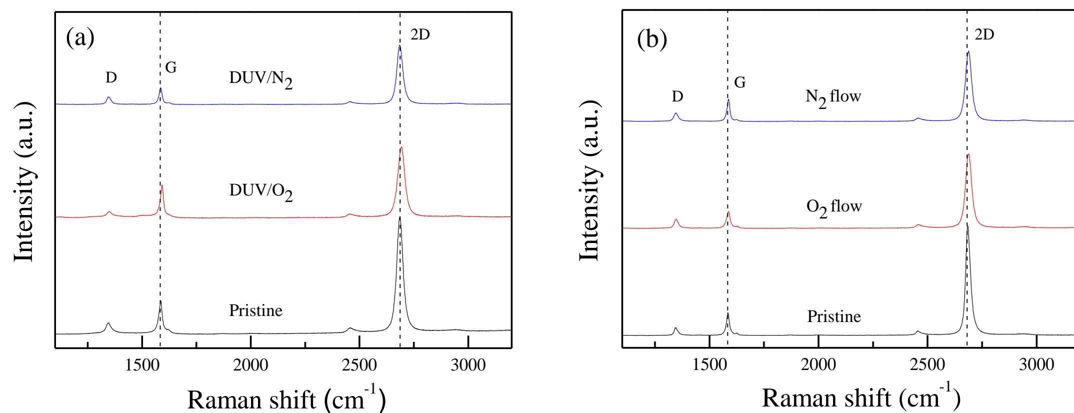

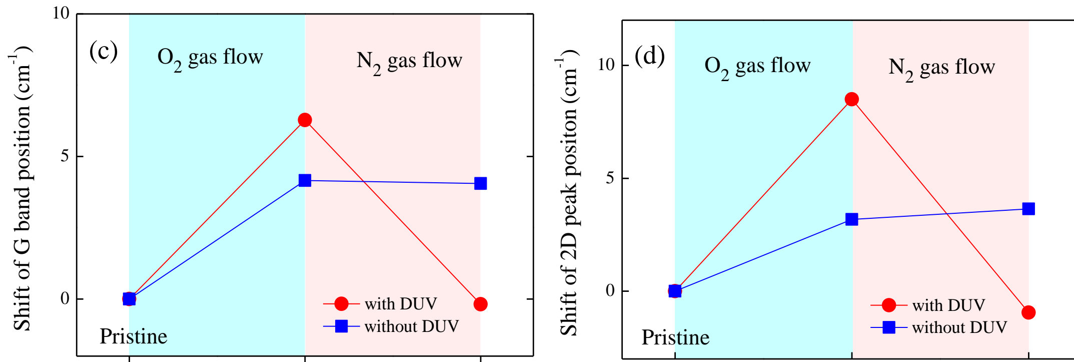

Figure 5.2. (a) Raman spectra of pristine graphene, DUV irradiated graphene in O_2 flow (denoted by DUV/O_2), DUV irradiated graphene in N_2 flow (denoted by DUV/N_2) after DUV/O_2. DUV treatments were done for 60 minutes. (b) Raman spectra of pristine graphene, graphene in O_2 flow for 60 minutes, graphene in N_2 flow for 60 minutes after the O_2 flow treatment. (c) Shift of the Raman band position between treatments with and without DUV irradiation, changes in the G band position for pristine graphene, graphene in O_2 flow, graphene in N_2 flow. (d) The changes in the 2D band position for pristine graphene, graphene in O_2 flow, graphene in N_2 flow.

5.3.2 Transport measurements of DUV irradiated graphene

A detailed study of doping mechanism is carried out by electrical transport measurement. The graphene field effect transistor devices are exposed by DUV irradiation in a gas flow for a desired time, and then the electrical transport measurements are performed in a vacuum at room temperature. The charge neutrality point is identified by resistivity measurement as a function of back gate voltage (V_g). Figure 5.3 (a) shows that the charge neutrality point moves toward positive V_g as DUV light irradiated graphene, indicating p-type doping. The shift of the charge neutrality point increases rapidly with the initial treatment and tends to saturate as the DUV irradiation time increases beyond 60 min. The charge neutrality point is initially near ~5V for pristine graphene, which is slightly p-doped. As the irradiation time increases, the charge neutrality point shifts towards positive gate voltage up to ~54 V after 60 min of DUV irradiation in O_2 gas flow. Initially, the resistivity of the graphene device is increased during DUV irradiation under O_2 gas flow, but remains stable in subsequent DUV treatments.

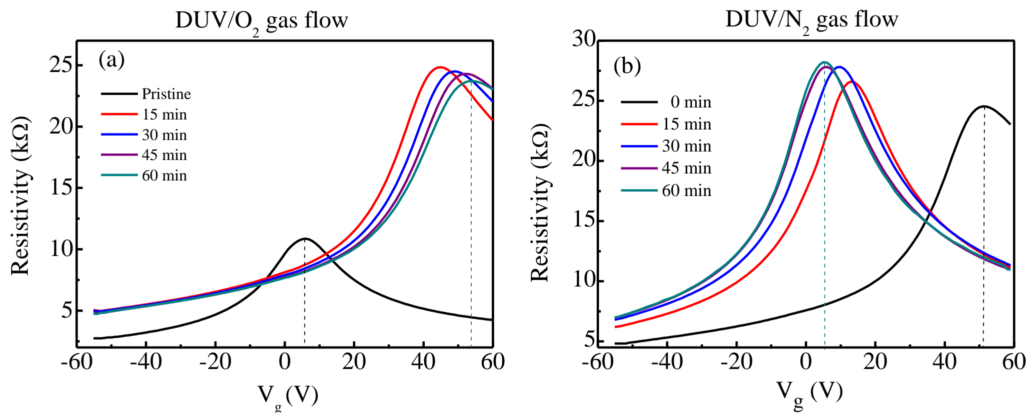

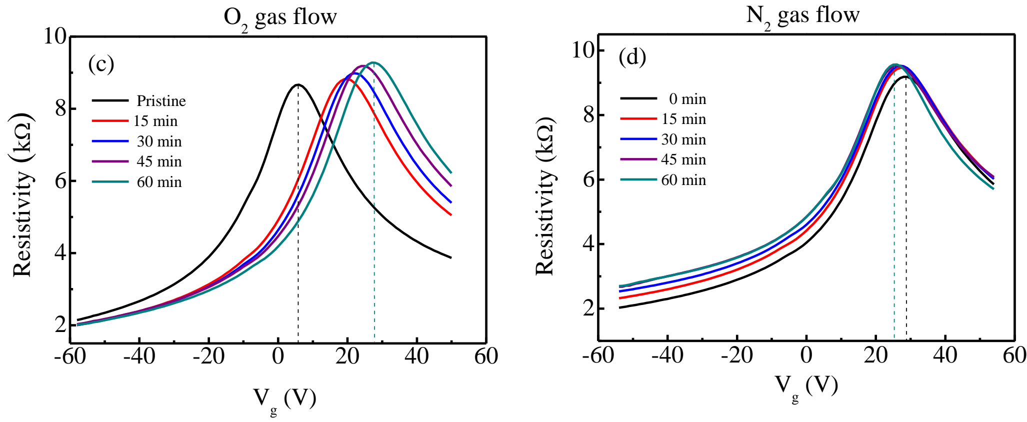

Figure 5.3. Resistivity as a function of back gate voltage (V_g) for (a) DUV irradiated graphene in O_2 flow, (b) DUV irradiated graphene in N_2 flow after DUV/O_2. Resistivity as a function of back gate voltage (V_g) for (c) graphene in O_2 flow, (d) graphene in N_2 flow after the O_2 flow treatment.

This reason for this increase in resistivity remains unclear, but may be due to the interaction of DUV light with residues or dangling bonds on graphene in an O_2 environment. Figure 5.3 (b) shows that the reversal of hole doping is produced by DUV irradiation under an N_2 gas flow. The charge neutrality point shifts from 54 V to 13V after 15 min DUV irradiation under N_2 gas flow, and reaches the initial value of 5V after 60 min DUV irradiation. The resistivity of the graphene field effect transistor devices are found to increase during the irradiation process. The efficiency of DUV irradiation is compared by simple gas flow treatment. Figure 5.3 (c,d) shows the charge neutrality point shift under O_2 and N_2 gas flow without irradiation of DUV light. Hole doping by O_2 gas flow treatment is reported for exfoliated graphene [78]. While dry oxygen binding is reversible by re-exposure to flowing Ar gas, the hole doping by oxygen binding becomes irreversible under wet environments [53]. In Fig. 5.3 (c) a similar hole doping effect is observed in the treatment of dry O_2 gas flow without irradiation of DUV light. However, the hole doping effect is smaller than that with DUV irradiation. The charge neutrality point shifts up to ~28 V after 60 min O_2 gas flow. In subsequent treatment, as shown in Fig. 5.3 (d), graphene was exposed by N_2 gas flow for certain durations. The electrical measurement after N_2 gas flow shows a very small down-shift of the charge neutrality point, indicating that N_2 gas flow without DUV irradiation does not affect the hole doping of graphene [78]. The level of hole doping can be estimated by changing the carrier concentration. The carrier concentration change (Δn) of graphene after treatment in this experiment can be estimated by the charge neutrality point shift (ΔV_D), $\Delta n = C_g \Delta V_D / e$, where C_g is the back gate capacitance, and e is electron charge. By using the back gate capacitance (C_g) in our Si/SiO_2 substrate, 101 aF/μm^2, we show Δn after the time duration in O_2 and N_2 gas flow with or without DUV irradiation, as can be seen in Fig. 5.4. After 60 min DUV irradiation in O_2 gas flow, Δn increases to 3×10^{12} cm^{-2}. The increment of the carrier concentration is very small for the gas flow without DUV irradiation. The carrier concentration is completely restored to the initial state after 60 min DUV irradiation in N_2 gas flow. However, the treatment by N_2 gas without DUV irradiation hardly affects the carrier concentration of graphene. The adsorption of oxygen on the graphene film has already been studied [78]. However, we find that the doping effect due to oxygen is greater when graphene is exposed by DUV light. Conversely, the minimum amount of energy is required to release oxygen from the

graphene surface. Therefore, during N_2 flow under DUV light, nitrogen atoms react with oxygen atoms and desorbs oxygen atom from the surface of the graphene. DUV light would be able to provide enough energy to bring about electron adsorption or desorption from the surface of the graphene.

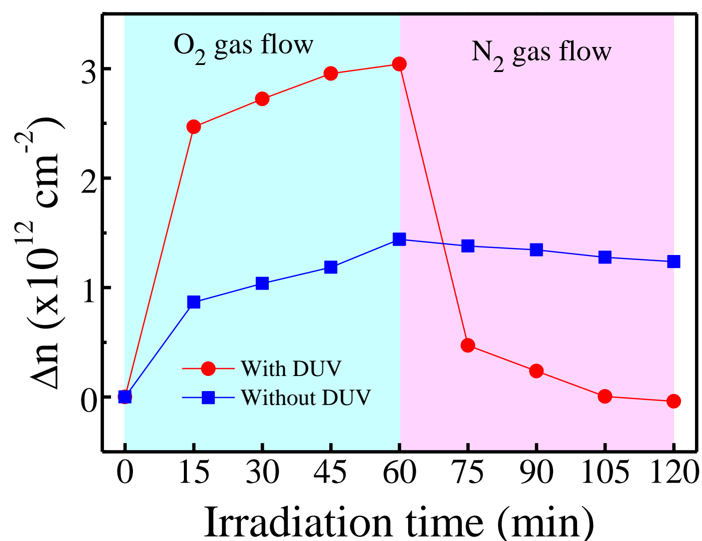

Figure 5.4. Carrier concentration change (Δn) as a function of exposure time for DUV irradiated graphene in O_2 flow and DUV irradiated graphene in N_2 flow after DUV/O_2. Charge neutrality point for graphene in O_2 flow and graphene in N_2 flow after the O_2 flow treatment.

5.3.3 X-ray photoelectron spectroscopy of pristine and DUV irradiated graphene

The absorption and desorption of oxygen is further identified using XPS spectra. For pristine CVD graphene, only C-C is observed at 284.6 eV. However, an additional peak evolves as a result of oxidation at 288.5 eV, which is attributed to the C-O bond, as shown in Fig. 5.5 (a). This peak is found to be slightly broadened and appears at 284.5eV, where the downward shift is caused by hole doping [13, 39]. During DUV/O_2 treatment, the oxygen atoms become more reactive after gaining energy from DUV light, and further chemically react with carbon atoms of graphene, which leads to the formation of epoxide groups [39, 76, 79]. The deconvoluted XPS spectrum after DUV/O_2 treatment is shown in Fig. 5.5 (b). This slightly broad peak with additional shoulder peaks can be fitted by three peaks. The C-C bond peak appears at~284.5 eV, while the other two peaks appear at~285.9 eV and ~288.5 eV, which correspond to C-O and C=O bonds, respectively [80]. The formation of C-O and C=O bonds evidently represents the formation of oxygen-containing groups on the graphene surface [79]. However, these C-O and C=O peaks vanish after DUV/N_2 treatment on graphene, which indicates the recovery of graphene to its pristine state.

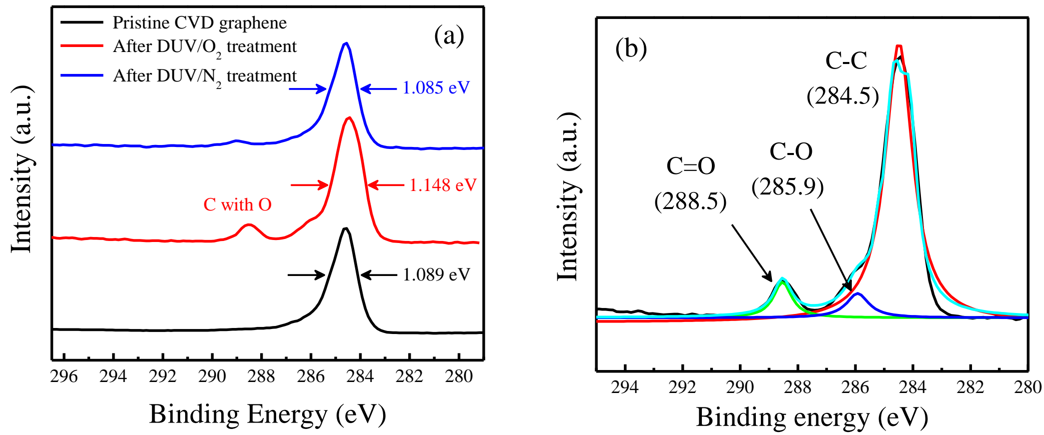

Figure 5.5. (a) C 1s XPS spectra of pristine CVD grown graphene (black curve), after being oxidized with DUV/O_2 (red curve) and then recovery with DUV/N_2 treatment. (b) The deconvoluted spectra after DUV and oxygen treatment show the appearance of the oxygen containing groups on the graphene.

We have performed further experiments on pristine and doped graphene to eliminate ambiguities and to arrive at a better understanding of the role of DUV irradiation. Resistivity of pristine graphene as a function of back gate voltage is studied for various exposure times of DUV irradiation in N_2 gas flow. The pristine graphene shows the charge neutrality point at ~13 V, as one may see in Fig. 5.6 (a). As the exposure time of DUV irradiation in N_2 gas flow increases, the charge neutrality point decreases and reaches at ~5V after 60 min exposure time. The treatment by DUV irradiation in N_2 gas flow (DUV/N_2) removes oxygen from graphene, reducing p-doping by oxygen adsorbates. Oxygen adsorbs on the graphene surface during the sample fabrication process.

We note that the overall resistivity of graphene does not change by DUV/N_2 treatment. The shift of the charge neutrality point of graphene has been examined after various exposure times of N_2 gas flow without DUV irradiation, as shown in Fig. 5.6 (b). The shift of the charge neutrality point is only 1 V from ~16 V for the pristine graphene to ~15 V for 60 min exposure time. The treatment without DUV irradiation is not effective for removing oxygen adsorbates on graphene. After graphene is p-doped by DUV irradiation in O_2 gas flow for 60 min, the graphene sample is exposed to N_2 gas flow. The gate voltage-dependent resistivity of the p-doped graphene sample after a certain exposure time to N_2 gas flow without DUV irradiation. The effect of this treatment is found to be very small compared to DUV/N_2. The charge neutrality point shifts only from ~53 V to ~50 V after 60 min N_2 gas flow, as shown in Fig. 5.6 (c). We find that DUV irradiation is necessary to reverse the hole doping, while the hole doping itself remains almost same with only N_2 gas flow. The graphene is hardly restored to the undoped state by this treatment. A summary of the three treatments may be seen in Fig. 5.6 (d). The shift of the charge neutrality point after each treatment shows the effectiveness of desorption of oxygen adsorbates from graphene. The largest shift occurs for treatment with DUV irradiation. The DUV treatment in N_2 gas flow may be used for purifying graphene from p-doping caused by the sample fabrication process. Stability of doping is an important

requirement for device applications. We note that the treatment developed in this work makes very stable doping of graphene. It is known that physically adsorbed gaseous molecules are easily desorbed in the atmospheric environment. However, we find that the treatment by using O_2 gas flow under DUV irradiation results in a stable doping of graphene. The p-doping state of graphene has been maintained for two months in the atmospheric environment, as shown in Fig. 5.6 (e).

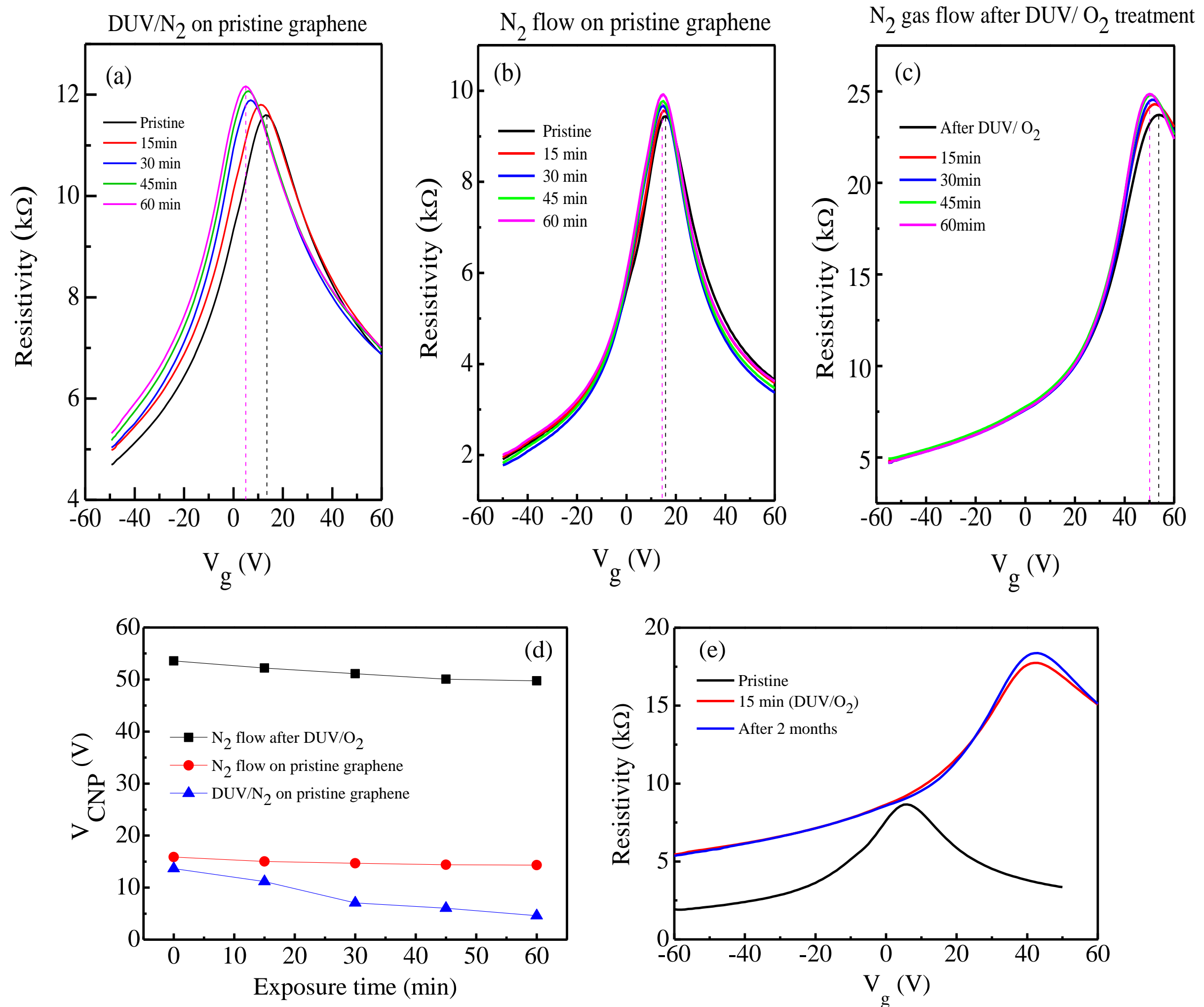

Figure 5.6. (a) Resistivity as a function of back gate voltage after DUV illumination in N_2 gas flow on pristine graphene. (b) Resistivity of graphene as a function of back gate voltage after exposure to N_2 gas flow. (c) Resistivity of p-doped graphene as a function of back gate voltage after N_2 gas flow. The graphene sample was p-doped by 60 min DUV/ O_2 treatment before the measurement. (d) Change of charge neutrality point (V_{CNP}) as a function of exposure time for the N_2 gas treatments. (e) Stability of doping after DUV/O_2 treatment. Resistivity as a function of gate voltage remains almost unaffected after 2 months in the atmospheric environment.

5.3.4 Photo-conductance measurement of the graphene transistor in DUV, DUV/O_2 and DUV/N_2 environments

Finally, conductance as a function of time intervals in three different environments such as DUV, DUV/O_2 and DUV/N_2 facilitates the generation of efficient photocurrent in graphene, as shown in Fig. 5.7 (a). The DUV and DUV/O_2 environments show relativity good photocurrent response in comparison with DUV/N_2. Photo-conductance responses as a function of time with continuous irradiation of DUV/O_2 and DUV/N_2 are shown in Fig. 5.7 (b). Photo-conductivity rapidly increases for the case of DUV and DUV/O_2 in contrast to the case of DUV/N_2.

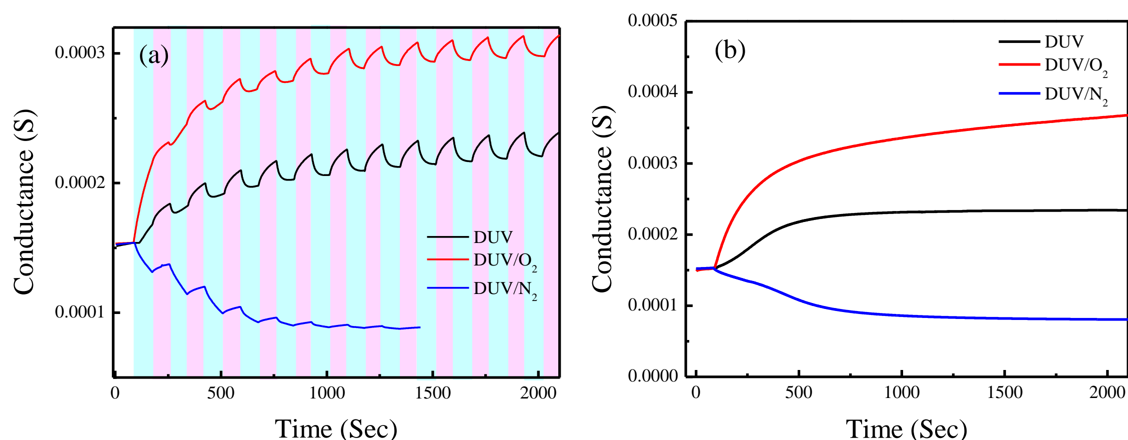

Figure 5.7. (a) Photo-conductance measurement of the graphene transistor in DUV, DUV/O_2 and DUV/N_2 environments. (b) Continuous sweep of conductance curve versus time with DUV irradiation (black) DUV /O_2 (red) and DUV/N_2 (blue).

5.4 Conclusion

In conclusion, we have developed an effective doping method for large area CVD grown graphene. The doping methods developed in this work have the advantage that graphene doping can be performed without disturbing the physical configuration of the graphene device. Moreover, the doping effect is stable and can also be restored to the neutral state without disturbing the physical configuration of the device. The dissociated oxygen atoms, O_2 and O_3 molecular species are thought to induce hole doping to graphene. In the reversing process, oxygen atom is transformed into a NO molecule in a nitrogen gas environment, while the O_2 and O_3 molecules, combined with N atoms, change to NO and NO_2 molecules. Then NO and NO_2 molecules are desorbed from graphene with the aid of DUV irradiation. The doping method using gas flow has so far proved to be unstable in an atmospheric environment. However, the doping by gas molecules with DUV irradiation is a feasible method to be applied in various graphene devices, and the generation of efficient photocurrent enables the integration of high-efficiency sensing and optoelectronic devices.

Chapter 6

6 The structural and electrical evolution of chemical vapor deposition grown graphene by electron beam irradiation induced disorder

The defect formation mechanism in chemical vapor deposition grown single layer graphene devices has been investigated by increasing the electron beam (e-beam) irradiation doses gradually up to 750 e^-/nm^2. The evolution of *D* peaks in Raman spectra provides evidence of strong lattice disorder due to e-beam irradiation. Particularly, the trajectory of *D* and *G* peak intensities ratio (I_D/I_G) suggests that graphene changes from crystalline to nanocrystalline and then towards the amorphous form when the irradiation dose increases. The defect parameters were calculated by phenomenological model of amorphization trajectory for graphitic materials. Mobility decreases gradually from ~1200 to ~80 cm^2/V s as the irradiation dose gradually increases, which implies the formation of localized states in e-beam irradiated graphene. The Dirac point shifts towards negative gate voltage, which indicates n-doping in graphene on increasing the e-beam irradiation dose.

6.1 Introduction

Graphene has recently attracted much attention due to its fascinating properties, such as its extremely high mobility, quantum electronic transport and high elasticity [6, 10]. These properties demonstrate the potential application of graphene in future solid-state devices and as a candidate as an alternative to traditional semiconductors. Growth on a metal substrate by chemical vapour deposition (CVD) is the most promising and the cheapest technique for the production of large area graphene, among various other methods [13, 57]. It is also compatible with the current large-scale integrated circuit fabrication processes [13, 73, 81, 82]. However, the absence of a band-gap in the pristine graphene makes it unsuitable for transistors with a high on-off ratio [83]. Hence, tailoring the electronic properties by means of defects and geometrical confinement is important in order to realize graphene as a competitive material for future electronics [84, 85].

Graphene-based nanodevices are currently being studied extensively. The fabrication and characterization of graphene devices often require an extensive use of scanning electron microscopy (SEM) and transmission electron microscopy (TEM), which are sources of e-beam. The irradiation of e-beam may damage the graphene lattice and can create some defects. Recently, polymethyl methacrylate (PMMA) has also been used as insulating layer to the top gate electrode in field effect transistor of graphene devices [86]. The creation of the PMMA insulating layer on top of the graphene requires significant amount of e-beam

dose. Therefore, the intentional or unintentional use of sources of e-beam (SEM and TEM) strongly affects the intrinsic properties of graphene [16, 64]. Some research groups have reported the effect of electron and ion beam radiation on exfoliated graphene [16, 29, 64, 87-91]. A. A. Balandin and co-workers have extensively investigated the effects of e-beam irradiation on the structural, electronic and thermal properties of mechanical exfoliated graphene sheets [16, 75, 92-95]. Recently, some effects of e-beam irradiation on CVD grown graphene have been reported [25]. The lattice defects due to irradiation can be considered as a potential source of intervalley scattering, which could in principle induce insulating behavior in the e-beam irradiated graphene [96]. However, a detailed investigation is still required to study the effects of e-beam irradiation on CVD grown graphene for its practical use and basic scientific interest.

Here we present the systematic study of the effect of e-beam irradiation on CVD grown graphene. The effects of an electron beam of various doses (125 to 750 e^-/nm^2) are investigated by Raman spectroscopy and transport measurements. The resistivity versus back gate voltage measurement shows the shift of the Dirac point towards negative gate voltage on increasing the dose of e-beam irradiation. The shift of the Dirac point position towards negative gate voltage is an indication of electron doping and is also confirmed by the red shift of *G* and *2D* peaks in Raman spectra. The growth of the *D* and *G* peak intensities ratio with increasing irradiation dose leads to an amorphization trajectory, which suggests that the structure of graphene film transforms from crystalline to nanocrystalline and then to an amorphous form. The crystalline size is estimated by the Tuinstra-Koening and Ferrari-Robertson relation and the defect parameters are theoretically calculated, which is in excellent agreement with experimental results.

6.2 Experimental

The CVD graphene samples are synthesized by same method as previously discussed in Chapter 4 [19, 25, 59]. The CVD grown graphene film on Cu foil is transferred after spin-coating a thin layer of PMMA on the SiO_2 (300nm)/Si (p-doped) substrate [19, 25, 59]. The CVD grown graphene on the SiO_2/Si substrate is kept in acetone for one day to completely remove the PMMA layer from the graphene surface; it is then rinsed in methanol and dried with nitrogen gas. The transferred CVD graphene on SiO_2 substrate is pre-patterned with big electrodes and alignment marks (Cr/Au of 5/30 nm) fabricated by photolithography. The unwanted CVD graphene is removed by a combination of photolithography and oxygen plasma etching techniques. The inner electrode is made by e-beam lithography and evaporation of Cr/Au (5/55 nm) for transport measurement. The exact location of the area of exposure is identified by using alignment marks. The e-beam irradiation of different dose is conducted by using the Raith GmbH lithography system, which permits an accurate control of the irradiation dose and the location of the exposed area. The experiment is performed with accelerating voltage of 20 keV of e-beam, at a working distance of 3.55 μm. The Faraday cup of the sample stage is used to measure the beam current, which is 14.9 pA for this experiment. The

dose is applied in such a way that the electrodes circumvent the exposure to the e-beam irradiation of the graphene channel.

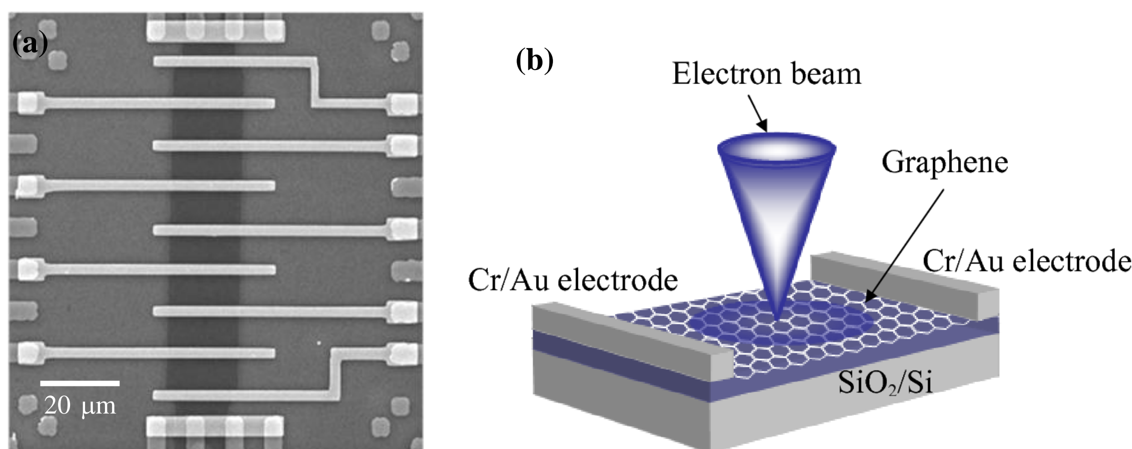

Figure 6.1. (a) Scanning electron micrograph (SEM) image of the device fabricated by simultaneous process of photo- and e-beam lithography. The graphene appears as a dark color in the middle of micrograph. (b) Diagram of e-beam exposure on graphene channel.

Raman spectra are measured with a Renishaw micro-spectrometer over a wave number from 1100 to 3200 cm^{-1} with the laser power 1 mW and wavelength of 514.5 nm at room temperature. The back-gate dependent electrical measurements are performed to examine the modification in resistivity by e-beam irradiation. Fig. 6.1(a) is the scanning electron micrograph image of the fabricated device, and Fig. 6.1(b) shows the graphene channel by e-beam exposure.

6.3 Results and discussion

6.3.1 Evaluation of Raman spectra of e-beam irradiated graphene

Figure 6.2 shows the Raman spectra of pristine and e-beam irradiated graphene samples at room temperature for various doses from 125 to 750 e^-/nm^2. The *D* and *G* peaks appear around 1347 and 1587 cm^{-1}, respectively as shown in Fig. 6.2(a), and these values are similar to those previously reported values obtained in pristine CVD grown graphene [97]. However, the very small *D* peak in pristine CVD graphene indicates high quality graphene. The *D* peak is attributed to A_{1g} symmetry phonons near the *K*-zone boundary. These phonons are not Raman active due to the momentum conservation in the scattering, and require a defect for their activation [98]. The *G* peak corresponds to the in-plane bond stretching motion of the pairs of carbon atoms with E_{2g} optical phonon at the Brillouin zone centre. The increase of *D* and *D'* peaks with increasing e-beam irradiation suggests that the disorder has been induced. Initially, the intensity of both *D* and *D'* peaks increases on increase of the dose after each irradiation step. However, after a certain e-beam dose, this trend is reversed and is observed for both *D* and *D'* peaks. The *2D* peak is the second order of the *D* peak and appears around 2690 cm^{-1}, which originates from a process where momentum

conservation is satisfied by two phonons with opposite wave vectors; no defects are required for their activation and thus they are always present. The change of *D, G* and *D'* peaks affected by e-beam irradiation are evaluated by the multiple Lorentzian curve fittings, as shown Fig. 6.2 (b). Fig. 6.3(a) shows the shift in the *D* peak position and the full width half maximum (FWHM) of *D* peak as a function of the e-beam irradiation dose. The FWHM of *D* peaks and shift in peak positions for the pristine and e-beam irradiated graphene are obtained by using the Lorentzian fit in Raman spectra from Fig. 6.2(b). The FWHM of the *D* peak decreases up to a certain value of irradiation doses, while for higher doses it returns towards the original magnitude. The *D* peak becomes sharper from 125 to 375 e^-/nm^2 irradiation doses, and the magnitude of FWHM has a smaller value in this regime. The positions of the *G* and *2D* peaks as functions of the irradiation dose are shown in Fig. 6.3(b), and these peaks shift towards lower wave number with a gradual increase in the irradiation dose similar to the *D* peak. The inset in Fig. 6.3(b) shows the crystalline size (L_a) of graphene as a function of the e-beam irradiation dose. The value of L_a decreases rapidly as the e-beam irradiation dose increases, which indicates that graphene transforms from a crystalline to an amorphous state. Fig. 6.4 (a) shows the intensity ratio of the *D* and *G* peaks (I_D/I_G) as a function of crystalline size. This plot is divided into two regions. Initially, the I_D/I_G ratio increases up to a certain value of the irradiation dose, while in the second region, when it reaches a certain limit it drops down gradually on further increase of the e-beam irradiation dose. This trend can be explained by the amorphization trajectory model proposed by A. C. Ferrari et al. [45].

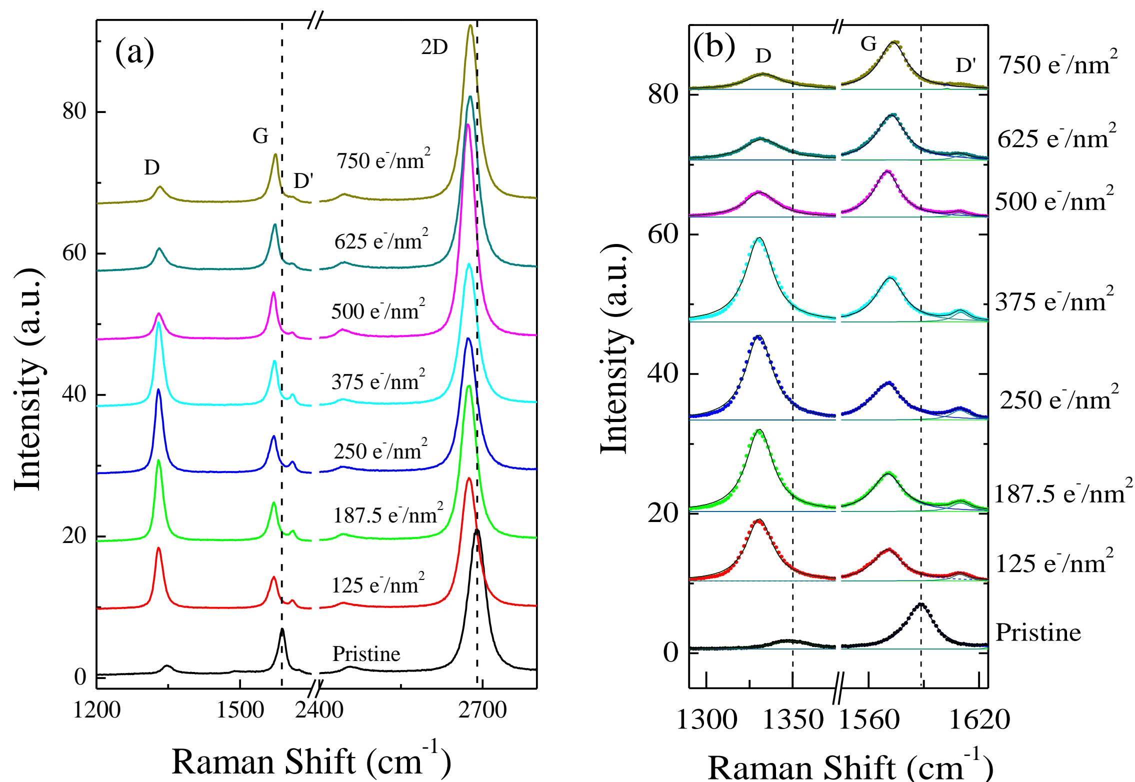

Figure 6.2. (a) Raman shift for various e-beam irradiation doses. The peaks *D, G* and *2D* appear around 1347, 1587 and 2690 cm^{-1}, respectively. The disorder induced *D* and *D'* peaks is raised after e-beam irradiation. (b) Evaluation of Raman spectra by the multiple Lorentzian curve fittings of *D, G* and *D'* peaks, respectively with measured data.

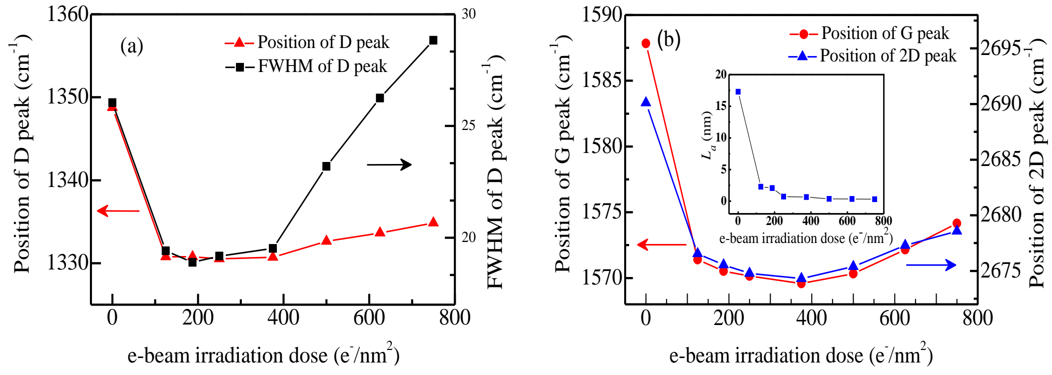

Figure 6.3. (a) Position and full width half maximum (FWHM) of *D* peak as a function of e-beam irradiation dose. (b) Position of *G* and *2D* peak as a function of e-beam irradiation dose. Inset: Crystalline size *(L_a)* as a function of e-beam irradiation dose.

The first trend, i.e. the increase of I_D/I_G, specifies that the crystalline graphene is transformed into a nanocrystalline form, and the second trend, i.e. the gradual decrease in the I_D/I_G ratio, suggests that nanocrystalline graphene is transformed into an amorphous carbon film. This is due to the large number of defects introduced at a higher dose, and most parts of nanocrystalline graphene are converted into an sp^2 amorphous carbon film. The region below 375 e^-/nm^2 e-beam irradiation doses corresponds to the nanocrystalline phase, and crystalline size *(L_a)* of this phase can be estimated by the Tuinstra-Koening relation ($I_D/I_G \propto 1/L_a$), as shown in Eq. (1), where $C(\lambda)\approx$ 4.4 nm (at exciting laser light λ= 514 nm) [99]. However, the second region, which has above 375 e^-/nm^2 e-beam irradiation doses, follows the Ferrari and Robertson relation ($I_D/I_G \propto L_a^2$), as shown in Eq. (2) [45]. Here $C'(\lambda)\approx$ 0.58 /nm^2 is estimated by consistency of I_D/I_G at the irradiation dose of 375 e^-/nm^2. The resulting plot of I_D/I_G ratio as a function of L_a calculated for both regions is shown in Fig. 6.4 (a). The I_D/I_G ratio decreases on increasing L_a in the region where L_a > 2 nm, i.e. the nanocrystalline state, and the ratio increases in the region where L_a < 2 nm, i.e. the amorphous state. This region is represented as amorphous sp^2 carbons film having lower values of L_a. The value of I_D/I_G ratio is consistent with the previous observation for CVD graphene [25].

$$\frac{I_D}{I_G} = \frac{C(\lambda)}{L_a} \qquad (1), \qquad\qquad \frac{I_D}{I_G} = C'(\lambda)L_a^2 \qquad (2)$$

$$\frac{I_D}{I_G} = C_A \frac{r_A^2 - r_S^2}{r_A^2 - 2r_S^2}\left[\exp\left(\frac{-\pi r_S^2}{L_a^2}\right) - \exp\left(\frac{-\pi\left(r_A^2 - r_S^2\right)}{L_a^2}\right)\right] + C_S\left[1 - \exp\left(\frac{-\pi r_S^2}{L_a^2}\right)\right] \qquad (3)$$

Here, we have fitted Eq. (3) to calculate the structural disorder in graphene as in the previously reported model used to calculate structural disorder by Ar^+ ion bombardment [27]. The two regions with different length scales are defined by structurally disordered and active regions. The r_S and r_A are the radii of the structurally disordered and activated regions, respectively, and here r_A is always greater than r_S. As the defect density increases, the *D* band intensity also increases and then reaches a maximum. Meanwhile, the activated regions start to overlap and these regions eventually saturate. By further increasing the defect density in graphene, the *D* band intensity decreases because structurally the disordered areas start to

dominate. The C_A parameter in Eq. (3) is a measure of the maximum possible value of the I_D/I_G ratio in graphene. Theoretically, the parameter C_A could be possible only when mixing of *K-K'* wave vector is allowed. However, in this situation there would be no structural change in the hexagonal network of carbon atoms. Therefore, C_A can be defined in terms of electron-phonon coupling elements between the Γ and *K* points [100]. The C_S parameter is the value of the I_D/I_G ratio in the highly disordered limit. The red line curve is in excellent agreement with the experimental results in Fig. 6.4(a), by taking the parameters C_A = 5.20048, C_S = 0.34096, r_A = 1.56084 nm and r_S = 1.08089 nm. The experimental data and fitting curve are plotted in log-log scale for clarity in Fig. 6.4 (b).

The electron energy loss is an important parameter to describe the influence of irradiation effect. We can estimate the electron energy loss, ΔK, in the graphene by using the relation ΔK = (δE/δx).t. Here, t is the thickness of the graphene layer and δE/δx is the electron stopping power, which is governed by inelastic interactions with the target material. It contributes to various physical phenomena, such as ionization of the target atoms and electronic excitations, and leads to local bond breaking and amorphization. It has a value of 2.89 eV/nm for graphitic materials [101]. Using t= 0.34 nm [102], the estimated energy loss is found to be ~0.893 eV for graphene [101, 103].

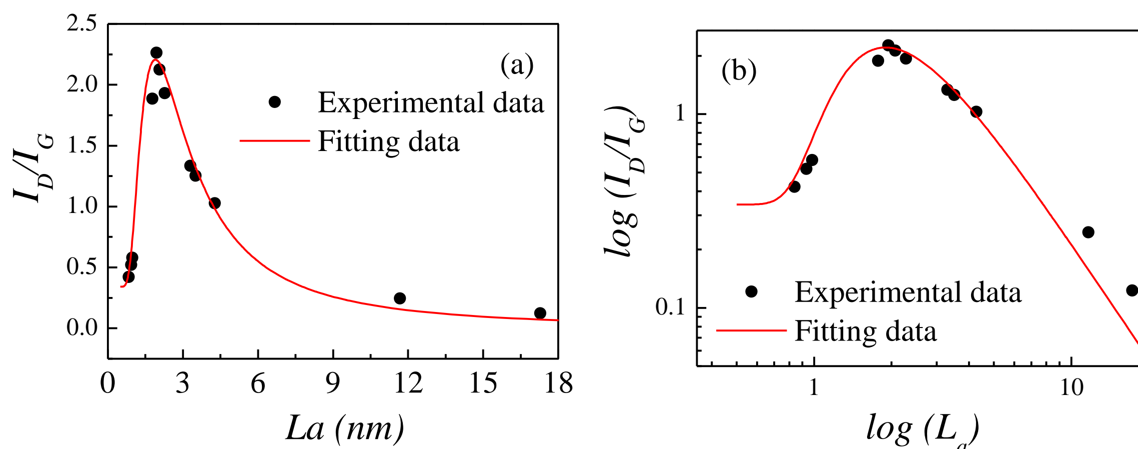

Figure 6.4. Implementation of Eq. (3) on I_D/I_G as a function of average distance L_a between defects, induced by e-beam irradiation. Instead of the integrated area ratio, we use the intensity ratio, because below L_a ~2 nm, the *G* and *D'* peaks overlap. The solid red line is the theoretical modelling data of Eq. (3) and the black dots are the experimental data. (b) The theoretical fit obtained by using Eq. (3) and experimental data of I_D/I_G vs. L_a are plotted on a log-log scale for clarity.

6.3.2 Transport measurements of E-beam irradiated graphene devices

The effect of an e-beam irradiation dose on graphene lattice modification is studied by measuring resistivity as a function of back-gate voltage (V_g) for various e-beam irradiation doses, as shown in Fig. 6.5(a). Resistivity is calculated by using $\rho=RW/L$, where *R* is the measured resistance, *W* is width and *L* is the length of graphene channel. The Dirac point shifts from 18 V to -9.5 V with controlled e-beam exposure and resistance persistently increased with a higher dose exposure. This implies that e-beam irradiation tunes

the transport properties and transforms graphene doping from the hole type to electron type doping. In order to analyze the difference between pristine and irradiated samples quantitatively, we employ the semi-classical Drude model to calculate the mobility, $\mu=(ne\rho)^{-1}$, where ρ is the resistivity, $n=C_g|V_g-V_{Dirac}|/e$ and C_g is gate capacitance taken to be 115 aF/μm² for 300 nm SiO_2 substrate [104], which is the same as that obtained from our Hall measurements. Fig. 6.5(b) shows the trend of mobility of the graphene device as a function of the irradiation dose, and the mobility is found to decrease gradually from ~1200 to ~80 cm²/V sec as the e-beam irradiation dose increases. The inset in Fig. 6.5(b) shows the resistivity at the Dirac point as a function of the irradiation dose, and it is observed that resistivity rapidly increases on increasing the e-beam irradiation dose. The increase in the device resistance supports the amorphization trajectory, which suggests that graphene is transformed into the nanocrystalline and then into the amorphous form when e-beam irradiation is increased. Therefore, we may conclude that graphene becomes amorphous rather than re-crystalline at a higher e-beam irradiation.

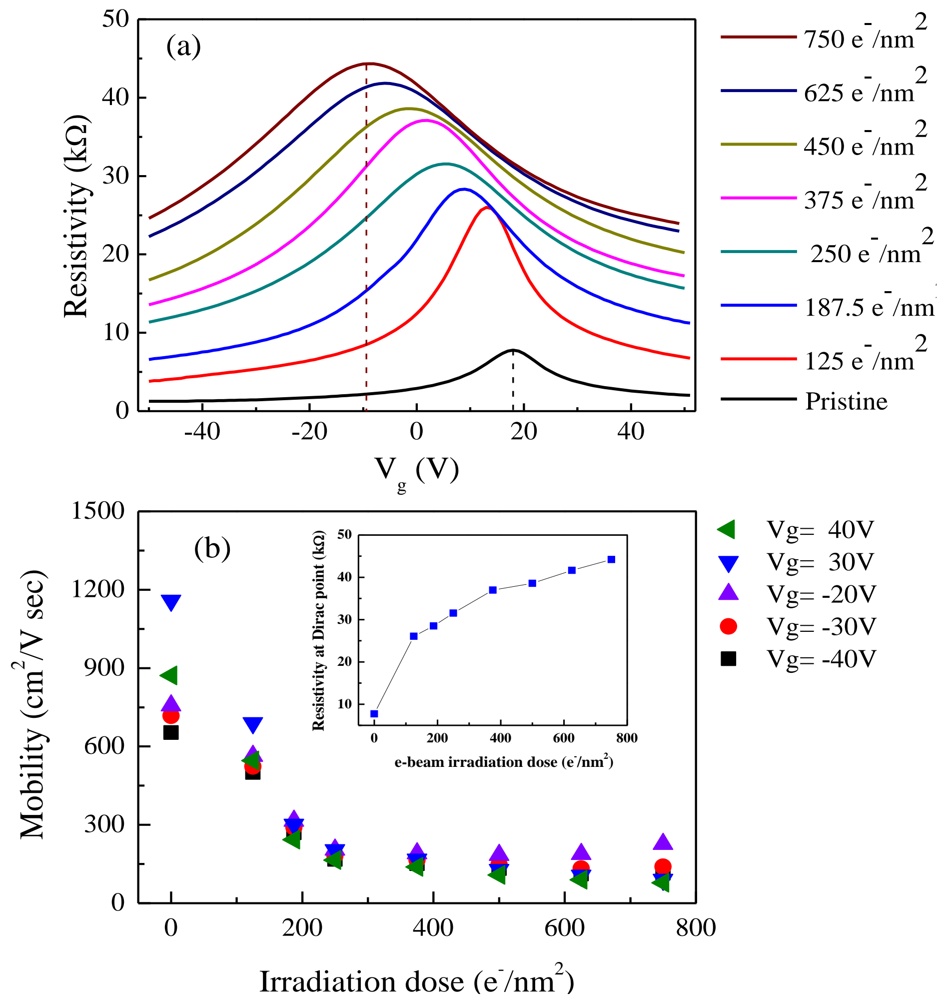

Figure 6.5. (a) Resistivity of graphene as a function of back gate voltage (V_g) for various doses. (b) Mobility of graphene as a function of e-beam irradiation dose at different gate voltage. The inset shows the resistivity at the Dirac point as a function of the e-beam irradiation dose.

6.4 Conclusion

We have introduced the defects in inductively-coupled plasma-enhanced chemical vapor deposition-grown graphene by e-beam irradiation. Raman spectra and transport measurements reveal the mechanisms of disorder formation in graphene. The appearance of a large *D* peak is attributed to lattice damage of the graphene layer upon applying e-beam irradiation. The evolution of *D* and *G* peak intensities ratio (I_D/I_G) follows the amorphization trajectory with increasing irradiation dose, which implies that graphene is converted from a crystalline form into a nanocrystalline form, and then after a certain limit it is transformed into an amorphous form. The crystalline size is calculated by the Tuinstra-Koening and Ferrari-Robertson relations, and the quantification of defect parameters is performed by fitting the phenomenological model of the amorphization trajectory for graphitic materials, which is consistent with experimental results. In transport measurements, the Dirac point shiftd towards negative gate voltage, indicating the n-doping in graphene. Resistance increases persistently and mobility decreases gradually from ~1200 to ~80 cm^2/V sec with a higher dose exposure. This may be attributed to the formation of disordered states in e-beam irradiated graphene.

Chapter 7

7 High frequency impedance of single-walled carbon nanotube networks on flexible substrate

We report the impedance measurement analysis of single-walled carbon nanotube networks (SWCNT), which are expected to be suitable as miniaturized flexible radio frequency RC filters and also have important implications for high frequency devices. The thickness and roughness of the thin film of SWCNT are examined by atomic force microscopy. The Bode plots using two probe measurement setup give the dependence of real and imaginary impedances on frequency. Nyquist plots of carbon nanotube networks on a flexible substrate are close to real circles, indicating that the material is conducting, and suggest a simple equivalent circuit having a resistor in parallel with a capacitor. The tunnels among different carbon nanotubes are capable of storing electric charge. The accumulative capacitances of tunnels for three varied concentrations are calculated by electrochemical impedance spectroscopy simulations to fit the observed Nyquist plots. We have also investigated the frequency dependent impedance measurements of SWCNT network by using Corbino reflectometry setups. The impedance measurements show the cut-off frequency increases with increasing density of SWCNT. High frequency impedance as a function of cut-off frequency reveals the same slope (on the log-log plot) in both measuring techniques and the slope is independent on sample geometries. However, the cut-off frequencies observed by the Corbino reflectometry technique are three orders of magnitude higher than those observed by the two-probe technique, even for the same density SWCNT network.

7.1 Introduction

Thin transparent and flexible networks with randomly distributed single-walled carbon nanotubes (SWCNTs) are emerging as novel materials for various applications, particularly as flexible electronic materials [105-116]. The CNT networks are also expected to be used in the development of logic circuits such as radio-frequency identification tags [117]. These SWCNT network films are useful for flexible networks in different fields, including sensors, electrodes, and filters [116-118]. For such applications, the use of SWCNT networks on flexible plastic substrate has various advantages including fast deposition process, low-temperature and non-vacuum process [105, 113, 116, 119], which help to reduce the cost of the devices. On the other hand, for an efficient use of their functionality it is necessary to understand the electrical properties of thin film of SWCNT networks on flexible substrate [120]. The junction resistance is dominant to the overall resistance in thin film network of SWCNTs because the nanotube-nanotube junction resistance is much larger than the nanotube resistance itself [121-123]. However, the resistance of

nanotube network shows nonlinear behavior with thickness [123, 124]. When the thickness of thin film of SWCNT networks reaches the order of tens of nanometers, the conduction through metallic tubes is dominant resulting in a metallic behavior [125, 126]. It is reported that semiconducting wires, ribbons, and membranes are other promising materials for flexible electronics with high-speed performances because they retain high carrier mobility and relative flexibility [127, 128]. Similar work have reported using Si nano-membranes with a current gain cut-off frequency of 1.9 GHz on plastic substrate for high speed devices, although their flexibility has yet to be studied [129]. The performance of GaAs wires-based transistor is examined up to 1.55 GHz under mechanical stress [130]. Recently, carbon nanotubes have attracted much interest as they offer great potential for high frequency flexible electronics due to their excellent electrical, optical and mechanical properties. Several groups have studied the dc performances of flexible transistors based on SWCNTs, and it has been found that SWCNTs have more advantages than the other materials for their flexible electronic performances [105, 131-133]. The frequency-dependent impedance investigation of different network densities and high value of cut-off frequency is not only helpful to miniaturize the SWCNTs network, but is also important for high speed transistor and transparent shielding material applications. Grüner et al. have investigated the frequency and electric field dependent conductivity of a thin film of the SWCNT network on flexible plastic substrate [134, 135]. They found that the frequency-dependent ac conductivity and nonlinear electric-field-dependent dc conductivity are strongly dependent on film thickness [134, 135]. They also found that the ac conductivity is frequency-independent up to the cut-off frequency (f_0) is defined as where the real part of the impedance decreases suddenly or where the imaginary part has maximum value and that it obeys approximate power law behavior beyond f_0 [134, 135]. Burke and co-workers measured the microwave conductivity of individual SWCNTs and investigated their operation as a transistor at 2.6 GHz [118, 136, 137]. Petit et al. found that conductivities at dc and up to 10 GHz are almost the same for the films with thickness in the range of tens of micrometers [126]. However, there is a lack of high frequency-dependent impedance investigation with systematic variation of network SWCNTs densities and different sample geometries. In addition, determination of the cut-off frequency is yet to be resolved because the impedance measurements by different techniques provide different values of cut-off frequency. The ac-electrochemical impedance spectroscopy (ac-EIS) can be used to characterize the SWNT films. The advantages of ac-EIS analysis over the dc analysis include detail characterization of the local electrical behavior of materials. Generally, ac-EIS measurement techniques employing commercially available frequency response analyzers may not be applicable directly to probe kinetic processes occurring in the materials under a driving force. A single impedance spectrum commonly referred to as a “Nyquist plot” or a “Cole-Cole plot” consists of a set of impedance data collected in a wide range of frequency. Due to such a frequency sweep, it is hardly possible to construct the real time Nyquist plots, which are often required for kinetic studies [138].

We studied the frequency-dependent impedance measurements for SWCNT networks with varying density and different sample geometries. The SWCNTs density of the films is controlled by optimizing the concentration of nanotubes in an SDS aqueous solution. The thickness and transparency are also controlled by the number of spray passes over the substrate. The sample A1 is made by the least number of spray passes, so the lowest density is expected. As the number of spray passes increases from A1 to A8, the density also increases in sequence. We also compare the measurements by different techniques. We found that f_0 extracted from the frequency-dependent impedance measurement remarkably depends on the measurement technique, even for same density SWCNTs network. The cut-off frequency determined by two probe impedance is lower than that of the Corbino reflectometry setup, and their comparisons are discussed in detail. Raman and AFM are also used to characterize SWCNTs network. We also observed that the transmittance of SWCNTs network is closely related to the density of SWCNTs.

7.2 Experimental

The conductive network of SWCNT is prepared on the substrate of polypropylene carbonate (PPC). The SWCNTs are dissolved in a 1% solution of aqueous sodium dodecyl sulfate (SDS), and then the suspension is sonicated for 1 h at 40 W using a probe sonicator. The suspension is then vigorously sprayed on the PC substrate, which is heated at 120 ℃. The heating of the substrate is done to prevent the agglomeration of SWCNTs. After several layers of nanotubes have been sprayed onto the PC, the substrate is submerged and shaken in distilled water in order to remove the rest of SDS. As a result, a conductive layer is deposited on the PC substrate [105]. The samples are made with different densities for characterizations. Raman spectra are taken using the RENISHAW spectrometer having 633-nm laser wavelength under ambient conditions. Surface morphology is recorded by using the atomic force microscope (NanoFocus Inc.). Two-probe contact and the Corbino reflectometry setups, which are ideal for broadband impedance measurements of resistive materials [139], are used to investigate the impedance of the SWCNT networks [112]. The two-probe method is used because SWCNT thin films exhibit high impedance and the contact resistance should be several orders of magnitude lower. In order to measure the impedance in the broad frequency range, two instruments are used, as shown in Fig. 7.1(a) and (b); Agilent E8362B network analyzer with a frequency range from 10 MHz to 20 GHz and Agilent 4294A network analyzer with a frequency range from 40 Hz to 110 MHz.

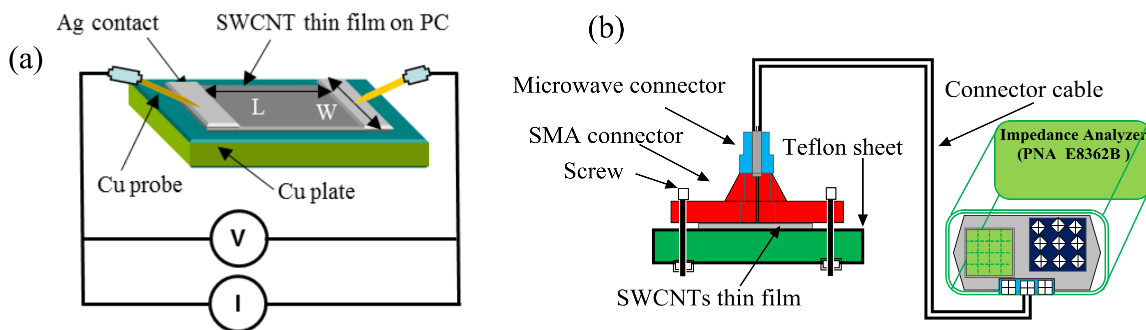

Figure 7.1. Figure 1. (a) Diagram of SWCNT on polypropylene carbonate substrate with Ag contacts in two probe impedance measurement setup (b) Diagram of Corbino reflectometry setup with panel mount SMA connector for microwave frequency range.

7.3 Results and discussion

7.3.1 Raman spectroscopy, surface morphology and optical absorption analysis

Figure 7.2(a) shows the Raman spectra for SWCNTs network with various densities, prepared on flexible PPC substrate. The most characteristic features in Raman spectra of SWCNTs show a behavior similar to that reported previously [140, 141]. The peak at the high energy range from 1550 to 1650 cm^{-1} corresponds to the tangential G mode, and a peak around ~1300 cm^{-1} is related to the inter-band with defect-induced vibration (D mode). The G/D peaks ratio in Raman spectra are 2.017, which is indicative of the high purity of SWCNTs network. Figure 7.2 (b) shows the optical transmittance as a function of wavelength for various SWCNTs network films. The highly dense SWCNTs network shows low transmittance, whereas the slightly dense SWCNTs network shows high transmittance. The inset is the photograph of optically transparent SWCNTs network. The least density of SWCNTs network corresponds to the maximum transparency of ~95 %. Since all the SWCNTs samples are obtained using the same method and made from the same batch, we can relate transmittance to the SWCNTs density.

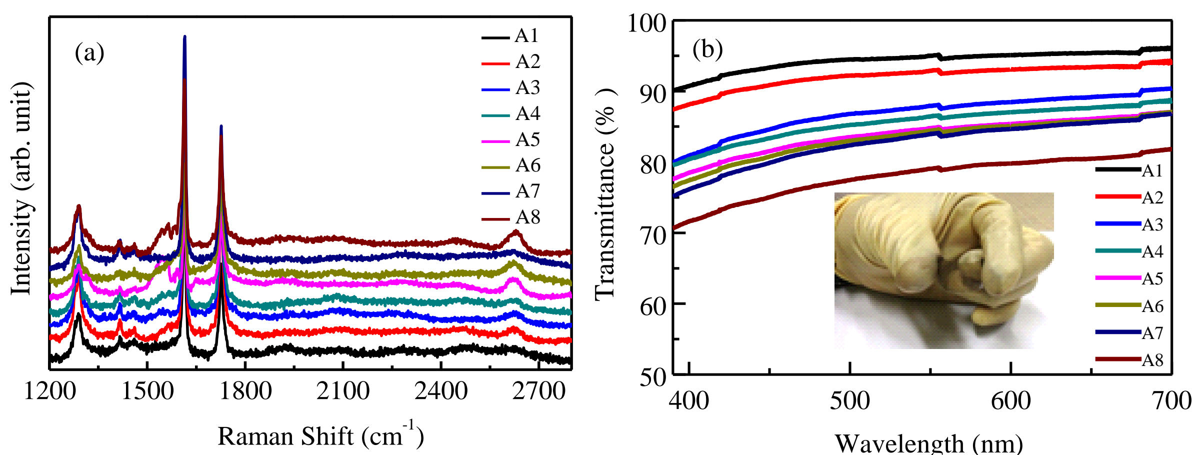

Figure 7.2. (a) Raman spectra of SWCNT thin film network on PC substrate with different densities of CNT used for two-probe and Corbino geometry impedance measurements. (b) Transmittance as a function of wavelength for various density networks. Inset shows the photograph of SWCNT network on polypropylene carbonate flexible substrate.

The surface morphology is studied by atomic force microscopy (AFM) to verify the dispersion of SWCNTs on PPC substrate. As observed from the topography image in Fig. 7.3(a) for sample A1, the cluster network is distributed over a large area of the PPC substrate with mostly uniform thickness. The bright part on the topography image highlighted shows a number of clusters agglomerated on that part of the surface. The root-mean-square (RMS) roughness is estimated to be ~12 nm. The AFM estimated size of CNT bundles to be approximately 15-20 nm. The thickness profile taken by drawing the line in the middle of topography image shows the average thickness of the CNT film~27 nm, as seen in Fig. 7.3(b).

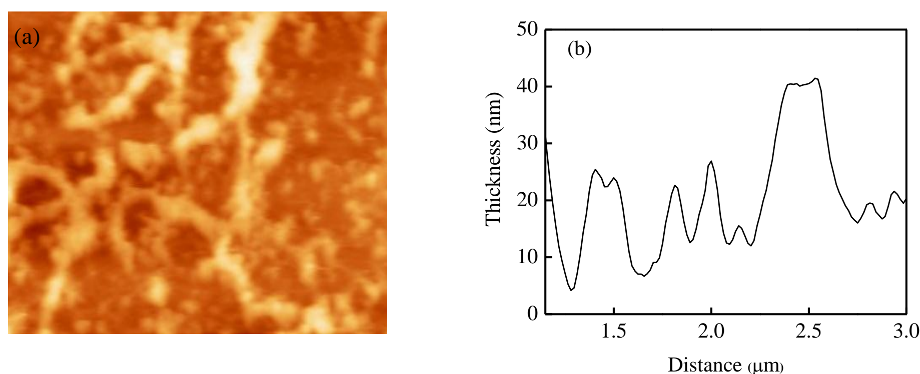

Figure 7.3. (a) AFM image of a nanotube thin film area 4x4 μm^2. (b) Thickness profile taken by drawing the line in the middle of topography image. The average thickness of the SWCNT film is 27 nm and RMS roughness is around 12 nm. The SWCNT bundle size is approximately 15-20 nm.

7.3.2 Impedance analysis with two-probe setup up to 100 MHz

To analyze the electronic characteristics in the SWCNTs network, the impedance measurements are employed on rectangular shape samples with length and width 1.5 and 0.5 cm, respectively, at room temperature. The charge carrier transport through this kind of network is thought to be limited not only by the conductivity along the nanotubes themselves, but by the large inter-tube resistance associated with barriers to charge propagation that arises at the tube-tube junctions. As expected for a network with significant randomness, the impedance is frequency and density-dependent.

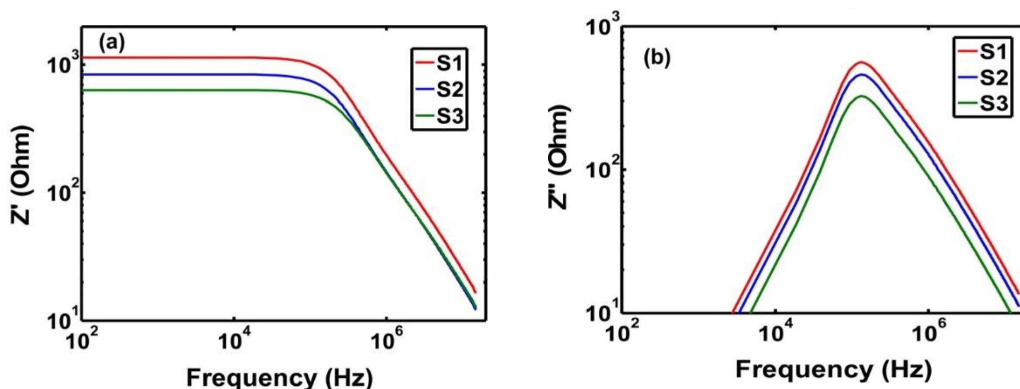

Figure 7.4. Bode plots showing the real (a) and imaginary (b) parts of impedance as a function of frequency for SWCNT thin film networks with different density of samples S1, S2, and S3.

The two dimensional Bode plots for the real component (Z') and the imaginary part (Z'') are shown in Figs. 7.4(a) and 7.4(b), respectively. As observed from Fig. 7.4(a) at low frequencies, the impedance increases as the density of SWCNTs network decreases. The impedance remains constant up to a certain frequency and then starts to decrease at a constant rate. The cut-off frequency is defined as where the real part of the impedance decreases suddenly or where the imaginary part has maximum value. The cut-off frequency in Bode plots is related to the mean distance between nanotubes or gaps in random nanotube networks [112]. Since the gaps between SWCNTs act as a parallel plate capacitor, any increase in the density makes the gaps smaller, while at the same time the impedance decreases when the mean distance between the nanotube network decreases. In the Bode plot, the imaginary component (Z'') increases in the range from 10^3 to 10^5 Hz, while Z' remain constant and both the real and imaginary parts of impedance abruptly decrease as the frequency increases over the cut-off frequency. As can be seen in Fig. 7.5(a), the complex impedance variation with frequency follows an approximately real circle resembling a Debye relaxation peak [142]. At low densities, these conducting networks contain some highly resistive nanotubes, while at higher density pathways are formed among metallic nanotubes. This can be described with a model that includes both semiconducting and metallic pathways [113]. These ideas have been elaborated by other groups [114, 143]. All these models are based on the inherent randomness and driven charge transport across arbitrary barriers.

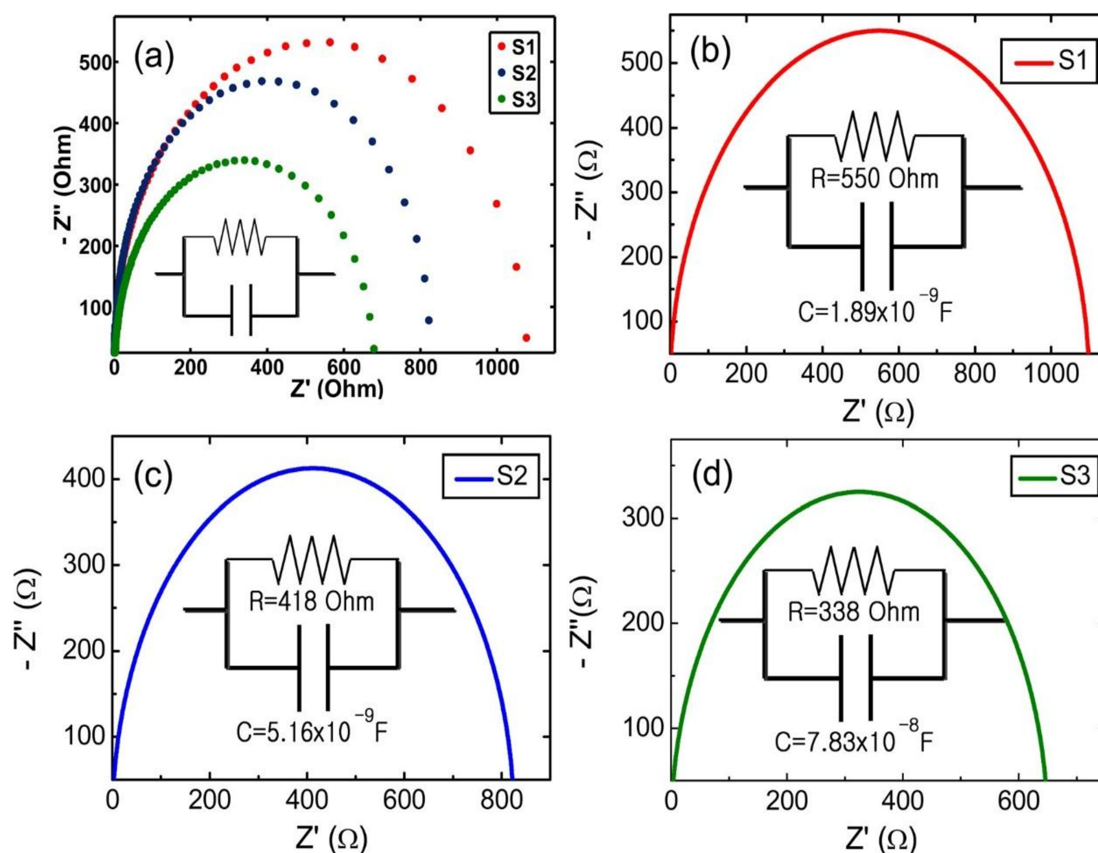

Figure 7.5. (a) Nyquist plot showing the imaginary part (-Z'') vs real part (Z') of impedance of SWCNT thin film networks with different densities of samples S1, S2, and S3. The inset shows a simple equivalent circuit composed of parallel combination of

resistor and capacitor. The electrochemical impedance spectroscopy (EIS) simulation plot (b) for sample S1 with resistance R =550 Ω and capacitance C =1.89 × 10^{-9} F, (c) for sample S2 with resistance R = 418 Ω and capacitance C = 5.16 × 10^{-9} F, and (d) for sample S3 with resistance R = 338 Ω and capacitance C = 7.83 × 10^{-8} F.

The SWCNTs network can serve as semiconducting channels when the density is lower than the percolation threshold, and they serve as a metallic interconnect or as a conducting sheet for high network densities. These results can be simulated by a simple equivalent circuit composed of parallel combination of a resistor and a capacitor [inset in Fig. 7.5(a)]. The contribution of resistance and capacitance is calculated by using electrochemical impedance spectroscopy simulations (EIS), as shown in Figs. 7.5(b)–7.5(d), respectively, while the simulated resistances (R) are obtained as 550, 418, and 338 Ω for three samples S1, S2, and S3, the accumulation capacitances are calculated as 1.89 × 10^{-9}, 5.16 × 10^{-9}, and 7.83 × 10^{-8} F, respectively. The results presented above indicate that band-stop RC flexible filters can be assembled successfully from a carbon nanotube film grown on a flexible substrate. The range of the cut-off frequency can be tuned by varying the density of SWCNTs networks.

7.3.3 Impedance analysis up to 20 GHz

The ac measurements are performed in frequency range from 40 Hz to 110 MHz by two-probe measurement and from 10 MHz to 20 GHz with the Corbino reflectometry setup. Here, we use eight samples with different SWCNT densities. For each density, we prepare four different sample geometries. Three samples with width (W) of 0.5 cm- and different lengths (L) of 1.5, 3 and 6 cm are characterized by the two-probe contact method. The fourth sample, with circular geometry with a diameter (D) of 1.9 mm, is characterized by the Corbino reflectometry setup. A schematic view of the two-probe measurement method is shown in Fig. 7.1(a). The Corbino geometry setup is shown in Fig. 7.1(b). The real and imaginary components of the ac impedance as a function of frequency are presented in Fig. 7.6 and 7.7., while Fig. 7.6 shows the ac impedance measured by the two-probe method, Fig. 7.7 shows the ac impedance measured by Corbino reflectometry setup. In Fig. 7.6(a) and Fig. 7.7(a), the real part of impedance in the frequency range from 40 to 10^5 Hz and from 10^7 to 5× 10^8 Hz is almost constant. In general, the impedance measured at a given frequency reflects typically the response within a length scale of wavelength. Therefore, the impedance measurement will probe longer length scales at low frequencies [135]. This phenomenon is related to the fact that there is not enough time for electrons to cross all the junctions on their way through the nanotube random paths during one period of the electric field, T = $1/f_0$, where $f_0 = 1/2\pi RC_{total}$, R is resistance and $C_{total} = C_Q + C_{ES}$ (C_Q is quantum capacitance, and C_{ES} electrostatic capacitance) of CNT network [118, 144]. In Fig. 7.6(b), the imaginary component (Z″) increases from 10^3 to 10^5 Hz, then both real and imaginary components of impedance start to decrease above a particular frequency, which is defined as the cut-off frequency (f_0). These results are in line with the previous two-probe measurements, as shown in Fig.7.4. However, f_0 in the Corbino reflectometry setup is in the range of 10^9 Hz, which is

higher than that of the two-probe method, as shown in 7.8. The impedance Z(ω) is calculated from measured scattering parameters by the given formula [134], a(= 0.5 mm) and b (= 1.9 mm) are the inner and outer diameters of the sample contact, respectively. S_{11} (ω) is the scattering parameter at an angular frequency, ω.

$$Z_s(\omega) = Z_0 \frac{2\pi}{\ln(b/a)} \frac{1+\widehat{S}_{11}(\omega)}{1-\widehat{S}_{11}(\omega)}$$

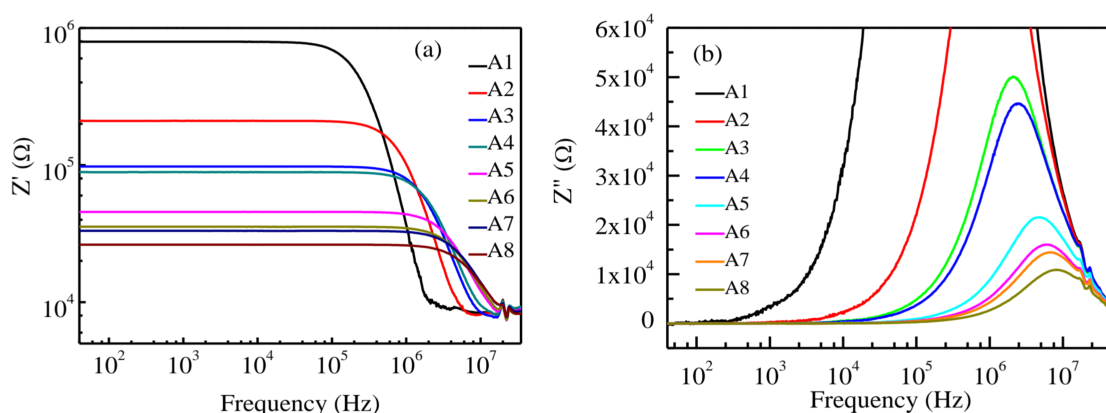

Figure 7.6. (a) Frequency dependence of real component and (b) imaginary component of impedance with various densities of samples measured by two probe method. Length and width of the sample are 1.5 cm and 0.5 cm, respectively.

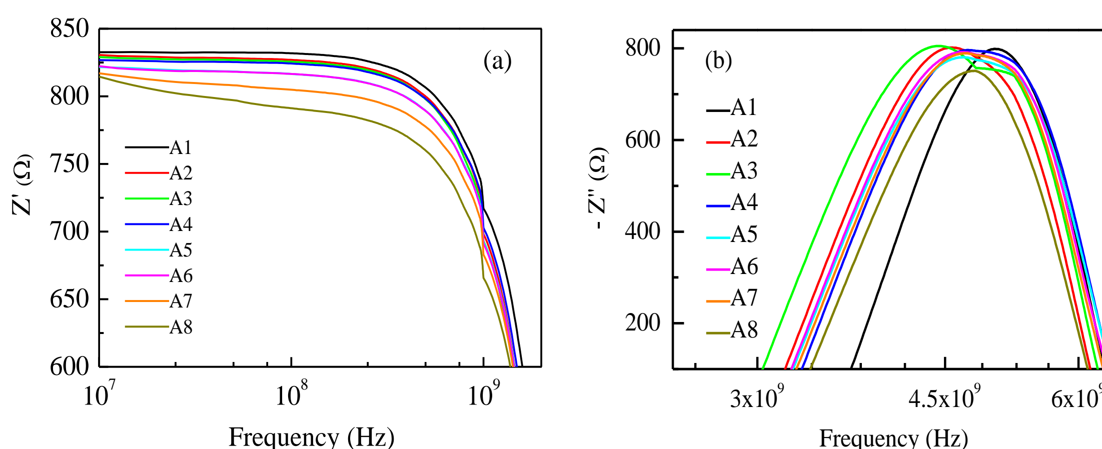

Figure 7.7. Impedance as a function of frequency of SWCNT thin film networks with various densities. (a) Real component and (b) imaginary component measured by Corbino reflectometry (panel mount SMA connector with inner and outer diameters a = 0.5 mm and b = 1.9 mm, respectively) setup.

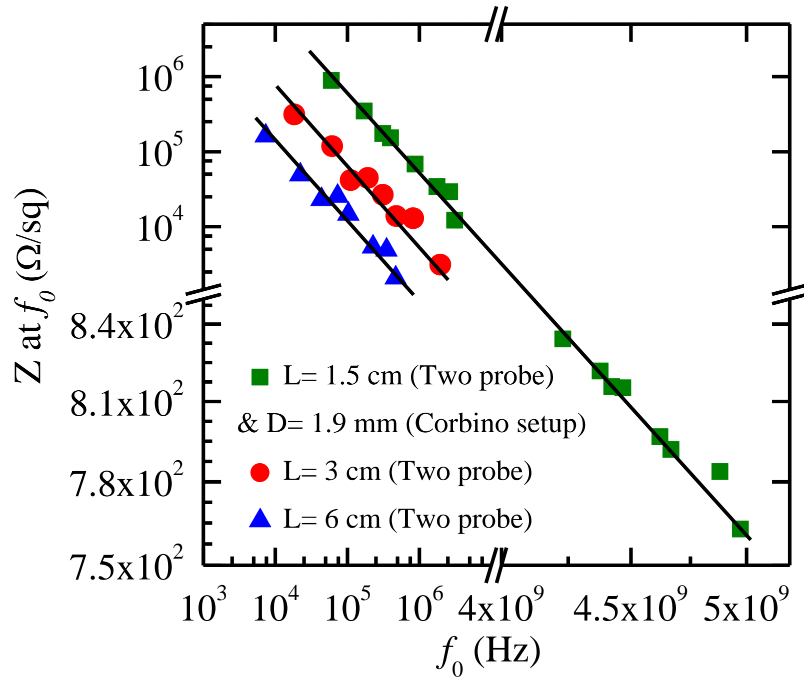

Figure 7.8. The impedance at cut-off frequency as a function of cut-off frequency (f_0) of SWCNT thin film networks with different densities. In the two-probe measurement, the width was 0.5 cm and lengths were 1.5, 3 and 6 cm, respectively. In the Corbino reflectometry setup the circular shape sample has a diameter of D = 1.9 mm.

Figure 7.8 shows the real part of impedance (Z′) at f_0 (on log-log plot) for different samples. The upper group of green points represents the impedance dependence of samples with length L= 1.5 cm measured by the two-probe method. The lower group of green points corresponds to the impedance dependence of samples with diameter D= 1.9 mm measured by the Corbino reflectometry setup. The blue and red points represent the impedance dependence for samples with lengths L= 3 and 6 cm, respectively, measured by the two-probe method. We observe that the impedance dependence on the cut-off frequency of all the samples lies on the same slop. For the two-probe impedance measurements, the impedance measured is probably greater due to high contact resistance [145]. As expected, f_0 not only depends on the density of the network, but also on other factors such as geometry in the measurement setup. The results show that the behavior is mostly determined by the contact resistance between the SWCNTs, which are completely disordered in the network. As the SWCNTs density increases there are more connections between the tubes, which causes the cut-off frequency to increase [135]. These results are in good agreement with the results the previously reported [135], and as predicated by the theory of universality of ac conduction in completely disordered solids and verified experimentally in different solids [146].

7.4 Conclusions

We study the effects of frequency-dependent impedance measurements of SWCNTs network on transparent and flexible substrates between two different measurement techniques; the two-probe setup and

the Corbino reflectometry setup. The large value of the G/D peaks ratio in Raman spectra indicates the high quality of SWCNT networks. AFM analysis shows the large area growth of SWCNTs with uniform thickness on most parts of the substrate. The observations by optical absorption spectroscopy confirm the high transparency from 79 to 95 % for samples with various CNT densities in our experiment. The sharp decrease in impedance obtained by the Bode plots is associated with the mean distance of the SWCNTs network, while the real components of impedance show a constant behavior up to the defined cut-off frequency, after which it decreases abruptly. The imaginary components of impedance show maximum value at cut-off frequency. The Nyquist diagram suggests a simple equivalent circuit composed of a parallel combination of a resistor and a capacitor. The simulated values for these RC circuits fit well with experimental data; the R values decrease and the C values increase as the SWCNTs density increases. The films should be a plausible candidate for a flexible band-stop filter. The impedance measurements show that the cut-off frequency decreases as the density of SWCNTs increases. The log-log plot of ac impedances as a function of cut-off frequency reveal the same slope in all the samples regardless of sample geometry or measurement setup. This can be explained by the theory of ac conduction in very disordered systems.

Chapter 8

8 Summary and outlook

We highlight the importance of the modulation of graphene properties with various kinds of doping. There are several challenges at present for the doping of graphene, such as structural deformation, mobility degradation, controlled doping, reproducibility and unstability. In general, the graphene devices are found to be p-type due to adsorption of oxygen molecules from ambient atmosphere and charge trapping between graphene and substrates. Therefore, some thoughtful strategies are required in order to overcome these challenges.

We tune the graphene properties using various techniques, such as DUV irradiation in ambient atmosphere, DUV irradiation in different gaseous environments, and electron beam irradiation. We investigate the DUV irradiation effect on different number of graphene layers. The tuning of electronic properties of mechanically exfoliated single-, bi-, and trilayer graphenes by DUV irradiation are studied without significantly degrading its charge carrier mobility. To some extent, controlled p-type doping is feasible. We find that DUV irradiation in ambient atmosphere shows the p-type doping effect in graphene, while the doping level can be well-controlled with irradiation time without degradation of mobility. Raman spectroscopy and charge transport measurements reveal that DUV irradiation effects tune the properties of single-, bi-, and trilayer graphene layers towards p-type doping. The shift in of the Dirac point for single-, bi-, and trilayer graphenes is also investigated as a function of DUV irradiation time. It is found that the charge neutrality point is shifted toward positive gate voltage on increasing the DUV irradiation time for all single-, bi-, and trilayer graphenes. However the doping effect slightly decreases when the number of layers is increased, and one may even identify clearly the effect of tunability on multilayer graphene. The results indicate that DUV irradiation is a non-destructive approach to tuning the electrical properties of single-, bi-, and trilayer graphenes, while preserving the electrical properties.

The doping phenomena can be explained by the dissociation of oxygen molecules in the presence of UV light. The dissociated molecules react with graphene to create oxygen-containing groups and induce p-type doping. The shift of the Dirac point position towards positive gate voltages confirms the p-type doping. These oxygen atoms can attach themselves onto the most stable site of graphene. During the photo-oxidation process with DUV light, the O_2 molecules absorb enough energy from photons to form two oxygen ions in the ground state. These dissociated oxygen ions attach themselves to different sites and will remain on the most stable adsorption site of the graphene. The intensity of DUV light determines the change

of carrier concentration in the graphene. However, the change of carrier concentration saturates after a certain limit of time, since only a finite number of dopants can be adsorbed on the graphene surface. This method becomes more useful when half the graphene device is covered and the remaining half is exposed to DUV light so that a sharp p-n junction is constructed. Since DUV light in the atmosphere acts as p-type dopant for graphene, it raises the Fermi level of the p-doped region; however, the untreated region remains at the same Fermi level as pristine graphene. This difference in the Fermi level creates a junction across the boundary. Nevertheless, I-V characteristics curves show linear behavior, because the depletion region is not expected between the doped and undoped region of graphene, due to the gapless band structure.

Furthermore, the DUV effect becomes more prominent and controllable at a higher range when the doping is performed in an oxygen environment. The most interesting phenomena are observed when doping of graphene retreats towards pristine graphene using DUV irradiation in a nitrogen environment. The p-doping effect is observed in an ambient atmosphere with DUV light, as discussed in the above paragraph, and shows a similar trend in an oxygen environment, which indicates p-type doping. The shift of the charge neutrality point increases rapidly with the DUV light on graphene in an oxygen environment. The reversal of hole doping is observed by DUV irradiation under nitrogen gas flow. The resistivity of the graphene field effect transistor devices are found to increase slightly during the irradiation process and effect of DUV irradiation is also compared with simple gas flow treatment. The charge neutrality point is examined after oxygen and nitrogen gas flow without irradiation of DUV light. The hole doping effect is found in the treatment of dry oxygen gas flow without irradiation of DUV light. However, the hole doping effect is smaller than that with DUV irradiation. Subsequent treatment of nitrogen gas flow shows a very small down-shift to the charge neutrality point. We find that the doping effect due to oxygen is more significant when graphene is exposed by DUV light. Conversely, a minimum amount of energy provided by DUV light is required to release oxygen from the surface of graphene. Therefore, during nitrogen flow under DUV light, nitrogen atoms react with oxygen atoms and desorb oxygen atoms from the surface of graphene. We find that the treatment by using oxygen gas flow under DUV irradiation results in a stable doping of graphene. The p-doping state of graphene is maintained for couple of months in the atmospheric environment. The absorption and desorption of oxygen is further identified using XPS spectra. During DUV treatment in an oxygen environment, the oxygen atoms become more reactive after gaining energy from DUV light and further chemically react with carbon atoms of graphene, leading to the formation of epoxide groups. The deconvoluted XPS spectrum after DUV and oxygen treatment shows a slightly broader peak with additional shoulder peaks that can be fitted by three peaks. The first peak is assigned to the C-C bond, whereas the other two peaks correspond to C-O and C=O bonds, respectively. However, these C-O and C=O peaks vanish after treatment with DUV in a nitrogen environment of graphene, which indicates the recovery of graphene to its pristine state.

The structural deformation due to electron beam irradiation is an important factor in graphene device fabrication. We have intentionally irradiated the graphene devices with various controlled doses using electron beam irradiation. The structurally deformed graphene undergoes various phases, where graphene transforms from a crystalline to a nanocrystalline form, and then after a certain irradiation time it changes into amorphous form. The crystalline size is calculated by the Tuinstra-Koening and Ferrari-Robertson relations, and the quantification of defect parameters is performed by fitting the phenomenological model of the amorphization trajectory for graphitic materials, which is consistent with experimental results. The resistance of the graphene devices increases after irradiation. This observation supports the amorphization trajectory, which suggests the transformation of graphene to the nanocrystalline and then to the amorphous form on increasing the e-beam irradiation. During this process, the graphene devices are found to be n-type doped and the doping level is increased by increasing the dose factor. The other important consequence of this technique is that graphene devices which are good conductors of electricity and heat can be transformed into electrical and thermal insulators as well as having important implications for band-gap opening.

The last section of the thesis describes SWCNTs network for different applications to flexible and transparent electronic devices; in particular, to high frequency devices. We fabricate the flexible and transparent electrodes and characterize them by AFM, Raman- and optical absorption spectroscopy. We measure the electrical impedances up to 100 MHz for the two-probe measurements and up to 20 GHz for the Corbino geometry setup. The two dimensional Bode plots for the real and the imaginary components define the frequency-dependent impedance behavior of SWNTs network. The observed results show that at low frequencies the impedance increases as the density of SWCNTs network decreases. The impedance remains constant up to a certain frequency or cut-off frequency and then decreases abruptly. The cut-off frequency in Bode plots is related to the mean distance between nanotubes or gaps in random nanotube networks. Since the gaps between SWCNTs act as a parallel plate capacitor, by increasing the density the gaps become smaller, and as a result the capacitance increases and the impedance decreases. Both the real and imaginary parts of impedance abruptly decrease as the frequency increases over the cut-off frequency. As the SWCNTs density increases there are more connections between the tubes, making the cut-off frequency increase. The cut-off frequency not only depends on the carbon nanotube density of the network, but depends on the geometry in the measurement setup. We observe that the impedance dependence on the cut-off frequency of all the samples lies on the same slope. The Nyquist diagram suggests a simple equivalent circuit composed of a parallel combination of a resistor and a capacitor. The simulated values for these RC circuits fit well with experimental data. The films should be a plausible candidate for a flexible band-stop filter. The results show that the behavior is mostly determined by the contact resistance between the SWCNTs, which have a completely disordered distribution in the network. These results are in good agreement with the previously reported theory of universality of ac conduction in disordered solids.

The systematic study described in Chapters 3, 4, and 5 for tuning the properties of graphene by DUV light has many practical applications. Due to defects free doping and the long-term stability of this technique, it could be applied on an industrial scale and may be further employed with other two-dimensional materials such as MoS_2, WS_2, WSe_2. The controlled defects formation with electron beam irradiation, as described in Chapter 6, can modify the properties of graphene according to the required applications of the devices, and this method can be used to tune the properties of other two-dimensional materials as well. Flexible and transparent electronic devices have great importance in different electronic applications, such as electrodes in photovoltaic cells, sensors and displays. The method described in Chapter 7 is a very simple and cost-effective for large scale production of carbon nanotubes based flexible and transparent high frequency electronics. This method can be improved by controlling the thickness of carbon nanotubes more precisely and selecting the carbon nanotubes.

9 Bibliography

[1]Wallace PR. The Band Theory of Graphite. Phys Rev. 1947;71(7):476-.
[2]Mcclure JW. Diamagnetism of Graphite. Phys Rev. 1956;104(3):666-71.
[3]Slonczewski JC, Weiss PR. Band Structure of Graphite. Phys Rev. 1958;109(2):272-9.
[4]Semenoff GW. Condensed-Matter Simulation of a 3-Dimensional Anomaly. Phys Rev Lett. 1984;53(26):2449-52.
[5]Fradkin E. Critical-Behavior of Disordered Degenerate Semiconductors .2. Spectrum and Transport-Properties in Mean-Field Theory. Phys Rev B. 1986;33(5):3263-8.
[6]Novoselov KS, Geim AK, Morozov SV, Jiang D, Zhang Y, Dubonos SV, et al. Electric field effect in atomically thin carbon films. Science. 2004;306(5696):666-9.
[7]Novoselov KS, Geim AK, Morozov SV, Jiang D, Katsnelson MI, Grigorieva IV, et al. Two-dimensional gas of massless Dirac fermions in graphene. Nature. 2005;438(7065):197-200.
[8]Zhang YB, Tan YW, Stormer HL, Kim P. Experimental observation of the quantum Hall effect and Berry's phase in graphene. Nature. 2005;438(7065):201-4.
[9]Ho JH, Chiu YH, Tsai SJ, Lin MF. Semimetallic graphene in a modulated electric potential. Phys Rev B. 2009;79(11).
[10] Geim AK, Novoselov KS. The rise of graphene. Nat Mater. 2007;6(3):183-91.
[11] Nair RR, Blake P, Grigorenko AN, Novoselov KS, Booth TJ, Stauber T, et al. Fine structure constant defines visual transparency of graphene. Science. 2008;320(5881):1308-.
[12] Das Sarma S, Adam S, Hwang EH, Rossi E. Electronic transport in two-dimensional graphene. Rev Mod Phys. 2011;83(2):407-70.
[13] Bae S, Kim H, Lee Y, Xu XF, Park JS, Zheng Y, et al. Roll-to-roll production of 30-inch graphene films for transparent electrodes. Nat Nanotechnol. 2010;5(8):574-8.
[14] Iqbal MZ, Iqbal MW, Eom J, Ahmad M, Ferrer-Anglada N. Capacitive tunnels in single-walled carbon nanotube networks on flexible substrate. J Appl Phys. 2012;111(6):063712.
[15] Ferrer-Anglada N, Perez-Puigdemont J, Figueras J, Iqbal MZ, Roth S. Flexible, transparent electrodes using carbon nanotubes. Nanoscale Res Lett. 2012;7:1-4.
[16] Teweldebrhan D, Balandin AA. Modification of graphene properties due to electron-beam irradiation. Appl Phys Lett. 2009;94(1).
[17] Schedin F, Geim AK, Morozov SV, Hill EW, Blake P, Katsnelson MI, et al. Detection of individual gas molecules adsorbed on graphene. Nat Mater. 2007;6(9):652-5.
[18] Guo BD, Liu QA, Chen ED, Zhu HW, Fang LA, Gong JR. Controllable N-Doping of Graphene. Nano Lett. 2010;10(12):4975-80.
[19] Iqbal MW, Singh AK, Iqbal MZ, Eom J. Raman fingerprint of doping due to metal adsorbates on graphene. J Phys-Condens Mat. 2012;24(33).
[20] Dong XC, Fu DL, Fang WJ, Shi YM, Chen P, Li LJ. Doping Single-Layer Graphene with Aromatic Molecules. Small. 2009;5(12):1422-6.
[21] Bissett MA, Tsuji M, Ago H. Mechanical Strain of Chemically Functionalized Chemical Vapor Deposition Grown Graphene. J Phys Chem C. 2013;117(6):3152-9.
[22] Chan CK, Beechem TE, Ohta T, Brumbach MT, Wheeler DR, Stevenson KJ. Electrochemically Driven Covalent Functionalization of Graphene from Fluorinated Aryl Iodonium Salts. J Phys Chem C. 2013;117(23):12038-44.
[23] Jin Z, McNicholas TP, Shih CJ, Wang QH, Paulus GLC, Hilmer A, et al. Click Chemistry on Solution-Dispersed Graphene and Monolayer CVD Graphene. Chem Mater. 2011;23(14):3362-70.

[24] Sojoudi H, Baltazar J, Tolbert LM, Henderson CL, Graham S. Creating Graphene p-n Junctions Using Self-Assembled Monolayers. ACS Applied Materials & Interfaces. 2012;4(9):4781-6.
[25] Iqbal MZ, Singh AK, Iqbal MW, Seo S, Eom J. Effect of e-beam irradiation on graphene layer grown by chemical vapor deposition. J Appl Phys. 2012;111(8).
[26] Iqbal MZ, Kelekci O, Iqbal MW, Eom J. The structural and electrical evolution of chemical vapor deposition grown graphene by electron beam irradiation induced disorder. Carbon. 2013;59:366-71.
[27] Lucchese MM, Stavale F, Ferreira EHM, Vilani C, Moutinho MVO, Capaz RB, et al. Quantifying ion-induced defects and Raman relaxation length in graphene. Carbon. 2010;48(5):1592-7.
[28] Ferreira EHM, Moutinho MVO, Stavale F, Lucchese MM, Capaz RB, Achete CA, et al. Evolution of the Raman spectra from single-, few-, and many-layer graphene with increasing disorder. Phys Rev B. 2010;82(12).
[29] Mathew S, Chan TK, Zhan D, Gopinadhan K, Barman AR, Breese MBH, et al. The effect of layer number and substrate on the stability of graphene under MeV proton beam irradiation. Carbon. 2011;49(5):1720-6.
[30] Murakami K, Kadowaki T, Fujita J. Damage and strain in single-layer graphene induced by very-low-energy electron-beam irradiation. Appl Phys Lett. 2013;102(4).
[31] Liu HT, Liu YQ, Zhu DB. Chemical doping of graphene. J Mater Chem. 2011;21(10):3335-45.
[32] Farmer DB, Golizadeh-Mojarad R, Perebeinos V, Lin YM, Tulevski GS, Tsang JC, et al. Chemical Doping and Electron-Hole Conduction Asymmetry in Graphene Devices. Nano Lett. 2009;9(1):388-92.
[33] Childres I, Jauregui LA, Tian JF, Chen YP. Effect of oxygen plasma etching on graphene studied using Raman spectroscopy and electronic transport measurements. New J Phys. 2011;13.
[34] Kim DC, Jeon DY, Chung HJ, Woo Y, Shin JK, Seo S. The structural and electrical evolution of graphene by oxygen plasma-induced disorder. Nanotechnology. 2009;20(37).
[35] Wang B, Pantelides ST. Controllable healing of defects and nitrogen doping of graphene by CO and NO molecules. Phys Rev B. 2011;83(24).
[36] Wehling TO, Novoselov KS, Morozov SV, Vdovin EE, Katsnelson MI, Geim AK, et al. Molecular doping of graphene. Nano Lett. 2008;8(1):173-7.
[37] Chen Y, Gao B, Zhao JX, Cai QH, Fu HG. Si-doped graphene: an ideal sensor for NO- or NO2-detection and metal-free catalyst for N2O-reduction. J Mol Model. 2012;18(5):2043-54.
[38] Kim M, Safron NS, Huang CH, Arnold MS, Gopalan P. Light-Driven Reversible Modulation of Doping in Graphene. Nano Lett. 2012;12(1):182-7.
[39] Huh S, Park J, Kim YS, Kim KS, Hong BH, Nam JM. UV/Ozone-Oxidized Large-Scale Graphene Platform with Large Chemical Enhancement in Surface-Enhanced Raman Scattering. Acs Nano. 2011;5(12):9799-806.
[40] Li B, Zhou L, Wu D, Peng HL, Yan K, Zhou Y, et al. Photochemical Chlorination of Graphene. Acs Nano. 2011;5(7):5957-61.
[41] Zhu WJ, Perebeinos V, Freitag M, Avouris P. Carrier scattering, mobilities, and electrostatic potential in monolayer, bilayer, and trilayer graphene. Phys Rev B. 2009;80(23).
[42] Hsu CL, Lin CT, Huang JH, Chu CW, Wei KH, Li LJ. Layer-by-Layer Graphene/TCNQ Stacked Films as Conducting Anodes for Organic Solar Cells. Acs Nano. 2012;6(6):5031-9.
[43] Hwang J, Choi HK, Moon J, Kim TY, Shin JW, Joo CW, et al. Multilayered graphene anode for blue phosphorescent organic light emitting diodes. Appl Phys Lett. 2012;100(13).

[44] Jo G, Choe M, Cho CY, Kim JH, Park W, Lee S, et al. Large-scale patterned multi-layer graphene films as transparent conducting electrodes for GaN light-emitting diodes. Nanotechnology. 2010;21(17).
[45] Ferrari AC, Robertson J. Interpretation of Raman spectra of disordered and amorphous carbon. Phys Rev B. 2000;61(20):14095-107.
[46] Ferrari AC, Meyer JC, Scardaci V, Casiraghi C, Lazzeri M, Mauri F, et al. Raman spectrum of graphene and graphene layers. Phys Rev Lett. 2006;97(18).
[47] Tongay S, Berke K, Lemaitre M, Nasrollahi Z, Tanner DB, Hebard AF, et al. Stable hole doping of graphene for low electrical resistance and high optical transparency. Nanotechnology. 2011;22(42).
[48] Kim KK, Reina A, Shi YM, Park H, Li LJ, Lee YH, et al. Enhancing the conductivity of transparent graphene films via doping. Nanotechnology. 2010;21(28).
[49] Iqbal MZ, Siddique S, Iqbal MW, Eom J. Formation of p-n junction with stable p-doping in graphene field effect transistors using deep UV irradiation. J Mater Chem C. 2013;1(18):3078-83.
[50] Das A, Pisana S, Chakraborty B, Piscanec S, Saha SK, Waghmare UV, et al. Monitoring dopants by Raman scattering in an electrochemically top-gated graphene transistor. Nat Nanotechnol. 2008;3(4):210-5.
[51] Tan YW, Zhang Y, Bolotin K, Zhao Y, Adam S, Hwang EH, et al. Measurement of scattering rate and minimum conductivity in graphene. Phys Rev Lett. 2007;99(24).
[52] Xu ZP, Xue K. Engineering graphene by oxidation: a first-principles study. Nanotechnology. 2010;21(4).
[53] Ryu S, Liu L, Berciaud S, Yu YJ, Liu HT, Kim P, et al. Atmospheric Oxygen Binding and Hole Doping in Deformed Graphene on a SiO2 Substrate. Nano Lett. 2010;10(12):4944-51.
[54] Li ZY, Zhang WH, Luo Y, Yang JL, Hou JG. How Graphene Is Cut upon Oxidation? J Am Chem Soc. 2009;131(18):6320-+.
[55] Cheng YC, Kaloni TP, Zhu ZY, Schwingenschlogl U. Oxidation of graphene in ozone under ultraviolet light. Appl Phys Lett. 2012;101(7).
[56] Hass J, de Heer WA, Conrad EH. The growth and morphology of epitaxial multilayer graphene. J Phys-Condens Mat. 2008;20(32).
[57] Kim KS, Zhao Y, Jang H, Lee SY, Kim JM, Kim KS, et al. Large-scale pattern growth of graphene films for stretchable transparent electrodes. Nature. 2009;457(7230):706-10.
[58] Yan J, Zhang YB, Kim P, Pinczuk A. Electric field effect tuning of electron-phonon coupling in graphene. Phys Rev Lett. 2007;98(16).
[59] Singh AK, Iqbal MW, Singh VK, Iqbal MZ, Lee JH, Chun SH, et al. Molecular n-doping of chemical vapor deposition grown graphene. J Mater Chem. 2012;22(30):15168-74.
[60] Kalbac M, Reina-Cecco A, Farhat H, Kong J, Kavan L, Dresselhaus MS. The Influence of Strong Electron and Hole Doping on the Raman Intensity of Chemical Vapor-Deposition Graphene. Acs Nano. 2010;4(10):6055-63.
[61] Lin J, Zhong JB, Kyle JR, Penchev M, Ozkan M, Ozkan CS. Molecular absorption and photodesorption in pristine and functionalized large-area graphene layers. Nanotechnology. 2011;22(35).
[62] Grujicic M, Cao G, Rao AM, Tritt TM, Nayak S. UV-light enhanced oxidation of carbon nanotubes. Appl Surf Sci. 2003;214(1-4):289-303.
[63] Larciprete R, Lacovig P, Gardonio S, Baraldi A, Lizzit S. Atomic Oxygen on Graphite: Chemical Characterization and Thermal Reduction. J Phys Chem C. 2012;116(18):9900-8.
[64] Xu ZW, Chen L, Li JL, Wang R, Qian XM, Song XY, et al. Oxidation and disorder in few-layered graphene induced by the electron-beam irradiation. Appl Phys Lett. 2011;98(18).
[65] Lee G, Lee B, Kim J, Cho K. Ozone Adsorption on Graphene: Ab Initio Study and Experimental Validation. J Phys Chem C. 2009;113(32):14225-9.

[66] Tao HH, Moser J, Alzina F, Wang Q, Sotomayor-Torres CM. The Morphology of Graphene Sheets Treated in an Ozone Generator. J Phys Chem C. 2011;115(37):18257-60.
[67] Luo ZT, Pinto NJ, Davila Y, Johnson ATC. Controlled doping of graphene using ultraviolet irradiation. Appl Phys Lett. 2012;100(25).
[68] Joo P, Kim BJ, Jeon EK, Cho JH, Kim BS. Optical switching of the Dirac point in graphene multilayer field-effect transistors functionalized with spiropyran. Chem Commun. 2012;48(89):10978-80.
[69] Dai JY, Yuan JM. Adsorption of molecular oxygen on doped graphene: Atomic, electronic, and magnetic properties. Phys Rev B. 2010;81(16).
[70] Shin HJ, Choi WM, Choi D, Han GH, Yoon SM, Park HK, et al. Control of Electronic Structure of Graphene by Various Dopants and Their Effects on a Nanogenerator. J Am Chem Soc. 2010;132(44):15603-9.
[71] Liu H, Ryu S, Chen Z, Steigerwald ML, Nuckolls C, Brus LE. Photochemical reactivity of graphene. Journal of the American Chemical Society. 2009;131(47):17099-101.
[72] Leenaerts O, Partoens B, Peeters FM. Adsorption of H(2)O, NH(3), CO, NO(2), and NO on graphene: A first-principles study. Phys Rev B. 2008;77(12).
[73] Avouris P. Graphene: Electronic and Photonic Properties and Devices. Nano Lett. 2010;10(11):4285-94.
[74] Zhang LM, Diao SO, Nie YF, Yan K, Liu N, Dai BY, et al. Photocatalytic Patterning and Modification of Graphene. J Am Chem Soc. 2011;133(8):2706-13.
[75] Calizo I, Bejenari I, Rahman M, Liu G, Balandin AA. Ultraviolet Raman microscopy of single and multilayer graphene. J Appl Phys. 2009;106(4).
[76] Mulyana Y, Horita M, Ishikawa Y, Uraoka Y, Koh S. Thermal reversibility in electrical characteristics of ultraviolet/ozone-treated graphene. Appl Phys Lett. 2013;103(6).
[77] Matis BR, Burgess JS, Bulat FA, Friedman AL, Houston BH, Baldwin JW. Surface Doping and Band Gap Tunability in Hydrogenated Graphene. Acs Nano. 2012;6(1):17-22.
[78] Yang YX, Brenner K, Murali R. The influence of atmosphere on electrical transport in graphene. Carbon. 2012;50(5):1727-33.
[79] Yuan JT, Ma LP, Pei SF, Du JH, Su Y, Ren WC, et al. Tuning the Electrical and Optical Properties of Graphene by Ozone Treatment for Patterning Monolithic Transparent Electrodes (vol 7, pg 4233, 2013). Acs Nano. 2013;7(6):5647-.
[80] Yuan JT, Ma LP, Pei SF, Du JH, Su Y, Ren WC, et al. Tuning the Electrical and Optical Properties of Graphene by Ozone Treatment for Patterning Monolithic Transparent Electrodes. Acs Nano. 2013;7(5):4233-41.
[81] Wu YQ, Lin YM, Bol AA, Jenkins KA, Xia FN, Farmer DB, et al. High-frequency, scaled graphene transistors on diamond-like carbon. Nature. 2011;472(7341):74-8.
[82] Yang H, Heo J, Park S, Song HJ, Seo DH, Byun KE, et al. Graphene Barristor, a Triode Device with a Gate-Controlled Schottky Barrier. Science. 2012;336(6085):1140-3.
[83] Xia FN, Farmer DB, Lin YM, Avouris P. Graphene Field-Effect Transistors with High On/Off Current Ratio and Large Transport Band Gap at Room Temperature. Nano Lett. 2010;10(2):715-8.
[84] Jafri SHM, Carva K, Widenkvist E, Blom T, Sanyal B, Fransson J, et al. Conductivity engineering of graphene by defect formation. J Phys D Appl Phys. 2010;43(4).
[85] Banhart F, Kotakoski J, Krasheninnikov AV. Structural Defects in Graphene. Acs Nano. 2011;5(1):26-41.
[86] Huard B, Sulpizio JA, Stander N, Todd K, Yang B, Goldhaber-Gordon D. Transport measurements across a tunable potential barrier in graphene. Phys Rev Lett. 2007;98(23).

[87] Teweldebrhan D, Balandin AA. Response to "Comment on 'Modification of graphene properties due to electron-beam irradiation' " [Appl. Phys. Lett. 95, 246101(2009)]. Appl Phys Lett. 2009;95(24).
[88] Childres I, Jauregui LA, Foxe M, Tian JF, Jalilian R, Jovanovic I, et al. Effect of electron-beam irradiation on graphene field effect devices. Appl Phys Lett. 2010;97(17).
[89] Kim KJ, Choi JH, Lee H, Lee HK, Kang TH, Han YH, et al. Effects of 1 MeV electron beam irradiation on multilayer graphene grown on 6H-SiC(0001). J Phys Chem C. 2008;112(34):13062-4.
[90] Compagnini G, Giannazzo F, Sonde S, Raineri V, Rimini E. Ion irradiation and defect formation in single layer graphene. Carbon. 2009;47(14):3201-7.
[91] Krasheninnikov AV, Nordlund K. Ion and electron irradiation-induced effects in nanostructured materials. J Appl Phys. 2010;107(7).
[92] Balandin AA. Thermal properties of graphene and nanostructured carbon materials. Nat Mater. 2011;10(8):569-81.
[93] Nika DL, Ghosh S, Pokatilov EP, Balandin AA. Lattice thermal conductivity of graphene flakes: Comparison with bulk graphite. Appl Phys Lett. 2009;94(20).
[94] Calizo I, Balandin AA, Bao W, Miao F, Lau CN. Temperature dependence of the Raman spectra of graphene and graphene multilayers. Nano Lett. 2007;7(9):2645-9.
[95] Liu G, Teweldebrhan D, Balandin AA. Tuning of Graphene Properties via Controlled Exposure to Electron Beams.
[96] Chen JH, Cullen WG, Jang C, Fuhrer MS, Williams ED. Defect Scattering in Graphene. Phys Rev Lett. 2009;102(23).
[97] Suk JW, Kitt A, Magnuson CW, Hao YF, Ahmed S, An JH, et al. Transfer of CVD-Grown Monolayer Graphene onto Arbitrary Substrates. Acs Nano. 2011;5(9):6916-24.
[98] Cancado LG, Jorio A, Ferreira EHM, Stavale F, Achete CA, Capaz RB, et al. Quantifying Defects in Graphene via Raman Spectroscopy at Different Excitation Energies. Nano Lett. 2011;11(8):3190-6.
[99] Tuinstra F, Koenig JL. Raman Spectrum of Graphite. J Chem Phys. 1970;53(3):1126-&.
[100] Lazzeri M, Attaccalite C, Wirtz L, Mauri F. Impact of the electron-electron correlation on phonon dispersion: Failure of LDA and GGA DFT functionals in graphene and graphite. Phys Rev B. 2008;78(8).
[101] Tanuma S, Powell CJ, Penn DR. Calculations of stopping powers of 100 eV-30 keV electrons in 31 elemental solids. J Appl Phys. 2008;103(6).
[102] Morozov SV, Novoselov KS, Schedin F, Jiang D, Firsov AA, Geim AK. Two-dimensional electron and hole gases at the surface of graphite. Phys Rev B. 2005;72(20).
[103] Shinn E, Hübler A, Lyon D, Perdekamp MG, Bezryadin A, Belkin A. Nuclear energy conversion with stacks of graphene nanocapacitors.
[104] Tan YW, Zhang Y, Bolotin K, Zhao Y, Adam S, Hwang EH, et al. Measurement of scattering rate and minimum conductivity in graphene. Physical review letters. 2007;99(24):246803.
[105] Artukovic E, Kaempgen M, Hecht DS, Roth S, GrUner G. Transparent and flexible carbon nanotube transistors. Nano Lett. 2005;5(4):757-60.
[106] Takenobu T, Takahashi T, Kanbara T, Tsukagoshi K, Aoyagi Y, Iwasa Y. High-performance transparent flexible transistors using carbon nanotube films. Appl Phys Lett. 2006;88(3).
[107] Cao Q, Zhu ZT, Lemaitre MG, Xia MG, Shim M, Rogers JA. Transparent flexible organic thin-film transistors that use printed single-walled carbon nanotube electrodes. Appl Phys Lett. 2006;88(11).

[108] Zhang JL, Wang C, Zhou CW. Rigid/Flexible Transparent Electronics Based on Separated Carbon Nanotube Thin-Film Transistors and Their Application in Display Electronics. Acs Nano. 2012;6(8):7412-9.
[109] Jang S, Jang H, Lee Y, Suh D, Baik S, Hong BH, et al. Flexible, transparent single-walled carbon nanotube transistors with graphene electrodes. Nanotechnology. 2010;21(42).
[110] Lee D, Cui TH. Low-cost, transparent, and flexible single-walled carbon nanotube nanocomposite based ion-sensitive field-effect transistors for pH/glucose sensing. Biosens Bioelectron. 2010;25(10):2259-64.
[111] Gruner G. Carbon nanotube films for transparent and plastic electronics. J Mater Chem. 2006;16(35):3533-9.
[112] Ferrer-Anglada N, Puigdemont JP, Roth S. Impedance and quantitative TGA characterization of transparent carbon nanotube thin films. Phys Status Solidi B. 2008;245(10):2276-9.
[113] Hu L, Hecht DS, Gruner G. Percolation in transparent and conducting carbon nanotube networks. Nano Lett. 2004;4(12):2513-7.
[114] Bekyarova E, Itkis ME, Cabrera N, Zhao B, Yu AP, Gao JB, et al. Electronic properties of single-walled carbon nanotube networks. J Am Chem Soc. 2005;127(16):5990-5.
[115] Vigolo B, Coulon C, Maugey M, Zakri C, Poulin P. An experimental approach to the percolation of sticky nanotubes. Science. 2005;309(5736):920-3.
[116] Iqbal MZ, Iqbal MW, Eom J, Ahmad M, Ferrer-Anglada N. Capacitive tunnels in single-walled carbon nanotube networks on flexible substrate. J Appl Phys. 2012;111(6).
[117] Jung M, Kim J, Noh J, Lim N, Lim C, Lee G, et al. All-Printed and Roll-to-Roll-Printable 13.56-MHz-Operated 1-bit RF Tag on Plastic Foils. Ieee T Electron Dev. 2010;57(3):571-80.
[118] Burke PJ. An RF circuit model for carbon nanotubes. Ieee T Nanotechnol. 2003;2(1):55-8.
[119] Green AA, Hersam MC. Colored semitransparent conductive coatings consisting of monodisperse metallic single-walled carbon nanotubes. Nano Lett. 2008;8(5):1417-22.
[120] Kumar S, Cola BA, Jackson R, Graham S. A Review of Carbon Nanotube Ensembles as Flexible Electronics and Advanced Packaging Materials. J Electron Packaging. 2011;133(2).
[121] Fuhrer MS, Nygard J, Shih L, Forero M, Yoon YG, Mazzoni MSC, et al. Crossed nanotube junctions. Science. 2000;288(5465):494-7.
[122] Kaiser AB, Dusberg G, Roth S. Heterogeneous model for conduction in carbon nanotubes. Phys Rev B. 1998;57(3):1418-21.
[123] Stadermann M, Papadakis SJ, Falvo MR, Novak J, Snow E, Fu Q, et al. Nanoscale study of conduction through carbon nanotube networks. Phys Rev B. 2004;69(20).
[124] Chimot N, Derycke V, Goffman MF, Bourgoin JP, Happy H, Dambrine G. Gigahertz frequency flexible carbon nanotube transistors. Appl Phys Lett. 2007;91(15).
[125] Fischer JE, Dai H, Thess A, Lee R, Hanjani NM, Dehaas DL, et al. Metallic resistivity in crystalline ropes of single-wall carbon nanotubes. Phys Rev B. 1997;55(8):R4921-R4.
[126] Petit P, Jouguelet E, Fischer JE, Rinzler AG, Smalley RE. Electron spin resonance and microwave resistivity of single-wall carbon nanotubes. Phys Rev B. 1997;56(15):9275-8.
[127] Duan XF, Niu CM, Sahi V, Chen J, Parce JW, Empedocles S, et al. High-performance thin-film transistors using semiconductor nanowires and nanoribbons. Nature. 2003;425(6955):274-8.
[128] Liu X, Long YZ, Liao L, Duan XF, Fan ZY. Large-Scale Integration of Semiconductor Nanowires for High-Performance Flexible Electronics. Acs Nano. 2012;6(3):1888-900.
[129] Yuan HC, Ma ZQ. Microwave thin-film transistors using Si nanomembranes on flexible polymer substrate. Appl Phys Lett. 2006;89(21).
[130] Cao Q, Hur SH, Zhu ZT, Sun YG, Wang CJ, Meitl MA, et al. Highly bendable, transparent thin-film transistors that use carbon-nanotube-based conductors and semiconductors with elastomeric dielectrics. Adv Mater. 2006;18(3):304-+.

[131] Kang SJ, Kocabas C, Ozel T, Shim M, Pimparkar N, Alam MA, et al. High-performance electronics using dense, perfectly aligned arrays of single-walled carbon nanotubes. Nat Nanotechnol. 2007;2(4):230-6.
[132] Sun YG, Menard E, Rogers JA, Kim HS, Kim S, Chen G, et al. Gigahertz operation in flexible transistors on plastic substrates. Appl Phys Lett. 2006;88(18).
[133] Bradley K, Gabriel JCP, Gruner G. Flexible nanotube electronics. Nano Lett. 2003;3(10):1353-5.
[134] Xu H, Anlage SM, Hu LB, Gruner G. Microwave shielding of transparent and conducting single-walled carbon nanotube films. Appl Phys Lett. 2007;90(18).
[135] Xu H, Zhang SX, Anlage SM, Hu LB, Gruner G. Frequency- and electric-field-dependent conductivity of single-walled carbon nanotube networks of varying density. Phys Rev B. 2008;77(7).
[136] Li SD, Yu Z, Yen SF, Tang WC, Burke PJ. Carbon nanotube transistor operation at 2.6 GHz. Nano Lett. 2004;4(4):753-6.
[137] Burke PJ. An RF circuit model for carbon nanotubes (vol 2, pg 55, 2003). Ieee T Nanotechnol. 2004;3(2):331-.
[138] Searle A, Kirkup L. Real time impedance plots with arbitrary frequency components. Physiol Meas. 1999;20(1):103-14.
[139] Schwartz A, Scheffler M, Anlage SM. Determination of the magnetization scaling exponent for single-crystal La0.8Sr0.2MnO3 by broadband microwave surface impedance measurements. Phys Rev B. 2000;61(2):R870-R3.
[140] Thomsen C, Reich S, Maultzsch J. Resonant Raman spectroscopy of nanotubes. Philos T Roy Soc A. 2004;362(1824):2337-59.
[141] Dresselhaus MS, Jorio A, Hofmann M, Dresselhaus G, Saito R. Perspectives on Carbon Nanotubes and Graphene Raman Spectroscopy. Nano Lett. 2010;10(3):751-8.
[142] Fukuhara M, Seto M, Inoue A. ac impedance analysis of a Ni-Nb-Zr-H glassy alloy with femtofarad capacitance tunnels. Appl Phys Lett. 2010;96(4).
[143] Vavro J, Kikkawa JM, Fischer JE. Metal-insulator transition in doped single-wall carbon nanotubes. Phys Rev B. 2005;71(15).
[144] Yu Z, Burke PJ. Microwave transport in metallic single-walled carbon nanotubes. Nano Lett. 2005;5(7):1403-6.
[145] Wang D, Yu Z, McKernan S, Burke PJ. Ultrahigh frequency carbon nanotube transistor based on a single nanotube. Ieee T Nanotechnol. 2007;6(4):400-3.
[146] Dyre JC, Schroder TB. Universality of ac conduction in disordered solids. Rev Mod Phys. 2000;72(3):873-92.

Curriculum Vitae

Muhammad Zahir Iqbal

Education:-

Degree: Doctorate in Computational and Applied Physics (PhD)

University: Universitat Politècnica de Catalunya (UPC), Barcelona, Spain

Duration: 03/2010 –

Title: Structural and electrical characterization of doped graphene and carbon nanotube networks.

Degree: **Master of Philosophy in Physics (M. Phil)**

University: Government College University, Lahore, Pakistan

Duration: 09/2005 -08/2008

Thesis title: Synthesis and characterization of colossal magnetoresistance nanoparticles.

Degree: **Masters in Physics (M. Sc)**

University: University of the Punjab, Lahore, Pakistan
Duration: 09/2002 -08/2004
Thesis title: Monitoring and Controlling of Temperature with PC Parallel Port (Electronics).

Professional Experience:-

Duration: 09/2007 – 03/2010

Designation: Full time Lecturer in Physics

University: Government College University, Lahore, Pakistan

Research Skills & Activities

- Expertise in the two dimensional hydride structure device engineering and characterization (including graphene, boron nitride, MoS_2, WS_2).
- Spintronic device engineering and characterization.
- Study of mesoscopic phenomena and quantum Hall systems in two dimensional hybrid structures.
- Expertise in nano/micro device fabrication using photo- and electron beam lithography.

- CNTs network for flexible and transparent electronic devices.
- Low temperature cryogenic (He^3 cryostat) electronic transport measurements.
- Raman spectroscopy (ReniShaw) measurements.
- High magnetic field (9T) transport measurements.
- Experience of metal and chemical doping treatment of two dimensional materials.

On-going Projects:-

- Graphene-MoS_2 vertical layered heterostructures for photocurrent generation.
- Gate tunable controlled transport through Graphene-WS_2 vertical hybrid structures.

Journal Publications:-

Published Articles:-

1. **M. Z. Iqbal**, M. F. Khan, M. W. Iqbal, Jonghwa Eom, *Tuning the electrical properties of exfoliated graphene layers by deep ultraviolet irradiation,* Journal of Materials Chemistry C, 2014. *(Accepted).*

2. M. W. Iqbal, **M. Z. Iqbal**, Xiaozhan Jin, Chanyong Hwang, Jonghwa Eom, *Edge oxidation effect of chemical vapor deposition grown graphene nanoconstriction,* ACS Applied Materials & Interfaces,4207-4213, 6(6), 2014.

3. **M. Z. Iqbal**, M. W. Iqbal, Jae Hong Lee, Yong Seung Kim, Seunghyun Chun, Jonghwa Eom, *Spin valve effect of NiFe/graphene/NiFe junctions*, Nano Research, 373-380, 6(5), 2013.

4. **M. Z. Iqbal**, O. Kelekci, M.W. Iqbal, Jonghwa Eom, *The structural and electrical evolution of chemical vapor deposition grown graphene by electron beam irradiation induced disorder,* Carbon, 361-377, 59, 2013.

5. **M. Z. Iqbal**, S. Siddique, M. W. Iqbal, Jonghwa Eom, *Formation of p–n junction with stable p-doping in graphene field effect transistors using deep UV irradiation*, Journal of Materials Chemistry C, 3078-3083, 1, 2013.

6. Núria Ferrer-Anglada, Jordi Pérez-Puigdemont, Jordi Figueras, **M. Z. Iqbal,** Siegmar Roth, *Flexible, transparent electrodes using carbon nanotubes*, Nanoscale Research Letters, 571, 7, 2012.

7. G. R. Turpu, M. W. Iqbal, **M. Z. Iqbal**, Jonghwa Eom, *Relaxation in bi-stable resistive states of chemical vapor deposition grown graphene*, Thin Solid Films, 468-472, 522, 2012.

8. M. W. Iqbal, A. K. Singh, **M. Z. Iqbal**, Jonghwa Eom, *Raman fingerprint of doping due to metal adsorbates on graphene*, Journal of Physics Condensed Matter, 335301, 24, 2012.

9. A. K. Singh, M. W. Iqbal, V. K. Singh, **M. Z. Iqbal**, Jae Hong Lee, Seung-Hyun Chun, Koo Shin, Jonghwa Eom, *Molecular n-doping of chemical vapor deposition grown graphene,* Journal of Materials Chemistry, 15168, 22, 2012.

10. **M. Z. Iqbal**, A. K. Singh, M. W. Iqbal, Sunae Seo, Jonghwa Eom, *Effect of e-beam irradiation on graphene layer grown by chemical vapor deposition*. Journal of Applied Physics, 111, 084307, 2012.

11. **M. Z. Iqbal**, M. W. Iqbal, Jonghwa Eom, Muneer Ahmad, Núria Ferrer-Anglada, *Capacitive tunnels in single-walled carbon nanotube networks on flexible substrate*. Journal of Applied Physics, 063712, 111, 2012.

Submitted/In preparation manuscripts:-

1. **M. Z. Iqbal**, M. W. Iqbal, Xiaozhan Jin, Chanyong Hwang, Jonghwa Eom, *Polarity of magnetoresistance in graphene interlayer spin valves, submitted.*

2. **M. Z. Iqbal**, Dongchul Sung, M. W. Iqbal, M. F. Khan, Jonghwa Eom, Suklyun Hong, *Ultraviolet light induced doping in graphene and the origin of reversible modulation, submitted.*

3. **M. Z. Iqbal**, Özgür Kelekçi, M. W. Iqbal, Xiaozhan Jin, Chanyong Hwang, Jonghwa Eom, *Enhanced intervalley scattering in artificially stacked double layer graphene, submitted.*

4. M. W. Iqbal, **M. Z. Iqbal**, Xiaozhan Jin, Chanyong Hwang, Jonghwa Eom, *Superior characteristics of graphene enclosed by chemical-vapor-deposition-grown hexagonal boron nitride, submitted.*

5. **M. Z. Iqbal**, Jordi Pérez-Puigdemont, Jonghwa Eom, Núria Ferrer-Anglada, *High frequency impedance of single-walled carbon nanotube networks on flexible substrate, submitted.*

6. M. F. Khan, **M. Z. Iqbal**, M. W. Iqbal, Jonghwa Eom, *Improving graphene properties of graphene layer by chemical doping, submitted.*

7. M. W. Iqbal, **M. Z. Iqbal**, M. F. Khan, Jonghwa Eom, *Modification of structural and electrical properties graphene layers by Pt adsorbates, submitted.*

8. Jinwoo Choi, Hyeji Kim, Jaehyun Park, M. W. Iqbal, **M. Z. Iqbal,** Jonghwa Eom, Wan-Gyu Lee, and Jongwan Jung, *Enhanced performance of graphene by using gold film for transfer and masking process, submitted.*

9. **M. Z. Iqbal**, M. W. Iqbal, Xiaozhan Jin, Chanyong Hwang, Jonghwa Eom, *Coexistence of massive and massless Dirac fermions in artificially stacked graphene bilayer, In preparation.*

10. **M. Z. Iqbal**, S. Hussain, Jangwan Jung, Jonghwa Eom, *Chemical vapor deposition grown molybdenum disulfide field effect transistor for high-performance photoresponce, In preparation.*

11. **M. Z. Iqbal**, M. F. Khan, M. W. Iqbal, Jonghwa Eom, *Gate tunable controlled tunneling through graphene-boron nitride hybrid structures, In preparation.*

Conference Presentations/Attended:-

1. Poster presentation, *Observation of fractal quantum Hall effect in artificially stacked CVD grown graphene bilayer,* The 8th International conference on Advanced Materials and Devices, December 11-13, 2013, Ramada Plaza Jeju Hotel, Jeju, South Korea.
2. Poster presentation, *Quantum Hall effect in artificially stacked graphene bilayer,* 5th recent progress in graphene research, September 9-13, 2013, Tokyo, Japan.
3. Oral presentation, *Quantum Hall effect in non-Bernal stacked bilayer graphene,* Graphene workshop, KRISS, July 5-6, 2013, Jeju, South Korea

4. Poster presentation, *Reversible p-doping of graphene activated by deep ultraviolet light,* Korean Physics Society (KPS) meeting at Daejeon convention centre, April 24-26, 2013, Daejeon, South Korea.
5. Oral presentation, *Current perpendicular to plane transport in single and bilayer graphene,* Korean Physics Society (KPS) meeting, October, 24-26, 2012, Pyung Chang, South Korea.
6. Attended Graphene workshop, Korean Research Institute of Standards and Science (KRISS) meeting, July, 2012, Anmyeondo, South Korea.
7. Poster presentation, *Spin valve effect in NiFe/Graphene/NiFe junctions,* International conference of magnetism (ICM), July 8-13, 2012, Busan, South Korea.
8. Poster presentation, *Spin filtering with single and bilayer graphene interlayers in magnetic junctions,* Annual poster competition at Dept. of Physics Sejong University, October, 2012.
9. Poster presentation, *Vertical spin transport in single layer graphene,* The 7th International conference on Advanced Materials and Devices (ICMAD), December 7-9, 2011, Ramada Plaza Jeju Hotel, Jeju Korea.
10. Poster presentation, *Spin valve effect in graphene interlayer junctions,* Annual poster competition at Dept. of Physics Sejong University, October, 2011.
11. Invited talk, *Ambipolar bi-stable switching effects in CVD graphene devices,* The 9th International Nanotech Symposium & Exhibition Nano-Korea, KNTEX, August 24-26, 2011, Seoul, South Korea.
12. Attended Graphene workshop, Korean Research Institute of Standards and Science (KRISS) meeting, July, 2011, Anmyeondo, South Korea.
13. Invited talk, *Transparent and flexible carbon nanotubes thin film networks,* The 18th International Conference on Composite Materials (ICCM 18), August 21-26 2011, Jeju convention centre, Jeju, South Korea.
14. Poster presentation, *Transparent and flexible carbon nanotubes thin film network: Impedance dependence on sample geometry and nanotube density,* Meeting of the International Research Group on Graphene and Nanotubes (GNT GRD-I), February 7-11, 2011, Dourdan, France.